J. Fluid Mech. (1970), *vol.* 41, *part* 1, *pp.* 81–139
Boeing Symposium on Turbulence

Experiments on nearly homogeneous turbulent shear flow

By F. H. CHAMPAGNE,† V. G. HARRIS AND S. CORRSIN

Department of Mechanics, The Johns Hopkins University,
Baltimore, Maryland 21218, U.S.A.

(Received 2 September 1969)

With a transverse array of channels of equal widths but differing resistances, we have generated an improved approximation to spatially homogeneous turbulent shear flow. The scales continue to grow with downstream distance, even in a region where the mean velocity gradient and one-point turbulence moments (component energies and shear stress) have attained essentially constant values. This implies asymptotic non-stationarity in the basic Eulerian frame convected with the mean flow, behaviour which seems to be inherent to homogeneous turbulent shear flow.

Two-point velocity correlations with space separation and with space-time separation yield characteristic departures from isotropy, including clear 'upstream–downstream' unsymmetries which cannot be classified simply as axis tilting of ellipse-like iso-correlation contours.

The high wave-number structure is roughly locally isotropic although the turbulence Reynolds number based on Taylor 'microscale' and r.m.s. turbulent velocity is only 130. Departures from isotropy in the turbulent velocity gradient moments are measurable.

The approximation to homogeneity permits direct estimation of all components of the turbulent pressure/velocity-gradient tensor, which accounts for intercomponent energy transfer and helps to regulate the turbulent shear stress. It is found that its principal axes are aligned with those of the Reynolds stress tensor. Finally, the Rotta (1951, 1962) linear hypothesis for intercomponent energy transfer rate is roughly confirmed.

CONTENTS

---

† Present address: Boeing Scientific Research Laboratories.

Printed in Great Britain

4. Measurements

5. Analysis of experimental results

1. Introduction

The central role of shear in most natural and technological turbulent flows arises in coupling the mean velocity field with the turbulent velocity field. The spatial variation of the turbulent shear stress determines the mean velocity distribution, as seen in the mean momentum equations, and the turbulent motion itself is maintained and moulded by the interaction of the mean velocity non-uniformities with the Reynolds stresses, vorticity fluctuations, etc.

These interactions can be identified as various terms in the averaged equations for momentum, mean flow kinetic energy, turbulence kinetic energy, turbulent shear stress (Reynolds 1895, Chou 1945 etc.). This identification might be described as the outcome of the 'Reynolds theory' of turbulence, i.e. the notion that random hydrodynamic motion can be decomposed into mean and fluctuating parts.

The early attempts to make the turbulent shear flow problem analytically determinate with a minimum input of empirical information centred upon the mean momentum equation. Various physically motivated relations were tried as expressions of local turbulent shear stress in terms of local mean velocity gradient and higher derivatives. From the early *ad hoc* turbulent ('eddy') viscosity ideas of de Saint-Venant (1843) and Boussinesq (1877), through the mixing-length theories of Taylor (1915, for heat transfer), Prandtl (1925, 1942), von Kármán (1930, 1937), Nevzgljadov (1945) and others [see Hinze (1959) for a partial account], the phenomenological theories have become increasingly sophisticated.

Among the many theories since 1945, the strain-rate approach of Townsend (1956) and the 'wave-like' approaches of Landahl (1967) and Phillips (1967), for example, show notable physical motivation.

Central shortcomings of the earlier eddy viscosity and mixing-length theories are that they assume (*a*) simple gradient transport (a local concept) with (*b*) an eddy viscosity which is locally controlled. Batchelor (1950) and Corrsin (1957) pointed out that any theoretical model which uses a simple gradient transport concept for turbulent transport must be wrong in principle because it implies a transporting mechanism which is much smaller than the distance over which the mean values change appreciably. This criticism applies to both eddy viscosity theories and the oldest types of mixing-length theories. Surprisingly, these kinds of theories, judiciously applied, can be made to give fairly good predictions of mean velocity, especially in 'free' shear flows, but even in wall flows.

Some recent analytical work has started to generalize the earlier theories by introducing a non-local eddy viscosity (see, for example, Nee & Kovasznay 1969) and/or a transport rate expression with memory (Lumley 1967). The traditional turbulent shear flows (boundary layer, tube, jet, wake) have their turbulent shear stress carried by eddies which are large enough to cover distances over which the mean velocity gradient changes appreciably. In fact, these shear-carrying eddies are comparable in size to the lateral distance between flow boundaries, so they may be affected by the boundary conditions (Corrsin 1957). This suggested the scientific importance of devising a shear flow in which the relation between shear stress and mean velocity gradient (strain rate) field could be studied without the complicating effects of boundary conditions. The rational method of starting with the simplest case suggests a flow without mean profile curvature. This leads to the simplest conceivable shear flow, homogeneous turbulence maintained by a uniform mean shear.

Although homogeneity requires an infinite spatial field, it can be approximated in practice if the integral scales of the turbulence field are much smaller than the distances over which the mean strain-rate is essentially constant. In proposing the experiment, Corrsin (1963, p. 524) discussed some of the difficulties, including the possibility that such a homogeneous turbulent shear flow might not remain in equilibrium. Since the momentum-carrying eddies in the traditional shear flows are not small relative to the gross shear zone width, a grid-generated homogeneous shear flow might simply develop larger and larger eddies. Such a mean velocity field contains no inherent characteristic length, such as the ratio of first to second derivative. In fact, when Rose (1966) attempted to generate a homogeneous turbulent shear flow (using a plane parallel-rod grid of uniform rod diameter and non-uniform spacing) he found the turbulence scales growing monotonically downstream. His flow field attained other properties of a homogeneous shear flow: a uniform mean velocity gradient, uniform turbulence intensities, and a (roughly) uniform turbulent shear stress. However, there also remained downstream a spatial variation of the scales in planes perpendicular to the mean flow, a vestige of the non-uniformity of the shear-generating grid.

The problem of exactly homogeneous turbulent shear flow has been examined analytically by several investigators. Reis (1952), Burgers & Mitchner (1953) and Craya (1958) deduced the symmetry properties of the various velocity correlations and derived equations governing the two-point, single time correlation and the corresponding spectral equations.

Townsend's (1956) strain-rate theory of Reynolds stress is based largely on the idea that a parcel of turbulent fluid whose scale is small compared with the shear zone width is subjected to a local uniform mean strain rate. He conjectured that (*a*) a state of structural equilibrium of the turbulence would be attained under the action of an irrotational, constant mean strain rate, and that (*b*) this state is approximately the same as that produced by a uniform plane (rotational) shearing motion with equal strain rate. Moffat (1967, p. 139) suggested that this neglect of the rigid body rotation may be unjustifiable if the process of vortex line stretching is less efficient when the rigid body rotation is present. Pearson (1959) performed a 'weak turbulence' (effectively, small Reynolds number) analysis in which the self-interaction of the turbulent field was neglected. He computed the linearized response (i.e. with triple correlation discard) of an initially isotropic turbulence subjected to a sudden uniform gross shear. Deissler (1961) and Fox (1964) pursued the same problem in greater detail. The results show that in this truncated model, whose self-consistency remains to be investigated, the turbulence energy eventually decreases to zero. The turbulence is not sustained. Nevertheless, it shows qualitative features strikingly like those observed in real shear flows. Hasen (1967) has computed the behaviour of a two-dimensional disturbance in the linear approximation and in a non-linear one.

The purpose of the present experimental study was to generate a closer approximation to homogeneous turbulent shear flow than that obtained by Rose, and then to investigate the structure of the resulting flow field. The turbulent structure was not expected to reach an exact equilibrium or stationary state, but the hope was that the length scales growth rate with increasing distance from the grid would be relatively slow. Then, this 'asymptotic state', where the turbulence intensities and shear stress were maintained at nearly uniform values, would be a region of the flow field which was nearly homogeneous. The resulting negligibility of some terms in the component energy equations then allows indirect estimation of the pressure-velocity correlation terms, which have not yet been measured away from solid boundaries with unequivocal precision. This gives new information on intercomponent energy transfer and on the destruction of turbulent shear stress.

Finally, it should be noted that many turbulent shear stress theories either assume (e.g. von Kármán 1930, Taylor 1932) or conclude (e.g. Phillips 1967) that the mean strain-rate gradient is an essential determinant of the turbulent shear stress. Since we make that quantity negligible in this kind of experiment, those theories are not directly tested. In fact, the experiment is designed primarily to get information, not to test prior theories.

2. Analytical preliminaries

2.1. *Moment equations for homogeneous turbulent shear flow*

As a prelude to the experimental report, it is helpful to inspect the simplest moment equations for the postulated case of homogeneous turbulent shear flow. Theoretical investigators who worked with the full equations (Reis 1952, Burgers & Mitchner 1953, Craya 1958) appear to have assumed that a stationary asymptotic state is possible. It seems to us that this is actually one of the questions to be investigated because (like isotropic turbulence) this system has no intrinsic length or velocity scales. If it had one, it would of course have the other, the connexion being given by the mean velocity gradient.

To begin we assume rectilinear mean flow $\overline{U}_1(x_2, t)$ parallel to the x_1 axis. $\overline{U}_2 = \overline{U}_3 = 0$. $\partial\overline{U}_1/\partial x_2$ is independent of $\mathbf{x}$. With the restriction to homogeneity, all one-point averages except $\overline{U}_1$ can depend at most on time t. The mean momentum equation reduces to

$$\partial\overline{U}_1/\partial t = 0. \tag{2.1}$$

The equation for the mean *velocity gradient* (in this case the same as mean *vorticity* and mean *strain rate*) is, more or less trivially,

$$\frac{\partial}{\partial t}\left(\frac{\partial\overline{U}_1}{\partial x_2}\right) = 0. \tag{2.2}$$

This $\partial/\partial t$ could be written as an ordinary total derivative, but maintaining the partial derivative symbols in this part of the text serves to remind us that these equations are deduced from more complicated ones.

The time rate of change of the *kinetic energy of the mean flow*,

$$E \equiv \tfrac{1}{2}\overline{U}_j\overline{U}_j = \tfrac{1}{2}\overline{U}_1^2,$$

can first be simplified to

$$\frac{\partial E}{\partial t} = \overline{u_1u_2}\frac{\partial\overline{U}_1}{\partial x_2} - \frac{\partial}{\partial x_2}(\overline{U}_1\overline{u_1u_2}) + \nu\frac{\partial^2E}{\partial x_2^2} - \nu\left(\frac{\partial\overline{U}_1}{\partial x_2}\right)^2. \tag{2.3}$$

The first term on the right side is the negative of the familiar turbulent energy production rate term, the second is change rate due to net turbulent convection of E down the E gradient,† the third is change rate due to viscous transport of E down the E gradient, and the last is the rate of viscous dissipation of E directly to internal energy of the fluid. We note that the first two just balance each other and the last two just balance each other, so

$$\partial E/\partial t = 0. \tag{2.4}$$

Physically, the local loss of mean flow kinetic energy to turbulent and internal energies is precisely made up by the non-uniformities of the two kinds of flux rate. The flux rates are non-uniform because the E gradient is not constant. We note in passing that the function $E(x_2)$ changes under a Galilean transformation along x_1.

---

† Although the identification of the general term $-\partial(\overline{U}_k\overline{u_iu_k})/\partial x_i$ as turbulent convective transport of the mean flow kinetic energy is 'obvious' by a process of elimination (it is the only physical phenomenon left after all the others have been correctly written), we can supplement the expository literature by a brief analytical demonstration: Suppose we have a random fluid property $A(\mathbf{x}, t)$ and form a moment equation for its mean field $\overline{A}$. The mean turbulent convection rate of $\overline{A}$ is $\overline{u_kA}$ and the local rate of increase of $\overline{A}$ due to inhomogeneity in this vector flux is $-\partial(\overline{u_kA})/\partial x_k$. Mean flow kinetic energy, $E \equiv \frac{1}{2}\overline{U}_j\overline{U}_j$, is formed by averaging the random fluid property $A \equiv \frac{1}{2}(U_jU_j - u_iu_i)$, where $\mathbf{U} \equiv \overline{\mathbf{U}} + \mathbf{u}$. Therefore the average convective flux vector is

$$\overline{\tfrac{1}{2}u_k[(\overline{U}_j+u_j)(\overline{U}_j+u_j) - u_iu_i]} = \overline{u_ku_j}\,\overline{U}_j.$$

The balance equation for the *mean turbulent kinetic energy* $\bar{e} \equiv \frac{1}{2}\overline{u_k u_k}$ has the simple form

$$\frac{\partial \bar{e}}{\partial t} = -\overline{u_1 u_2}\frac{\partial \bar{U}_1}{\partial x_2} - \nu\overline{\frac{\partial u_i}{\partial x_k}\frac{\partial u_i}{\partial x_k}}. \tag{2.5}$$

The first term on the right (ordinarily found to be $\geqslant 0$) is the rate of production from the mean flow kinetic energy, the second is the viscous dissipation rate. No further simplification can be made.

The three Cartesian component turbulent energy equations have the corresponding forms

$$\left.\begin{aligned} \frac{\partial \bar{e}_{(1)}}{\partial t} &= -\overline{u_1 u_2}\frac{\partial \bar{U}_1}{\partial x_2} + \frac{1}{\rho}\overline{p\frac{\partial u_1}{\partial x_1}} - \nu\overline{\frac{\partial u_1}{\partial x_k}\frac{\partial u_1}{\partial x_k}}, \\ \frac{\partial \bar{e}_{(2)}}{\partial t} &= \frac{1}{\rho}\overline{p\frac{\partial u_2}{\partial x_2}} - \nu\overline{\frac{\partial u_2}{\partial x_k}\frac{\partial u_2}{\partial x_k}}, \\ \frac{\partial \bar{e}_{(3)}}{\partial t} &= \frac{1}{\rho}\overline{p\frac{\partial u_3}{\partial x_3}} - \nu\overline{\frac{\partial u_3}{\partial x_k}\frac{\partial u_3}{\partial x_k}}. \end{aligned}\right\} \tag{2.6}$$

The energy is all fed into $\bar{e}_{(1)} \equiv \frac{1}{2}\overline{u_1^2}$, then parcelled out to the other components via the pressure-velocity covariance terms. Thus we expect that this term will be < 0 for $\bar{e}_{(1)}$ and > 0 for $\bar{e}_{(2)}$ and $\bar{e}_{(3)}$.

The Reynolds shear stress balance (apparently first employed by Chou 1945) reduces to

$$\frac{\partial}{\partial t}(-\overline{u_1 u_2}) = \overline{u_2^2}\frac{\partial \bar{U}_1}{\partial x_2} - \frac{1}{\rho}\overline{p\left(\frac{\partial u_1}{\partial x_2} + \frac{\partial u_2}{\partial x_1}\right)} + 2\nu\overline{\frac{\partial u_1}{\partial x_k}\frac{\partial u_2}{\partial x_k}}. \tag{2.7}$$

The first term on the right is production rate. At first glance we cannot say whether the pressure-velocity covariance helps or hinders the growth of shear stress, and the sign of the viscous term is not obvious *a priori* either. If we note, however, that $\overline{(\partial u_1/\partial x_k)(\partial u_2/\partial x_k)}$ is zero in isotropic turbulence, we are led to speculate that in very high Reynolds number turbulence, where local isotropy permits estimating one-point derivative moments by their isotropic forms, the viscous term may be negligible. Then the net effect of the pressure-velocity covariance terms is probably to destroy shear stress, because the other remaining term certainly creates it (Rotta 1962). There is no exact basis on which to drop terms from (2.7).

We can write an array of second moment equations for the vorticity fluctuations, but we save space by showing only the *mean square turbulent vorticity* balance ($\bar{\gamma} \equiv \overline{\omega_k \omega_k}$), which simplifies to

$$\frac{\partial \bar{\gamma}}{\partial t} = 2\overline{\omega_1 \omega_2}\frac{\partial \bar{U}_1}{\partial x_2} - 2\overline{\omega_j\frac{\partial u_j}{\partial x_3}}\frac{\partial \bar{U}_1}{\partial x_2} + 2\overline{\omega_i \omega_k\frac{\partial u_i}{\partial x_k}} - 2\nu\overline{\frac{\partial \omega_i}{\partial x_k}\frac{\partial \omega_i}{\partial x_k}}. \tag{2.8}$$

The first term on the right side is production by mean strain-rate stretching of turbulent vortex lines, the second (noting that the $-\partial \bar{U}_1/\partial x_2$ in this term was the mean vorticity component $\bar{\Omega}_3$) is production by local strain-rate fluctuations acting upon the mean vorticity, the third is self-amplification by turbulent stretching of turbulent vorticity (Taylor 1938). The last term is viscous destruction rate. Of all the missing terms, the one which may be most important in general shear flows is the rate of production of $\overline{\omega_j \omega_j}$ from $\bar{\Omega}_j \bar{\Omega}_j$: $-\overline{\omega_i u_k}\,(\partial \bar{\Omega}_i/\partial x_k)$.

The foregoing moment equations tell us that, if we could set up an exactly homogeneous turbulent shear flow at an instant of time, the mean velocity gradient would remain constant. They do not tell us whether the homogeneous turbulence structure would be independent of time.

2.2. *Estimates with local isotropy*

In order to be able to make rough estimates of the time evolution of homogeneous shear flow, we assume a Reynolds number so large that local isotropy allows all derivative moments to be approximated by their isotropic turbulence values. With the turbulent dissipation rate represented by ϵ, equations (2.5) to (2.8) are approximately

$$\frac{d\bar{e}}{dt} = -\overline{u_1 u_2}\frac{d\bar{U}_1}{dx_2} - \epsilon \quad \text{(exact)}, \tag{2.9}$$

$$\left.\begin{aligned} \frac{d\bar{e}_{(1)}}{dt} &\approx -\overline{u_1 u_2}\frac{d\bar{U}_1}{dx_2} + \frac{1}{\rho}\overline{p\frac{\partial u_1}{\partial x_1}} - \tfrac{1}{3}\epsilon, \\ \frac{d\bar{e}_{(2)}}{dt} &\approx \frac{1}{\rho}\overline{p\frac{\partial u_2}{\partial x_2}} - \tfrac{1}{3}\epsilon, \\ \frac{d\bar{e}_{(3)}}{dt} &\approx \frac{1}{\rho}\overline{p\frac{\partial u_3}{\partial x_3}} - \tfrac{1}{3}\epsilon, \end{aligned}\right\} \tag{2.10}$$

$$\frac{d}{dt}(-\overline{u_1 u_2}) \approx \overline{u_2^2}\frac{d\bar{U}_1}{dx_2} - \frac{1}{\rho}\overline{p\left(\frac{\partial u_1}{\partial x_2} + \frac{\partial u_2}{\partial x_1}\right)}, \tag{2.11}$$

$$\frac{d\bar{\gamma}}{dt} \approx 2\overline{\omega_i \omega_k \frac{\partial u_i}{\partial x_k}} - 2\nu\overline{\frac{\partial \omega_i}{\partial x_k}\frac{\partial \omega_i}{\partial x_k}}. \tag{2.12}$$

Since the vorticity is a velocity derivative, we insert the isotropic forms for the terms on the right side of (2.12):

$$\frac{d\bar{\gamma}}{dt} \approx \frac{7\cdot 2^{\frac{1}{2}}}{3^{\frac{5}{2}}}\bar{e}^{\frac{3}{2}}\, k'''(0) + \tfrac{14}{9}\nu\bar{e}f^{\mathrm{iv}}(0), \tag{2.13}$$

where f and k are the isotropic scalar double and triple correlation coefficient functions with velocity components along the line joining the two sampling points [e.g. Batchelor 1953, equation (5.5.8)].

Experiments have shown (Taylor 1938) that in nearly isotropic turbulence the (negative) viscous term dominates the right side of (2.12). If the same relative magnitudes occur in locally isotropic homogeneous shear flow, then $d\bar{\gamma}/dt < 0$, so the large Reynolds number case will not be stationary. The restriction to homogeneity and the assumption of local isotropy have combined to eliminate all contributions of the mean flow field to turbulent vorticity production, so the turbulent vorticity apparently would decay.

With local isotropy, $\bar{\gamma} \equiv \overline{\omega_k \omega_k} = 5\overline{u_i u_i}/\lambda^2$. Since (2.9) includes energy production, $\bar{e}$ would not decay as rapidly as in isotropic turbulence. Therefore, if $d\bar{\gamma}/dt$ were roughly the same for the two cases, the Taylor microscale λ would grow more rapidly in the shear flow.

The foregoing discussion suggests that a homogeneous turbulent shear flow might not remain stationary in time. For our wind tunnel experiment this suggests non-stationarity in a convected Eulerian frame moving at the centreline speed U_c. That implies in turn that the turbulence field must show some downstream inhomogeneity. The empirical amounts of spatial inhomogeneity, and of temporal non-stationarity in the convected frame, are discussed in § 5.1.

3. Experimental apparatus

3.1. *The wind tunnel and the shear-turbulence generator*

The wind tunnel is the one used by Rose (1966). In order to avoid the lateral gradients in turbulence scale which persisted behind his grid of non-uniform rod spacing, we devised a shear-turbulence generator with periodic geometry across the outlet plane. The original plan was to use a row of individually powered slot jets, but overall system design simplicity and economy finally dictated the compromise of a 'grid' consisting of a row of parallel, equal-width channels having adjustable internal resistances (screens), figure 1. Operationally this is less convenient because, with a common air supply, adjustment of one channel affects the others.

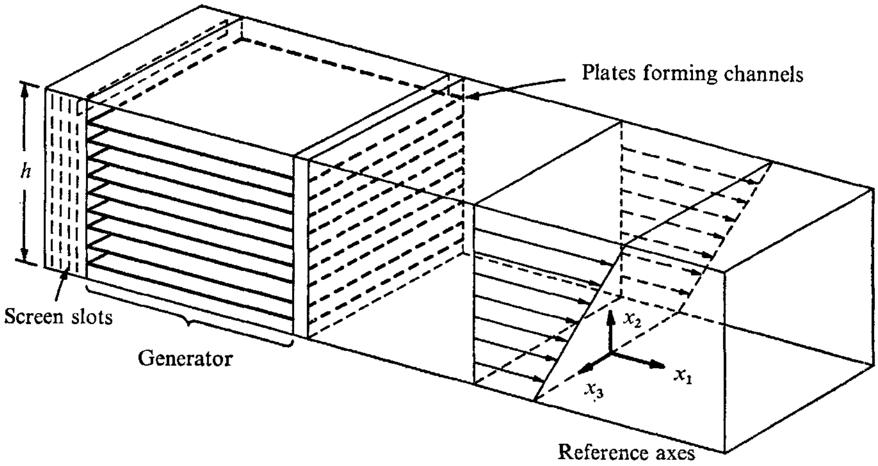

FIGURE 1. Schematic sketch of the 'homogeneous' turbulent shear flow generator and the downstream mean flow.

Co-ordinate	Mean component velocity	r.m.s. fluctuating-component velocity
x_1	$\bar{U}_1 = \bar{U}(x_2)$	u'_1
x_2	$\bar{U}_2 = 0$	u'_2
x_3	$\bar{U}_3 = 0$	u'_3

There are 12 channels, 24 in. long, with aluminium walls $\frac{1}{8}$ in. thick, spaced 1 in. on centres. These fall a bit short of having fully developed channel flow at the exit plane, but a $\frac{1}{8}$ in. square rod was installed on the long centreline of each channel exit plane in order to reduce the scale and characteristic time of the 'initial' turbulence. As will be seen in § 4, this allowed the turbulence to reach its nearly homogeneous asymptotic condition by about $x_1/h = 8{\cdot}5$, i.e. 8·5 ft. from the exit plane of the generator. This left about 2 ft. of nearly homogeneous turbulent shear flow for experimentation.

The mean velocity gradient is set by trial-and-error changing of the number and solidities of the screens spanning each channel. Mean velocity was measured with pitot tubes and constant-temperature hot-wire anemometers. The mean gradient for all measurements in this paper was $12{\cdot}9\,\mathrm{sec}^{-1}$, with a tunnel centre-line mean speed $U_c = 40{\cdot}7$ ft./sec. The walls were adjusted to give a mean static pressure constant within experimental accuracy.

It was hoped that the 'grid'-generated turbulence, which is inevitably non-uniform across the tunnel, would diffuse toward uniformity as it decayed, and that the turbulence field would eventually approach a good approximation to downstream constancy, as shear-produced turbulent energy and viscous dissipation came into balance. This hope was fairly well realized (§ 4).

3.2. *Instrumentation*

Velocity fluctuations were measured with Disa type 55 D 01† constant-temperature anemometers in conjunction with Disa type 55 D 10‡ linearizers. The linearizer output voltages were calibrated to known flow conditions in the wind tunnel test section with the shear-turbulence generator removed. The maximum u_1' turbulence level of the tunnel under these conditions was 0·15 %. An overheat ratio of 0·7 to 0·8 and a linearizer exponent setting of 2·22 (power) were found to yield linear calibration curves. Root mean squares of the fluctuating voltages were measured with the Disa type 55 D 35§ r.m.s. voltmeter, whose response is flat within ± 1 % of full scale from 1 Hz to 100 kHz.

Cross-component fluctuations, u_2', u_3', were measured with a standard symmetric X-array or with an asymmetric combination of normal and inclined wire. u_2 or u_3 sensitivity was obtained by yawing the probe $\pm 5^\circ$ (in a plane parallel to the two wires) in the test section of the empty tunnel.

Air temperature was monitored with a thermistor-bridge system and, with the aid of several heaters and a refrigerator ('air conditioner'), ambient temperature was kept sufficiently constant for no corrections to be required. Constancy of ambient temperature was important for mean velocity measurement, because the velocity gradient was fairly small; a $\frac{1}{2}$ in. translation in x_2 corresponds to only 1 % change in mean velocity.

Two-probe spatial velocity correlations were measured by direct multiplication of the two hot-wire signals followed by electronic integration in time. The multipliers used were either the G.P.S. model MU-500E-M or the G.P.S. model MU-405. Both have frequency responses flat (± 1 %) from d.c. to 50 kHz and accuracies of approximately ± 0·50 % of full scale amplitude. Time averages were taken with the S.O.S. model SI-100 integrator and Kramer timer. The data were corrected for a repeatable drift component of the integrator as determined with d.c. calibration. Nominal integration time was 90 sec.

---

† *Instruction Manual 55 D 01, second edition, Disa Elektronik A/S, Herlev, Denmark.*

‡ Instruction Manual 55 D 10, Disa Elektronik A/S, Herlev, Denmark.

§ Instruction Manual 55 D 35, Disa Elektronik A/S, Herlev, Denmark.

The traversing mechanism used was essentially the same as the one described by Kellogg (1965). Hot-wire probes were made of jeweller's broaches encased in Nu-Weld dental cement, with $\frac{1}{4}$ in. stainless-steel tube as main shafts. The upstream probe was bent up at an angle (see figure 45) to minimize downstream interference and to allow 'meshing' of the two probes to aid in determining zero separation. The x_1 and x_2 separation distances were read on dial gauges graduated in thousandths of an inch. Wires used for correlations were 0·00015 in. tungsten with copper-plated end supports. The sensing portions were 0·04 in. long.

Space-time correlations were determined in a similar manner, with time delay introduced by playing back the signals as recorded on a dual track (variable loop length) Sangamo model 482 RB tape recorder. Toward the end of the investigation a P.A.R. model 101 correlator became available and was used for some measurements. Some of the smallest delay times were obtained with an Ad-Yu model 801-D1 analogue delay line. A block diagram is shown in figure 2.

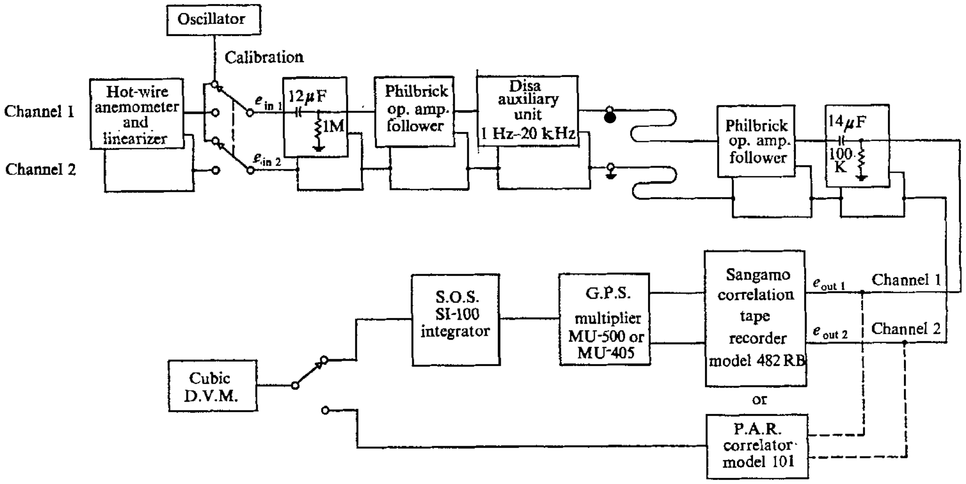

FIGURE 2. Block diagram of the space-time correlation circuits.

All of the time delay systems were checked with sine wave inputs. Unity minus the auto-correlation coefficient function, $1-R(\tau)$ in this test (figure 3), shows a slight departure from the required parabolic shape (slope = 2·0 on the log–log plot) as $\tau \to 0$. This departure must be due to slight inaccuracy ($\pm$ 1–2 %) in the correlation circuit.

This graphical technique was used to measure the spatial 'micro-scales' in the turbulence (§§4.2 and 4.3). As a cross-check on this method, λ_1 was also measured by differentiating the u_1 signal and assuming the validity of the 'Taylor approximation' (§4.2).

The frequency response of the differentiation circuit, a Disa model 55A06 R-C with nominal time constant of 0·2 msec, is shown in figure 4. Differentiation tends to reduce the signal-to-noise ratio, and it was necessary to correct differentiated data for noise.

Spectral measurements were made with a Dytronics model 720 (constant percent bandwidth) adjustable filter with 'high selectivity' setting in the lower-frequency range and a Hewlett Packard model 302A (fixed 6 Hz bandwidth) for high frequencies. The filter band shape calibrations are shown by Comte-Bellot & Corrsin (manuscript submitted). Data taken with the two instruments were overlapped at about 100 Hz as a check. In order to minimize the need for noise corrections, wires used for spectra were either 0·00009 in. diameter tungsten or 0·00005 in. diameter platinum/10 % rhodium. Lengths were on the order of the Kolmogorov microscale, 0·014 in., and frequency responses above 12 kHz. The spectral data were not corrected for filter shape or for finite sensing-element length.

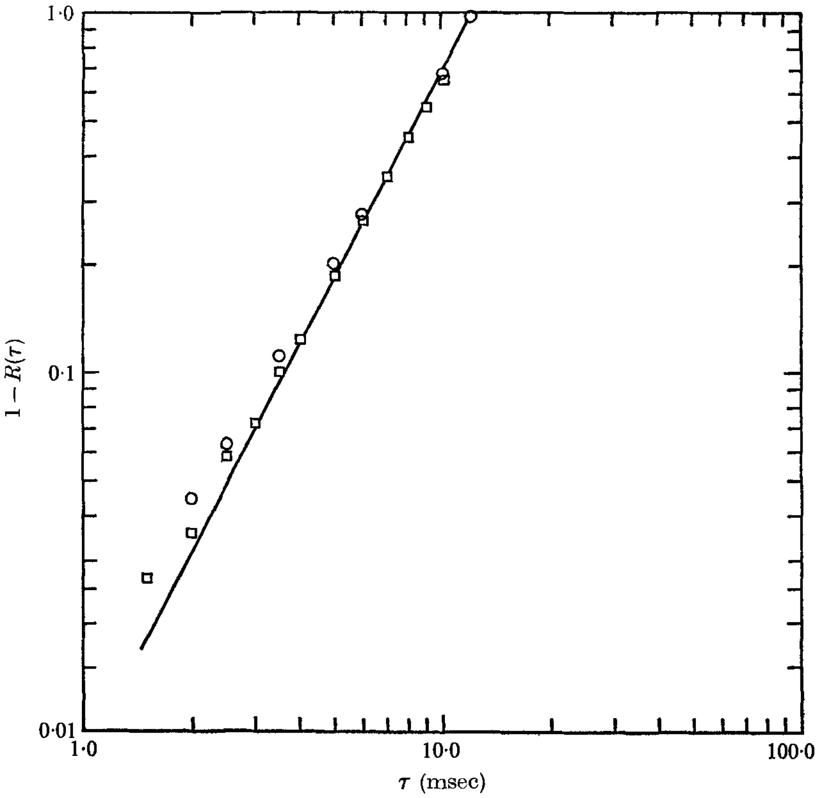

FIGURE 3. Performance checks of the two systems used for measuring correlation with time delay. Test signal is a sine wave of 20 Hz. ——, theoretical $R(\tau) = \cos 2\pi f\tau, f = 20$ Hz; ○, measured $R(\tau)$ W/tape recorder and G.P.S. multiplier; □, measured $R(\tau)$ W/P.A.R.

The turbulent shear stress spectrum (cross-spectrum of u_1 and u_2) was measured by two procedures which are not entirely independent. The first involves measuring the signal spectra of both wires in a symmetric X-array. Then, from the wire calibration constants and the measured u_1 and u_2 spectra one obtains the desired spectrum, essentially by subtracting. The other method consists in multiplying the narrow-band-pass-filtered outputs of a normal wire and an inclined wire from which the u_1 contribution has been electronically subtracted, and averaging this product.

The hot-wire anemometer unit is d.c. coupled. The magnetic tape system, using frequency modulation, is also faithful down to d.c. The effective high-frequency limitation of the tape, presumably due to mechanical fluctuation, is shown in figure 5 in terms of the ability of the system to reproduce a correlation function of 1·0 for τ equal to any integral number of periods of input sine waves.

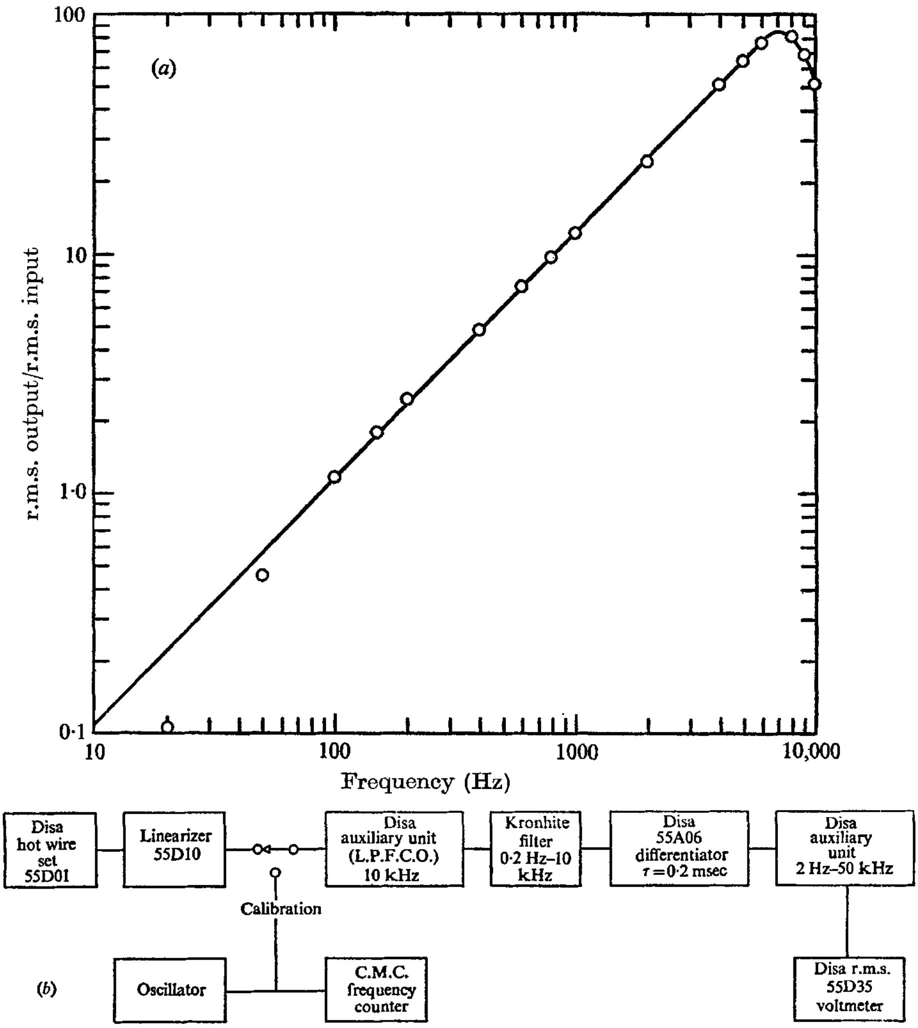

FIGURE 4. Frequency response and block diagram of differentiating circuit.

The frequency response of the rest of the electronic system, with a deliberate low-frequency cut-off, is shown in the same figure.

4. Measurements

4.1. *Flow development*

The flow field just downstream of the generator is of course non-uniform. We are interested in attaining an 'asymptotic' state which is as nearly homogeneous as possible. The approach toward homogeneity at least in planes normal to the mean flow turns out to be more rapid for the mean velocity than for the turbulence. This behaviour was observed by Rose, and is consistent with that of familiar turbulent shear flows (such as jets).

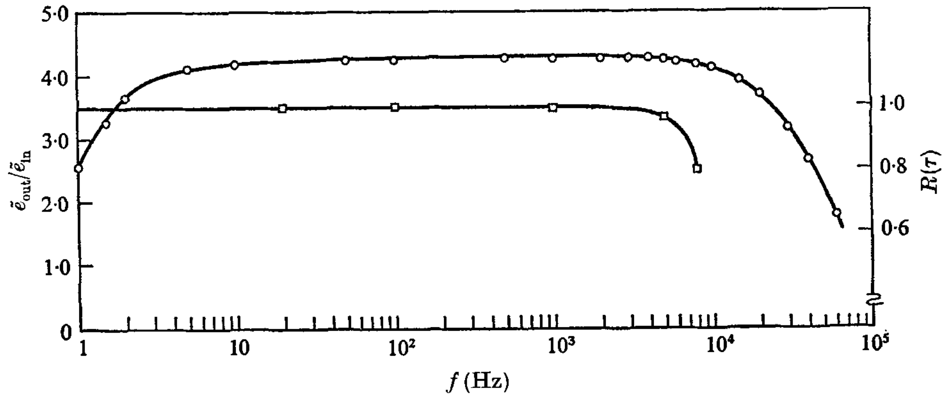

FIGURE 5. Frequency response of correlation circuit and the effective response of the Sangamo tape recorder used in f.m. mode. ○, $\tilde{e}_{\mathrm{out}}/\tilde{e}_{\mathrm{in}}$, frequency response of space-time correlation circuit W/cables to tape recorder; □, $R(\tau)$, effective correlation response of tape recorder (sine wave input, $\tau = 0$).

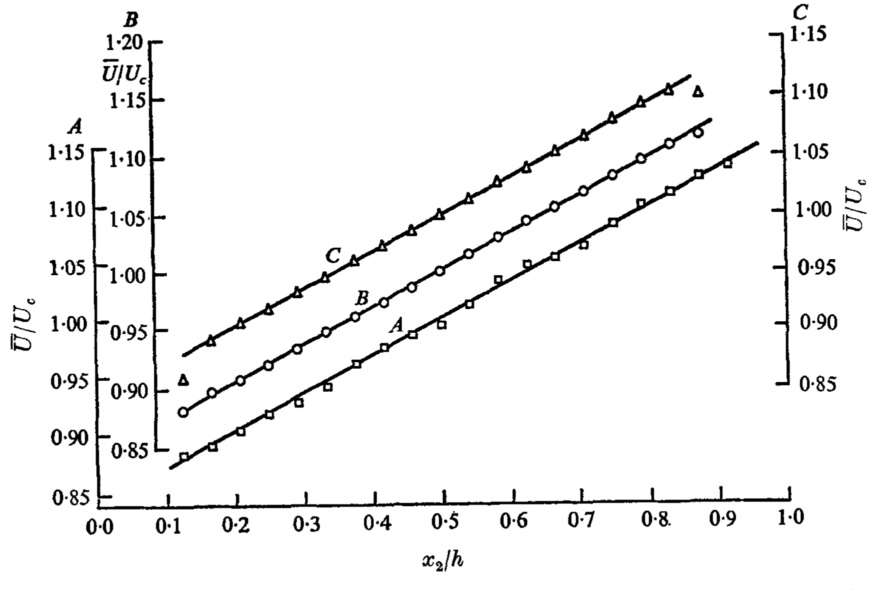

FIGURE 6. Mean velocity profiles at three distances downstream of the generator. h is the height of wind tunnel test section, 12 in. Departures of data points from the reference straight lines were reproducible. Most data were taken in the region $8{\cdot}5 \leqslant x_1/h \leqslant 10{\cdot}5$. □, $x_1/h = 3{\cdot}33$, strain rate $= 12{\cdot}94\ \mathrm{sec}^{-1}$; ○, $x_1/h = 6{\cdot}67$, strain rate $= 12{\cdot}96\ \mathrm{sec}^{-1}$; △, $x_1/h = 9{\cdot}50$, strain rate $= 12{\cdot}92\ \mathrm{sec}^{-1}$.

Lateral distributions of mean velocity $\overline{U}/U_c$ obtained with pitot tube and micromanometer at three downstream locations are shown in figure 6. The ordinate origins are displaced for clarity. The centreline velocity U_c was nearly constant down the tunnel, providing a check on the wall compensation for boundary-layer growth. The 12·9 sec^{-1} mean strain rate, about the same as Rose's (1966) 13·7 sec^{-1}, does not change significantly downstream. At $x_1/h = 9{\cdot}50$, where h is the tunnel height, the boundary layers have penetrated to about 0·15 inward on the bottom and top walls.

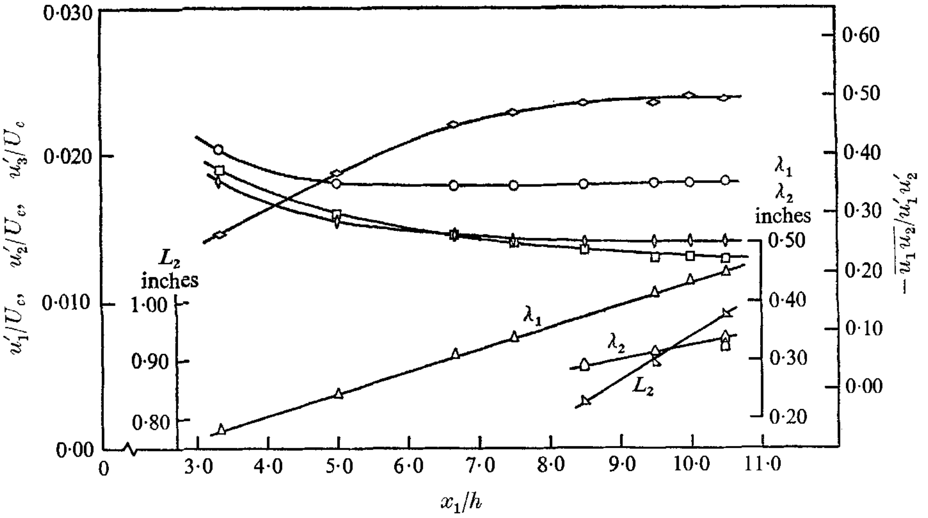

FIGURE 7. Tunnel centreline development of turbulence levels, shear stress and some scales. (Grid exit plane at $x_1/h = 0$.) Centreline development : ○, u_1'/U_c; □, u_2'/U_c; ◊, u_3'/U_c; ◇, $\overline{u_1u_2}/u_1'u_2'$.

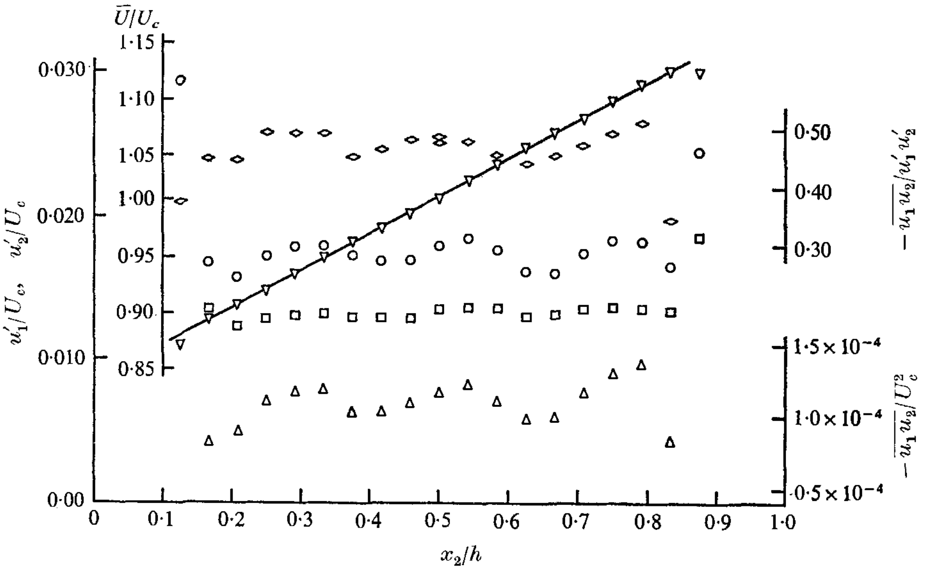

FIGURE 8. Lateral profiles of some turbulence properties at $x_1/h = 8{\cdot}5$, $x_3/h = 0$. ▽, $\bar{U}/U_c$; ○, u_1'/U_c; □, u_2'/U_c; △, $-\overline{u_1u_2}/U_c^2$; ◇, $-\overline{u_1u_2}/u_1'u_2'$.

The development of the turbulence field is shown in figures 7–10. Figure 7 shows the centreline distribution of turbulence intensities, shear stress and shear correlation coefficient. The turbulence intensities decay from generator-produced values to nearly constant values which are presumably characteristic of the mean shear sustaining the turbulence and of the (slowly growing) scales, and hence of the generator as well. The u_1' component reaches a level value before u_2', u_3' and the

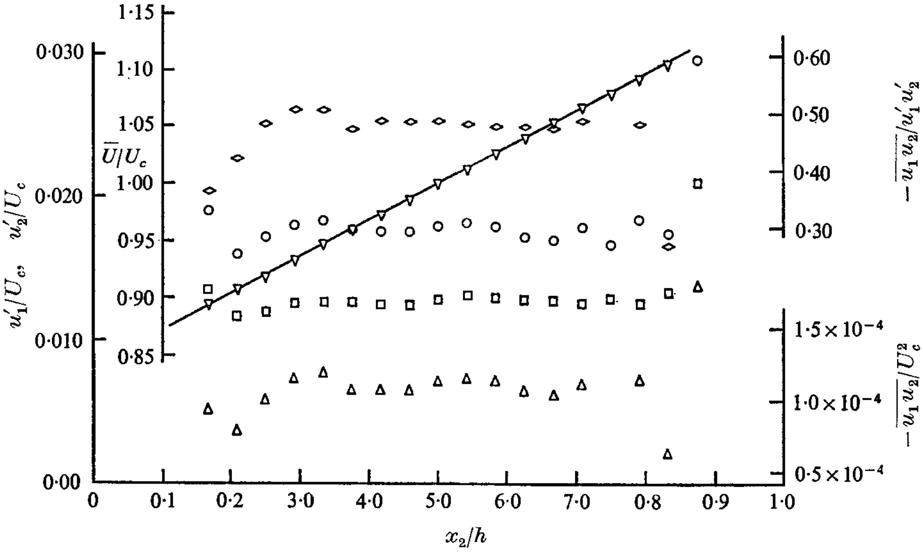

FIGURE 9. Lateral profiles of some turbulence properties at $x_1/h = 9{\cdot}5$, $x_3/h = 0$. ▽ ,$\bar{U}/U_c$; ○, u_1'/U_c; □, u_2'/U_c; △, $-\overline{u_1u_2}/U_c^2$; ◇, $-\overline{u_1u_2}/u_1'u_2'$.

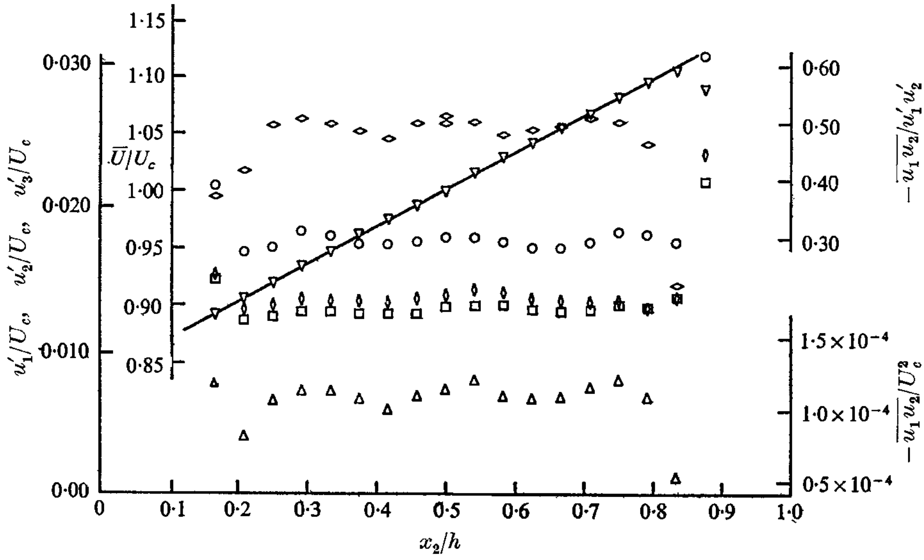

FIGURE 10. Lateral profiles of some turbulence properties at $x_1/h = 10{\cdot}0$, $x_3/h = 0$. ▽, $\bar{U}/U_c$; ○, u_1'/U_c; □, u_2'/U_c; ◇, $-\overline{u_1u_2}/u_1'u_2'$; ◊, u_3'/U_c; △, $-\overline{u_1u_2}/U_c^2$.

shear stress. This behaviour, also observed by Rose, may result from the fact that in rectilinear flows the production of turbulent energy occurs entirely in the u_1 component (e.g. Corrsin 1957), and to the fact that, since u'_1 has more energy, it is relatively less 'sensitive' to a given amount of energy exchange. The 'asymptotic' levels of u'_1, u'_2 and u'_3 are 1·8, 1·3 and 1·4 % respectively of U_c. The apparently asymptotic value of the shear correlation coefficient is about 0·50, the same order as is commonly measured in traditional shear flows away from solid or free boundaries.

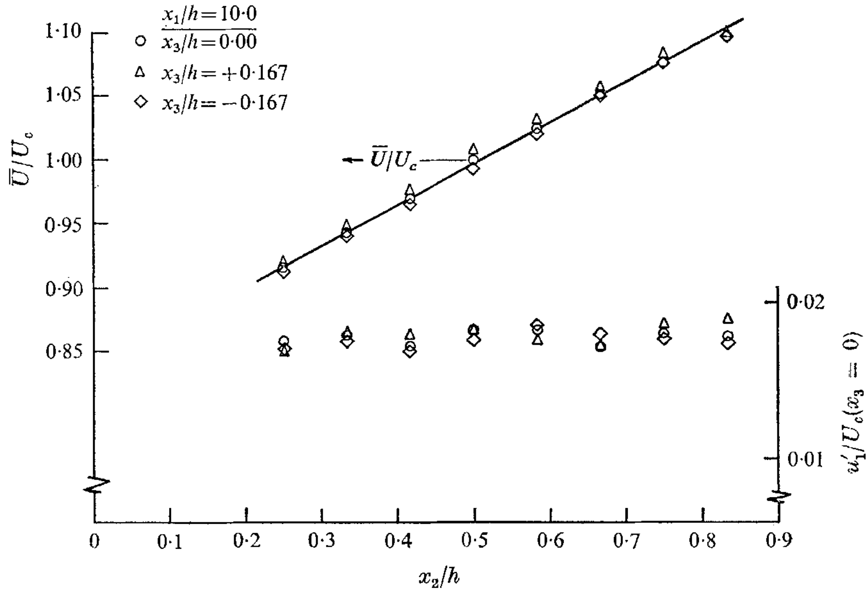

FIGURE 11. Profiles of mean and turbulent velocities at three x_3 stations across the test section—a test of two-dimensionality. $x_1/h = 10·0$: ○, $x_3/h = 0·00$; △, $x_3/h = +0·167$; ◇, $x_3/h = -0·167$.

Mean velocity and u'_1 data were also taken at $x_1/h = 11·0$. They agreed with the values at 10·0 and 10·5, but the tunnel exit plane was located at $x_1/h = 12·0$, and we wanted to avoid possible end effects, so few measurements were made beyond $x_1/h = 10·5$. Measurements showed $|\overline{u_1 u_3}/u'_1 u'_3|$ never exceeding 0·01 along the centreline. This suggests that, as far as the turbulence was concerned, the mean motion was effectively two-dimensional.

Lateral distributions of the r.m.s. turbulent velocities and the Reynolds stress in the ($x_3 = 0$) midplanes at different downstream locations are shown in figures 8–10. These mean velocity data were obtained with a linearized, constant-temperature hot-wire anemometer.

The grid-created non-uniformities in u'_1 and shear stress decrease as x_1/h increases until, at $x_1/h = 8·5$, the turbulent field becomes reasonably uniform. Residual variations are not identifiably related to grid dimensions. Figure 10 presents the data for $x_1/h = 10·0$, including u'_3. Excluding the boundary layers, the mean strain rate and the turbulence intensities are nearly constant across the flow field. The shear stress $-\overline{u_1u_2}/U_c^2$ on an expanded scale appears rather non-uniform, but the average is $1{\cdot}11 \times 10^{-4}$ with standard deviation of $\pm 0{\cdot}05 \times 10^{-4}$, about the uncertainty for these measurements.

The intensities and shear stress increase markedly at the bottom and top wall boundary layers. Some influence of the boundary layers is detectable to values of $\Delta x_2/h = 0{\cdot}30$ and $0{\cdot}20$ respectively from the walls.

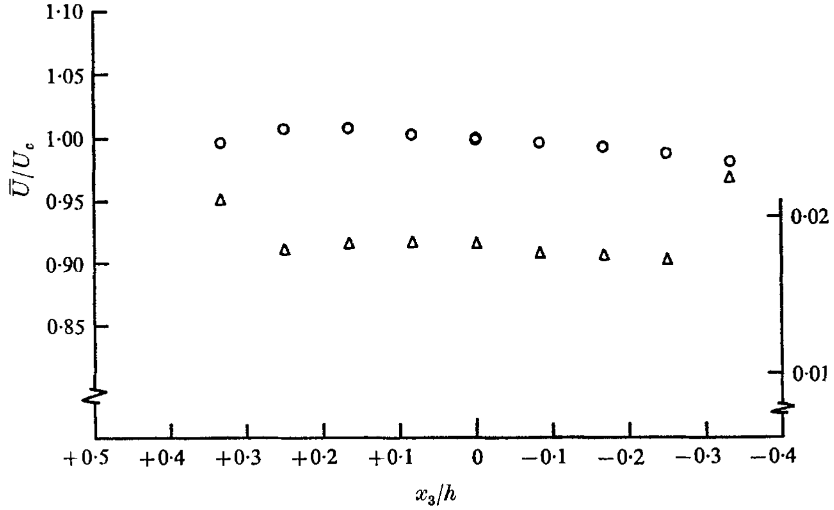

FIGURE 12. Profiles of mean and turbulent velocities in the x_3 direction, normal to both mean flow and principal velocity gradient. $x_1/h = 10{\cdot}0$, $x_2/h = 0{\cdot}50$. ○, $\overline{U}/U_c$; △, u_1'/U_c.

Lateral distributions of $\overline{U}/U_c$ and u_1'/U_c at $x_1/h = 10{\cdot}0$ at three values of x_3/h (figure 11) show fairly good two-dimensionality. Figure 12 is an x_3/h profile at $x_2/h = 0{\cdot}50$ and $x_1/h = 10{\cdot}0$. The slight (undesirable) $\partial\overline{U}/\partial x_3$ is about $1{\cdot}2\,\text{sec}^{-1}$. This gives $|\partial\overline{U}/\partial x_3|/|\partial\overline{U}/\partial x_2| = 0{\cdot}09$, a departure from the 'design' flow which appears to be of no dynamic significance in the turbulence because the corresponding turbulent energy production term, $-\overline{u_1u_3}\,\partial\overline{U}/\partial x_3$, is only 1/500 of the principal production term, $-\overline{u_1u_2}\,\partial\overline{U}/\partial x_2$.

The small departure from two-dimensionality suggested the possibility of secondary flow. A check using a single yawed wire as direction meter detected none.

4.2. *Two-point spatial correlations and auto-correlations of velocity*

The two-point velocity correlation functions are the simplest measures of spatio-temporal structure and they provide us with an additional test of homogeneity.

The u_1 double correlation coefficient is defined as

$$R_{11}(r_1, r_2, r_3; \tau) \equiv \frac{\overline{u_1(\mathbf{x}, t)\, u_1(\mathbf{x}+\mathbf{r}, t+\tau)}}{\sqrt{\overline{u_1^2}(\mathbf{x})}\sqrt{\overline{u_1^2}(\mathbf{x}+\mathbf{r})}},$$

with $u_1(\mathbf{x}, t)$ the turbulent velocity component in the mean flow direction at a position $\mathbf{x}$ and time t. The overbar denotes a time average, r_1, r_2 and r_3 are Cartesian components of the separation vector $\mathbf{r}$, and τ is time delay, which is zero for simple space correlation.

The 'longitudinal' Taylor microscale λ_1 is defined by

$$\lambda_1^2 \equiv \frac{2\overline{u_1^2}}{\overline{(\partial u_1/\partial x_1)^2}}, \tag{4.1}$$

and two 'lateral' microscales λ_2 and λ_3 are defined similarly, with the u_1 derivatives taken with respect to x_2 and x_3 respectively.

The 'longitudinal' integral scale L_{11} is defined by the relation

$$L_{11} \equiv \int_0^\infty R_{11}(r_1, 0, 0; 0)\, dr_1, \tag{4.2}$$

and lateral integral scales L_{12} and L_{13} are defined similarly, with the integration of $R_{11}(0, r_2, 0; 0)$ and $R_{11}(0, 0, r_3; 0)$.

In the event that a correlation coefficient became negative, however, the upper limit of integration in the definition was *arbitrarily* taken as the position of its first zero. This gives a measure of spatial large-structure without introducing the complexities associated with the a.c. coupling of some of the circuits. *As a matter of principle, a.c.-coupled circuits can give only zero as the value of an integral scale,* because the integral scale is proportional to the d.c. intercept of the energy spectrum. For discussion of this point, see, for example, Comte-Bellot & Corrsin (submitted for publication).

In statistically steady homogeneous turbulence (see, for example, Batchelor 1953), for vanishing r_1,

$$R_{11}(r_1, 0, 0; 0) \rightarrow 1 - r_1^2/\lambda_1^2, \tag{4.3}$$

and thus

$$\lambda_1^2 = -2\Big/\left[\frac{\partial^2}{\partial r_1^2} R_{11}(r_1, 0, 0; 0)\right]_{r_1=0},$$

so the $r_1 \rightarrow 0$ curvature of R_{11} is a convenient method for measuring λ_1. For vanishing time delay we have the analogous expression

$$R_{11}(0, 0, 0; \tau) \rightarrow 1 - (\tau^2/\lambda_\tau^2). \tag{4.4}$$

where $\lambda_\tau^2 \equiv 2\overline{u_1^2}/\overline{(\partial u_1/\partial t)^2}$. When the 'Taylor approximation' holds (see the end of this section), $\lambda_\tau \doteq \lambda_1/\overline{U}$ and the measurements can be checked against each other.

Two-point spatial correlation functions were measured at

$$\begin{aligned} x_1/h &= 8{\cdot}5 \quad [R_{11}(r_1, 0, 0; 0) \text{ and } R_{11}(0, r_2, 0; 0)], \\ &= 9{\cdot}5 \quad [R_{11}(0, r_2, 0; 0)] \\ \text{and} \quad &= 10{\cdot}5 \quad [R_{11}(0, r_2, 0; 0)]. \end{aligned}$$

Only the 8·5 data (at 'large r'), figure 13, and the 10·5 data, figure 14, are presented. The λ's and L's from the omitted data are included in figure 17.

Following Rose (1966), we inspect these functions on both semi-log plot [which emphasizes the small correlation ('large r') region] and log–log plot [where $1 - R_{11}$ emphasizes the 'small r' region]. The latter is useful for λ determination by fitting the 'best' straight line of slope 2.0. For small probe separation, both flow interaction effects and small circuit errors can cause appreciable errors in the λ determination.

Probe interaction is particularly severe when the downstream hot-wire is in the wake of the upstream one. Tests on this effect in terms of space and space-time correlations showed that this configuration had to be avoided for $r_1 < 4$ in. For this range of r_1, correlations were obtained by extrapolation.

Extrapolation (or interpolation) to $r_2 = 0$ was made simpler by the empirical discovery that $R_{11}(r_1, r_2, 0; 0)$ and $R_{11}(r_1, r_2, 0; \tau)$ were even functions of r_2 within our experimental accuracy, even though this has not been established theoretically from the symmetry properties of the correlation tensor in homogeneous shear flow. Thus values of the correlations $R_{11}(r_1, 0, 0; 0)$ and $R_{11}(r_1, 0, 0; \tau)$ were obtained by traversing the downstream wire along r_2 for each r_1, then extrapolating/interpolating to $r_2 = 0$, assuming R_{11} even in r_2. Least-squares parabolas were used.

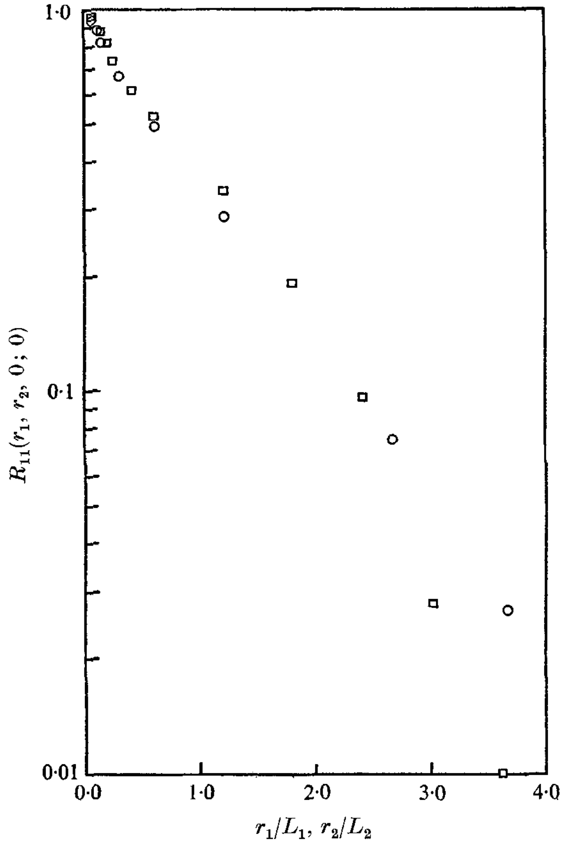

FIGURE 13. Spatial correlation functions along the flow direction and along the velocity gradient direction. Both decrease roughly exponentially. $x_1/h = 8{\cdot}50$, $x_2/h = 0{\cdot}50$, $x_3/h = 0{\cdot}0$. ○, $R_{11}(r_1, 0, 0)$, $L_1 = 1{\cdot}64$ in.; □, $R_{11}(0, r_2, 0)$, $L_2 = 0{\cdot}83$ in. See equation (4.6).

Probe interference effects and inaccuracies in electronic multiplication limited the accuracy of the microscales determined from these correlation data to an estimated ± 5 % maximum.

The longitudinal and lateral correlation coefficients $R_{11}(r_1, 0, 0; 0)$ and $R_{11}(0, r_2, 0; 0)$ are compared in figure 13 for $x_1/h = 8{\cdot}5$. They are nearly similar,

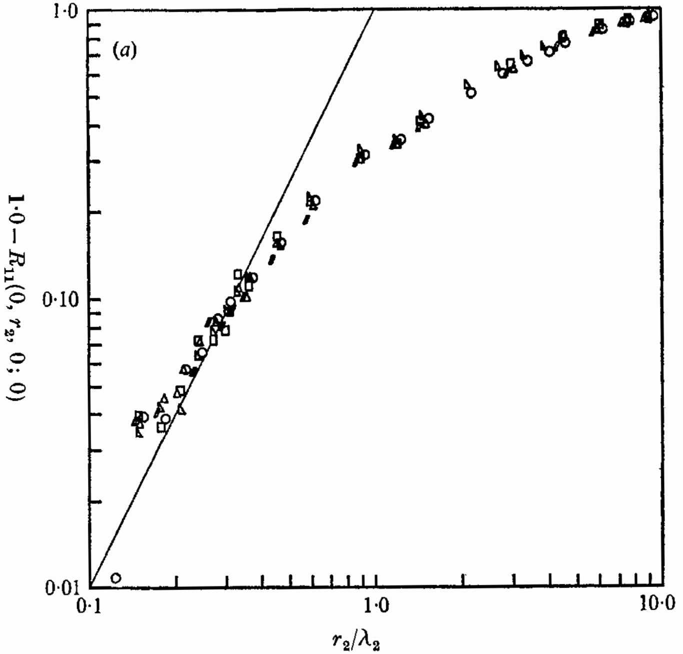

FIGURE 14(*a*). Lateral homogeneity of correlation functions, plotted to emphasize small structure, especially Taylor 'microscale'. $x_1/h = 10{\cdot}5$. ○, $x_2/h = 0{\cdot}50$, $r_2 > 0$, $\lambda_2 = 0{\cdot}32$ in.; ◺, $x_2/h = 0{\cdot}50$, $r_2 < 0$, $\lambda_2 = 0{\cdot}34$ in.; □, $x_2/h = 0{\cdot}375$, $r_2 > 0$, $\lambda_2 = 0{\cdot}33$ in.; ▱, $x_2/h = 0{\cdot}25$, $r_2 > 0$, $\lambda_2 = 0{\cdot}35$ in.; △, $x_2/h = 0{\cdot}75$, $r_2 < 0$, $\lambda_2 = 0{\cdot}33$ in.

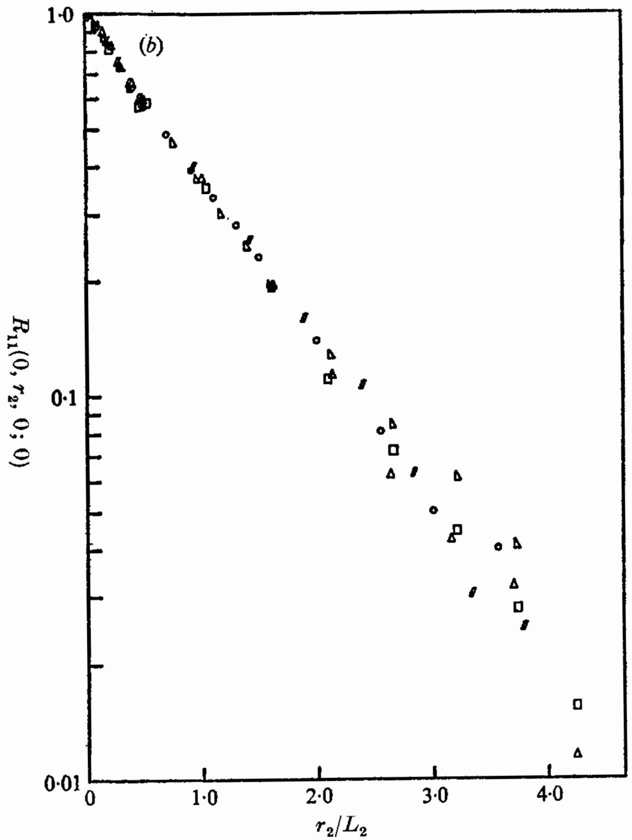

FIGURE 14(*b*). Lateral homogeneity of correlation functions, plotted to emphasize large structure. $x_1/h = 10{\cdot}5$. ○, $x_2/h = 0{\cdot}50$, $r_2 > 0$, $L_2 = 0{\cdot}98$ in.; ◺, $x_2/h = 0{\cdot}50$, $r_2 < 0$, $L_2 = 0{\cdot}94$ in.; □, $x_2/h = 0{\cdot}375$, $r_2 > 0$, $L_2 = 0{\cdot}94$ in.; ▱, $x_2/h = 0{\cdot}25$, $r_2 > 0$, $L_2 = 1{\cdot}05$ in.; △, $x_2/h = 0{\cdot}75$, $r_2 < 0$, $L_2 = 0{\cdot}95$ in.

in strong contrast to the case of isotropic turbulence, where the latter is observed to pass through zero at r/L of order 2, well before the former.

Figure 14 (*a*), (*b*) shows further tests of the lateral homogeneity as indicated by correlation functions measured at five positions along the mean velocity gradient direction, all at $x_1/h = 10{\cdot}5$. '$r_2 > 0$' and '$r_2 < 0$' indicate that the movable probe was in a region of velocity higher and lower respectively than that at the fixed probe. There was a 6 % variation in the microscales and 4 % in the integral scales, and some systematic trends. The less regular variations seem consistent with the uncertainty of these measurements. Like the corresponding data of Rose, figures 13 and 14 (*b*) show an extended linear range, implying a range of r in which $R_{11}(r_1, 0, 0; 0)$ and $R_{11}(0, r_2, 0; 0)$ are well approximated by simple exponential functions.

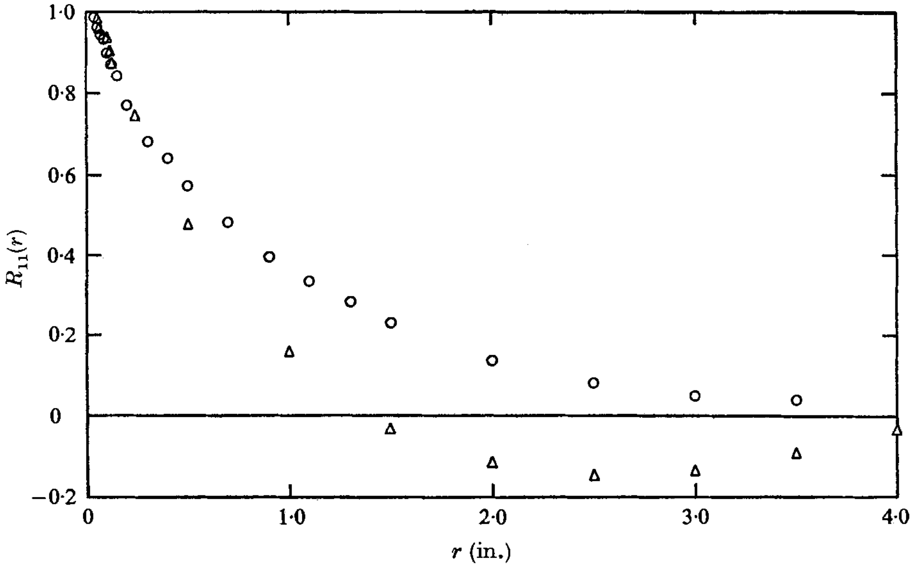

FIGURE 15. Spatial correlation functions along r_2, the velocity gradient direction, and along r_3, normal to both gradient and mean velocity directions. In isotropic turbulence they would be identical. ○, $R_{11}(r_2)$, $x_1/h = 10{\cdot}5$, $x_2/h = 0{\cdot}50$, $x_3/h = 0{\cdot}0$; △, $R_{11}(r_3)$, $x_1/h = 10{\cdot}5$, $x_2/h = 0{\cdot}50$, $x_3/h = 0{\cdot}0$.

A notable contrast with isotropic turbulence is that lateral correlation taken along the velocity gradient direction in shear flow seems to have no significant tendency to a negative region. As pointed out by Rose, this is observed in the traditional flows as well as in the 'homogeneous' one. Of course, incompressible mass conservation requires 'back flow' in terms of a negative transverse correlation region for R_{11} somewhere in the $(0, r_2, r_3)$ plane. It shows up in $R_{11}(0, 0, r_3; 0)$, which has a negative region stronger than that observed in isotropic turbulence; figure 15 contrasts the two lateral correlations along r_2 and r_3. In a precisely homogeneous turbulence, the constant-density continuity equation can be shown to require, for example, that

$$\iint_{-\infty}^{\infty} R_{11}(0, r_2, r_3; 0)\, dr_2 dr_3 = 0.$$

This kind of relation was pointed out first by Taylor (1936), with pipe flow as the example.

Since the a.c. coupling in our signal-processing network requires that all measured correlation functions have zero integrals, the measured $R_{11}(0, r_2, 0; 0)$ would also have shown a negative region at large enough r_2. But this would then reflect a property of the network rather than of the turbulence.

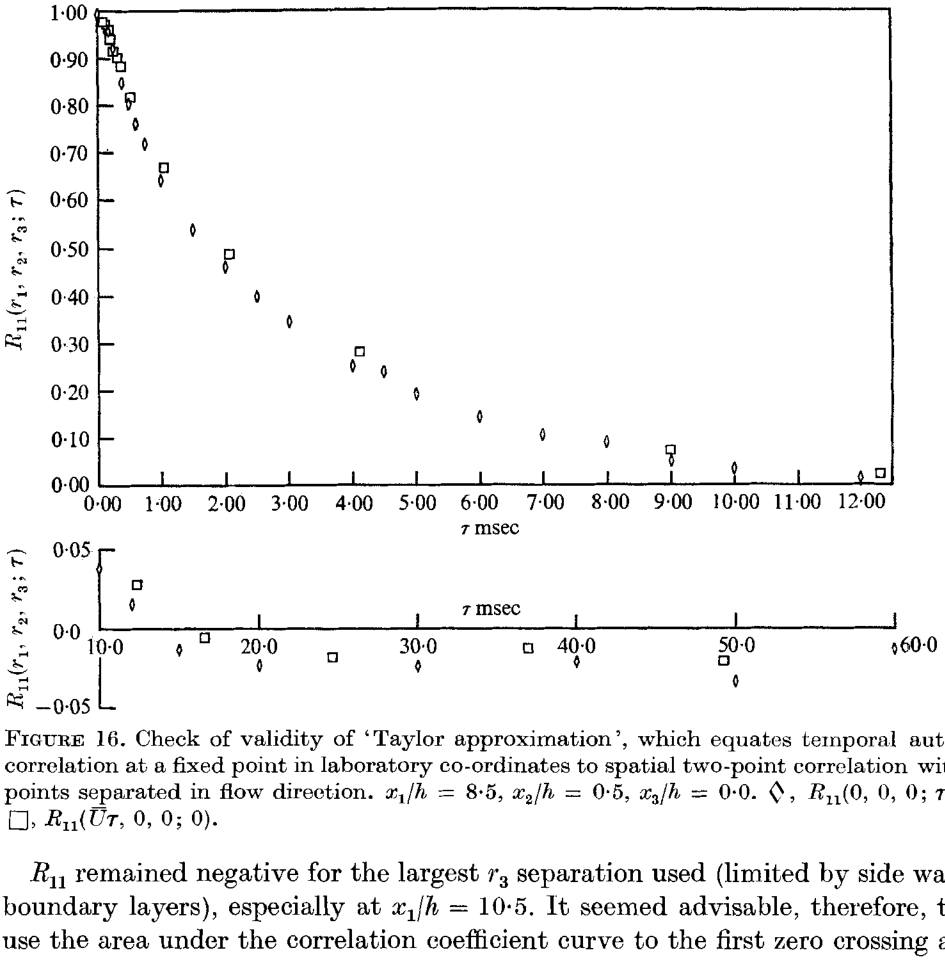

FIGURE 16. Check of validity of 'Taylor approximation', which equates temporal auto-correlation at a fixed point in laboratory co-ordinates to spatial two-point correlation with points separated in flow direction. $x_1/h = 8{\cdot}5$, $x_2/h = 0{\cdot}5$, $x_3/h = 0{\cdot}0$. ◇, $R_{11}(0, 0, 0; \tau)$; □, $R_{11}(\overline{U}\tau, 0, 0; 0)$.

R_{11} remained negative for the largest r_3 separation used (limited by side wall boundary layers), especially at $x_1/h = 10{\cdot}5$. It seemed advisable, therefore, to use the area under the correlation coefficient curve to the first zero crossing as a measure of 'integral scale'. Presumably this negative region is more a fluid-dynamic phenomenon than a network property. This arbitrary scale is called L_3.

A single wire auto-correlation measurement (in time) on the tunnel centreline at $x_1/h = 8{\cdot}5$ is shown in figure 16. Included for comparison are the $R_{11}(r_1, 0, 0; 0)$ data, with the transformation $\tau = r_1/\overline{U}$. The two functions are nearly equal, indicating good agreement with the 'Taylor approximation' (or 'hypothesis') identifying the temporal history at a fixed position with convected spatial structure, when the turbulence level is small enough [Lin 1953, Uberoi & Corrsin 1953; for more recent detailed discussion, see Lumley 1965, Comte-Bellot & Corrsin (manuscript submitted)]. This is consistent with, for example, the boundary-layer observations of Favre, Gaviglio & Dumas (1955).

4.3. *Taylor 'microscales'*

The distribution of longitudinal Taylor 'microscale' λ_1 along the test-section centreline is given in figure 17. Most of these values were obtained from time derivatives of the linearized hot-wire signal with the use of Taylor's approxima-

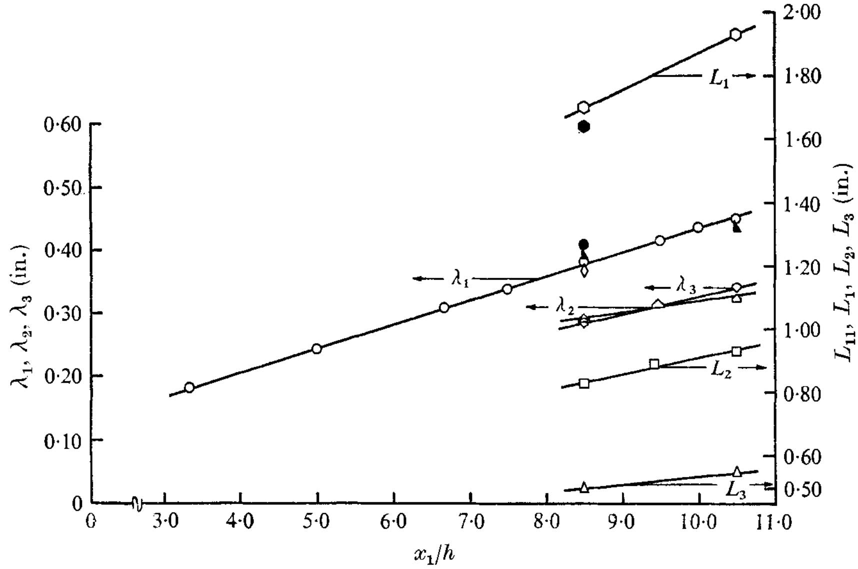

FIGURE 17. Growth of several integral scales and Taylor 'microscales' along the tunnel centreline. ●, λ_1 from $R_{11}(r_x, 0, 0; 0)$; ◣, λ_1 from $R_{11}(0, 0, 0; \tau)$; ◇, λ_1 from spectrum; ⬢, L_{11} from spectrum.

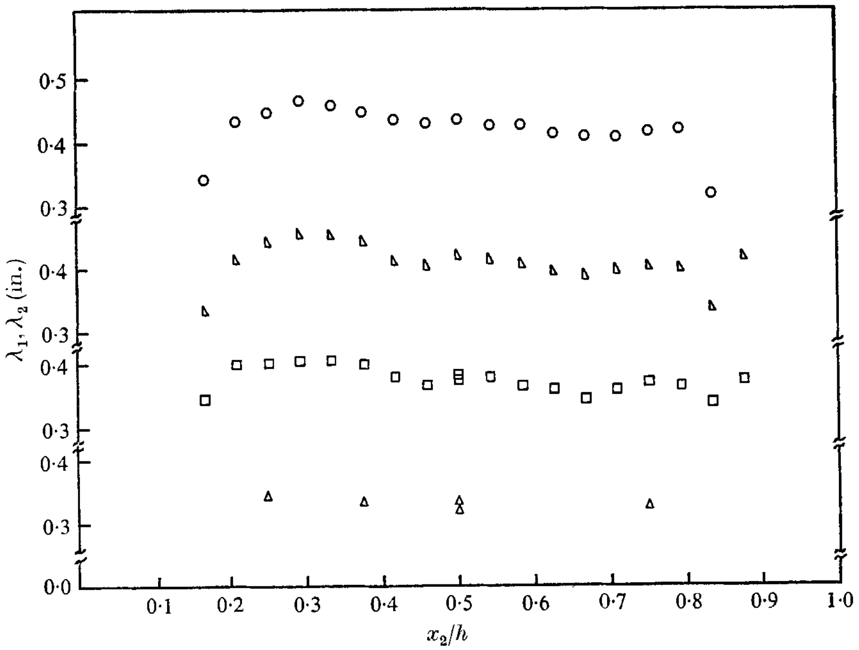

FIGURE 18. Lateral profiles of Taylor 'microscales'. △, λ_2, $x_1/h = 10{\cdot}5$; ◺, λ_1, $x_1/h = 9{\cdot}5$; □, λ_1, $x_1/h = 8{\cdot}5$; ○, λ_1, $x_1/h = 10{\cdot}0$.

tion (§4.2). These values are corrected for noise. As a check, three other kinds of measurements were used at $x_1/h = 8{\cdot}5$. The energy spectrum method is mentioned in the next section.

The lateral microscales λ_2 and λ_3 in figure 17 were measured from spatial correlation functions. All increase with increasing distance from the generator, even after the turbulent energies and shear have reached nearly constant values. This was found also by Rose (1966), and is presumably a natural trait of such flows, and an indication of the impossibility of maintaining a stationary, homogeneous turbulent shear flow (§5.1).

Distributions of λ_1 and λ_2 along the mean velocity gradient direction are shown in figure 18, with shifted origins. The lowest set of data is λ_2 at $x_1/h = 10{\cdot}5$ as determined from $R_{11}(0, r_2, 0; 0)$. The maximum variation is 6%. The upper three sets are λ_1 as determined from time derivatives at three downstream locations. The maximum variation at $x_1/h = 10{\cdot}0$ is 10%, excluding the two end points, which are in the boundary layers.

The values of these spatial microscales are consistent with local isotropy, i.e. $\lambda_1 \doteq \sqrt{2}\,\lambda_2 \doteq \sqrt{2}\,\lambda_3$.

4.4. *One-dimensional energy spectra and more on integral scales*

The one-dimensional energy spectra $F_1(k_1)$, $F_2(k_1)$, $F_3(k_1)$, whose integrals are $\overline{u_1^2}$, $\overline{u_2^2}$, $\overline{u_3^2}$, are presented in figures 19 and 21. Taylor's approximation in the form $k_1 \doteq 2\pi n/\overline{U}$ was used to convert frequency n to wave-number k_1, the x_1 component.

Figure 19 gives $\overline{u_1^2}$ spectra at $x_1/h = 8{\cdot}5$ and $10{\cdot}5$. The abscissa is ηk_1, where $\eta \equiv (\nu^3/\epsilon)^{\frac{1}{4}}$, the Kolmogorov microscale. The value of dissipation rate ϵ used is that given by the energy production rate because energy transport is negligible, and the production is measured with greater accuracy than the dissipation. The two spectra are not identical, although their integrals ($\overline{u_1^2}$) are sensibly equal. There is relatively less energy in the high wave-number region at $x_1/h = 10{\cdot}5$. This is consistent with the measured downstream growths of both λ_1 and integral scales, figure 17. The spectral equivalent of the hot-wire sensing-element length l_W is indicated. No wire length corrections were applied.

Integral scales of stationary random variables can be inferred from energy spectra simply from the Fourier transform connexion between auto-correlation and spectrum. For homogeneous turbulence, for example, the u_1 integral scale in the x_1 direction is

$$L_{11} \equiv \int_0^\infty R_{11}(r_1, 0, 0; 0)\,dr_1 = \frac{\pi}{2\overline{u_1^2}} F_1(0). \tag{4.5}$$

Thus the spectrum measurements contain the chance of another consistency check between two kinds of measurements. This check is not entirely explicit, however, because instrument limitations (the low-frequency cut-off) persuaded us to use as correlation function integral scale measure the integral of R_{11} only as far as its first zero: e.g.

$$L_1 \equiv \int_0^{{}_0r_1} R_{11}(r_1, 0, 0; 0)\,dr_1, \tag{4.6}$$

where $$R_{11}({}_0r_1, 0, 0; 0) \equiv 0.$$

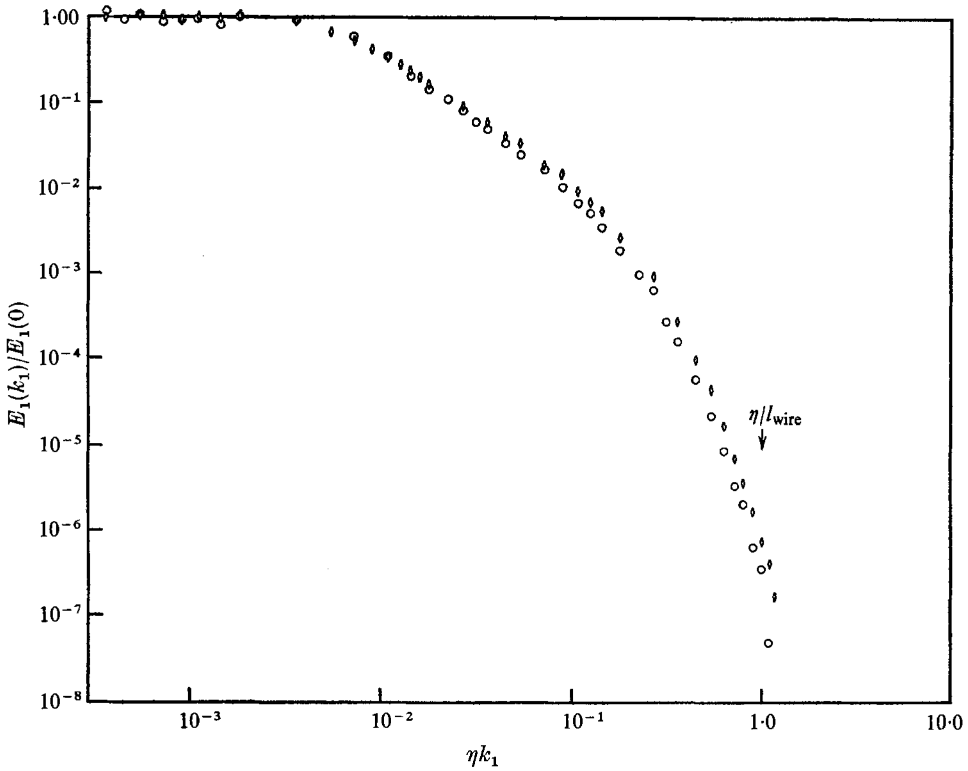

FIGURE 19. One-dimensional energy spectra at two downstream positions. $x_2/h = 0{\cdot}50$. ○, $x_1/h = 10{\cdot}50$; ◊, $x_1/h = 8{\cdot}50$.

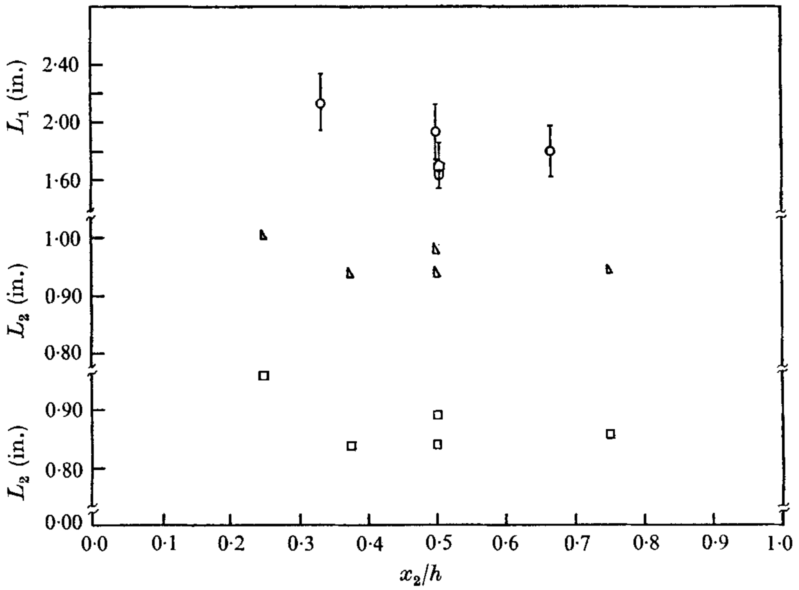

FIGURE 20. Lateral profiles of integral scales. Uncertainty estimates are indicated on one set of points. ○, L_{11}, $x_1/h = 10{\cdot}5$, spectra; ◊, L_{11}, $x_1/h = 8{\cdot}5$, spectra; ▽, L_1, $x_1/h = 8{\cdot}5$, $R_{11}(r_2)$; △, L_2, $x_1/h = 10{\cdot}5$, $R_{11}(r_2)$; □, L_2, $x_1/h = 9{\cdot}5$, $R_{11}(r_2)$.

A.c. circuit coupling must give an output for which $F_1(0) = 0$; this is the same as the integral of the auto-correlation. However, we measured the turbulence spectra without the low-frequency cut-off (figure 5) which was employed in the correlation circuits. Since the hot-wire set is d.c. coupled, it was possible to measure the turbulence spectrum down to rather 'small frequencies' (about 4 Hz), then extrapolate to zero frequency to infer L_{11}.

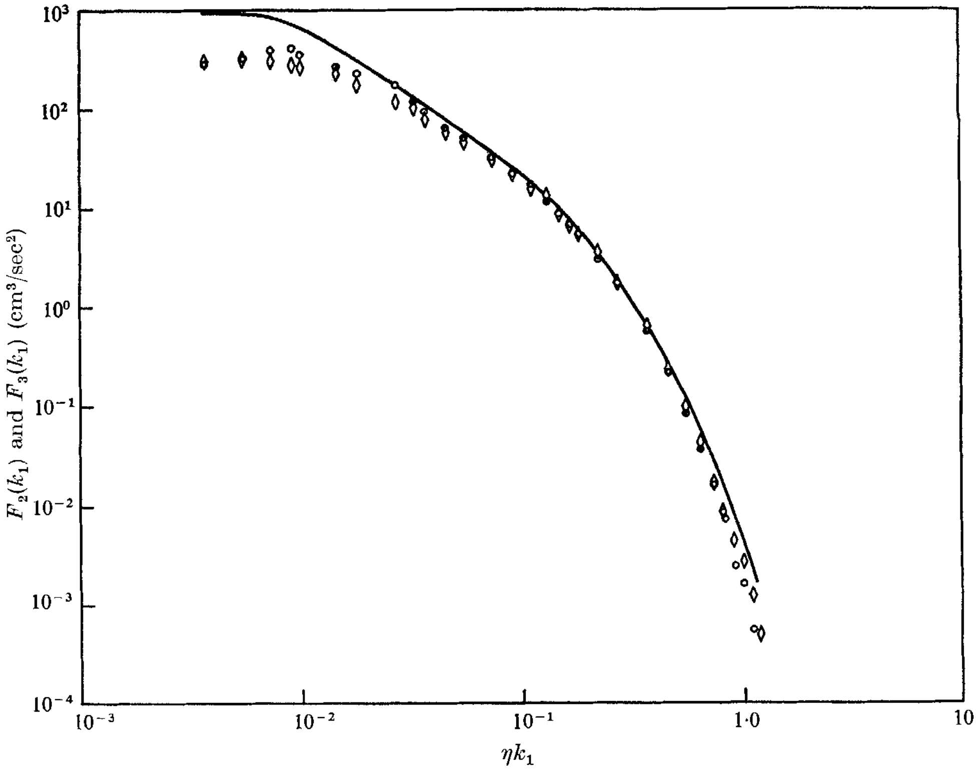

FIGURE 21. Comparison between u_2 and u_3 one-dimensional k_1 spectra, which should be equal for isotropy; comparison with corresponding spectrum computed from measured u_1 spectrum, using isotropic transformation. $x_1/h = 10·5$, $x_2/h = 0·50$, $x_3/h = 0·0$. ◊, $F_2(k_1)$, u_2 spectrum; ○, $F_3(k)$, u_3 spectrum; ——, calculated.

It must be emphasized that even with d.c. coupling one doesn't measure down literally to zero frequency because the sampling time is not infinite. Furthermore, the experiment is not infinite in size; frequencies corresponding to the passage of eddies larger than the homogeneous region are of no interest. This latter point suggests how we decide that 4 Hz is indeed a 'small frequency'. From the Taylor approximation (which may not be very accurate at such low frequencies) we infer that 4 Hz corresponds to a half-wavelength of 5 ft., half the length of the test section—and several times its width.

Figure 17 shows monotonic growth of the integral scales along the test section centreline. L_2 and L_3 were integrated from correlations as indicated following equation (4.6). We note that L_1 is nearly equal to L_{11}.

Figure 20 shows a small departure from integral scale homogeneity as a function of position along x_2, the velocity gradient direction. The departure is roughly the same as for the λ's. The scatter in L_{11} from repeated measurements is indicated by vertical lines and is fairly large.

The lateral scale L_2 is nearly constant across the flow, excluding $x_2/h = 0{\cdot}25$, where the wall boundary-layer influence begins. The dual values of L_2 at $x_2/h = 0{\cdot}50$ were obtained by traversing with $r_2 > 0$ and $r_2 < 0$. The larger value in each case corresponds to $R_{11}(0, r_2, 0; 0)$ with $r_2 > 0$. Numerically L_2 is about one-sixth of the width of the lateral zone which is free of boundary-layer influence.

Figure 21 is a logarithmic plot of the data points for the $\overline{u_2^2}$ and $\overline{u_3^2}$ spectra, $F_2(k_1)$ and $F_3(k_1)$. They are nearly identical for $\eta k_1 > 5{\cdot}0 \times 10^{-2}$, consistent with local isotropy. Also shown on this figure is a curve computed from the measured $\overline{u_1^2}$ spectrum using the isotropic relation

$$F_2(k_1) = F_3(k_1) = \tfrac{1}{2}[F_1(k_1) - k_1(\partial F_1/\partial k_1)]. \tag{4.7}$$

This curve is substantially high at small wave-numbers (where there is strong anisotropy) becaue $F_1(k_1)$ is relatively high there compared with isotropic turbulence, and the first term in the square bracket is dominant. $F_1(k_1)$ is relatively higher at small k_1 in this shear flow because the entire production of turbulent energy is fed into $F_1(k_1)$ in this spectral region (Corrsin 1957).

Beyond $\eta k_1 = 4 \times 10^{-2}$ there is a range of negligible difference, up to perhaps $\eta k_1 = 0{\cdot}5$, consistent with isotropy. The difference which appears at larger ηk_1 is most likely a result of the poorer spatial resolution of the X-probe (used to measure F_2 and F_3) compared with the (smaller) single wire used for F_1. No length correction has been applied, although recent calculations by Wyngaard (1968) will make the computing of this correction easier.

4.5. *Shear correlation spectrum*

A one-dimensional shear correlation coefficient spectrum (see, for example, Corrsin 1949) can be defined as the correlation coefficient between a narrow frequency band of u_1 fluctuation and the same narrow band of u_2 fluctuation at the same point in the flow field:

$${}_nR_{12} \equiv \frac{\overline{{}_nu_1\,{}_nu_2}}{{}_nu_1'\,{}_nu_2'}, \tag{4.8}$$

where the subscript n indicates a narrow frequency band about a nominal centre frequency n Hz. The numerator is a function sometimes called the 'cross spectrum'. With the Taylor approximation, $k_1 \doteq 2\pi n/\overline{U}$, the denominator is simply the product of the square roots of the two one-dimensional energy spectra. In terms of wave-number the correspondence is

$${}_nR_{12} \leftrightarrow {}_{k_1}R_{12} \equiv \frac{F_{12}(k_1)}{\sqrt{[F_1(k_1)\,F_2(k_1)]}}. \tag{4.9}$$

The monotonic decrease to zero of ${}_{k_1}R_{12}$ with increasing k_1 would be consistent with a tendency toward 'local isotropy' (Corrsin 1957) in the sense of Kolmogorov (1941).

The shear coefficient spectrum measured at $x_1/h = 10{\cdot}5$ is shown in figure 22. The accuracy at large wave-number is less than that of the one-dimensional spectrum $F_1(k_1)$ because ${}_nR_{12}$ required taking small differences between relatively large signals. Each point at $\eta k_1 > 0{\cdot}05$ is the average of two measurements.

We note at once that (i) the value of the shear coefficient spectrum is appreciable over much of the wave-number region where the component spectra exhibit consistency with local isotropy (figure 21), and that (ii) there seems to be a region of reversed sign at large wave-numbers. The correlation coefficient values in this large wave-number range are very small and therefore of limited accuracy, but the sign reversal is larger than the scatter in the data. Lacking (for the moment, at least) a fluid-dynamic rationalization for this sign reversal, we might blame it on a systematic instrument error. Since correlation is a measure of phase angle, small differences between the phase shifts of the two channels could be the cause. A more likely cause is hot-wire spatial resolution difficulties, requiring a 'length correction'. The sensing wire lengths of the X-array were 0·4 mm, about equal to the Kolmogorov microscale. The gap was about 0·3 mm.

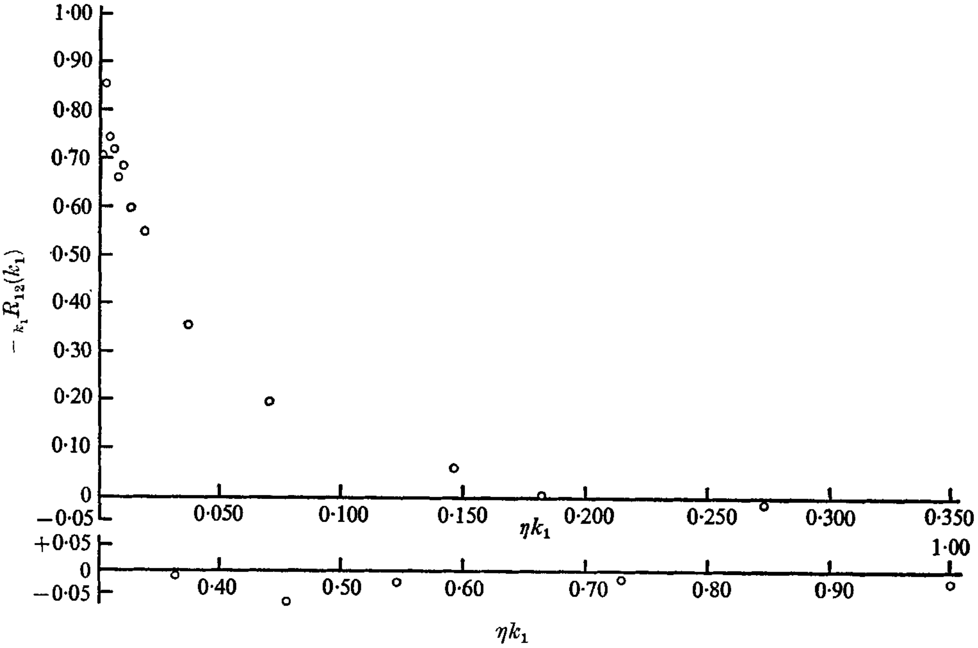

FIGURE 22. Shear stress 'correlation coefficient spectrum', i.e. the cross-spectrum of u_1 and u_2, 'normalized' at each k_1 by the square roots of the energy spectra.

A check on this spectrum was obtained by computing the Reynolds shear stress $-\overline{u_1u_2}$ from it,

$$-\overline{u_1u_2} = \int_0^\infty F_{12}(k_1)\,dk_1. \tag{4.10}$$

Since there is only negligible contribution to the integral at frequencies lower than the lowest experimental value of 5 Hz, no attempt was made to extrapolate the zero frequency. The zero-intercept could be obtained in principle from

$$\lim_{k_1\to 0}\{F_{12}(k_1)\} = -\frac{1}{2\pi}\int_0^\infty \overline{u_1(x_1,t)\,u_2(x_1+r_1,t)}\,dr_1.$$

The average value of $-\overline{u_1 u_2}$ obtained with different probes and on different occasions was $(1{\cdot}84 \pm 0{\cdot}05) \times 10^2\,\mathrm{cm^2/sec^2}$, and the integral of the shear stress spectrum curve gives $1{\cdot}92 \times 10^2\,\mathrm{cm^2/sec^2}$, which is a satisfactory check. The $\pm\,0{\cdot}05$ is full departure range. The integration was done with the assumption that $F_{12} = 0$ for $\eta k_1 \geqslant 0{\cdot}25$, since we tentatively guess that the reversed sign at larger ηk_1 may be due to instrument error.

4.6. *Spatial iso-correlation curves*

Convenient indication of spatial structure is given by the shapes of velocity iso-correlation contours. Measurements of $R_{11}(r_1, r_2, 0; 0)$ and $R_{11}(0, r_2, r_3; 0)$ permit us to draw iso-correlation contours in the (r_1, r_2) and (r_2, r_3) planes. These can then be contrasted with the shapes appropriate to isotropic turbulence, thus identifying effects of constant mean shear on spatial structure. Most of the measurements reported here were done with positive values of r_1, r_2 and r_3 because of the particular probe-traversing gear used.† A limited number of measurements of the type $R_{11}(\pm r_1, r_2, 0; 0)$ and $R_{11}(r_1, \pm r_2, 0; 0)$ were taken specially to examine possible departures from symmetry.

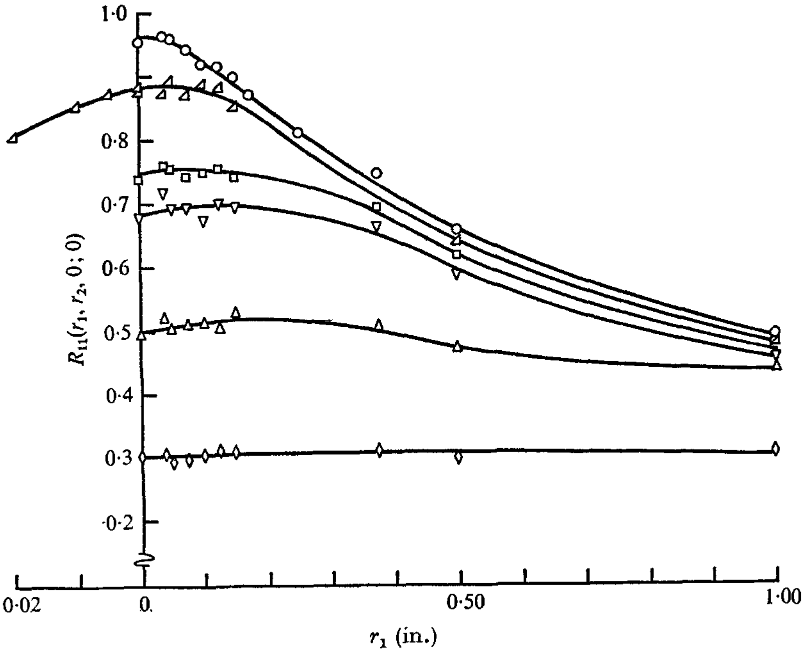

FIGURE 23. Streamwise spatial correlation functions for a series of probe separations along the velocity gradient direction. The unsymmetry is clear. $x_1/h = 8{\cdot}5$, $x_2/h = 0{\cdot}5$, $x_3/h = 0$. ○, $r_2 = 0{\cdot}05$ in.; ◬, $r_2 = 0{\cdot}10$ in.; □, $r_2 = 0{\cdot}20$ in.; ▽, $r_2 = 0{\cdot}25$ in.; △, $r_2 = 0{\cdot}50$ in.; ◇, $r_2 = 1{\cdot}00$ in.

Figure 23 shows some $R_{11}(r_1, r_2, 0; 0)$ data obtained with the fixed hot-wire on the test section centreline at $x_1/h = 8{\cdot}50$. $r_1 > 0$ means that the movable wire

---

† The convention is $\mathbf{r} \equiv \mathbf{x}_{\text{movable probe}} - \mathbf{x}_{\text{fixed probe}}$.

was downstream. For all values of $r_2 > 0$ (movable probe on the high-velocity side—and outside the upstream probe wake), the largest R_{11} occurs for $r_1 > 0$. In isotropic turbulence the largest R_{11} occurs for $r_1 = 0$.

The extended ($r_1 \gtrless 0$) traverse for $r_2 = 0{\cdot}100$ in. displays the phenomenon in more detail. A limited number of measurements at $x_1/h = 10{\cdot}4$ showed the same order of unsymmetry. This kind of unsymmetry was reported in turbulent boundary layers by Tritton (1967).

A lateral symmetry check with $R_{11}(r_1, \pm r_2, 0; 0)$ at $r_1 = 0{\cdot}100$ in. (figure 24(*a*); data points outside the upstream wire wake) show this to be an even function of r_2, at least for small r_2. Figure 24(*b*) indicates that $R_{11}(0, \pm r_2, r_3; 0)$ is also even in r_2.

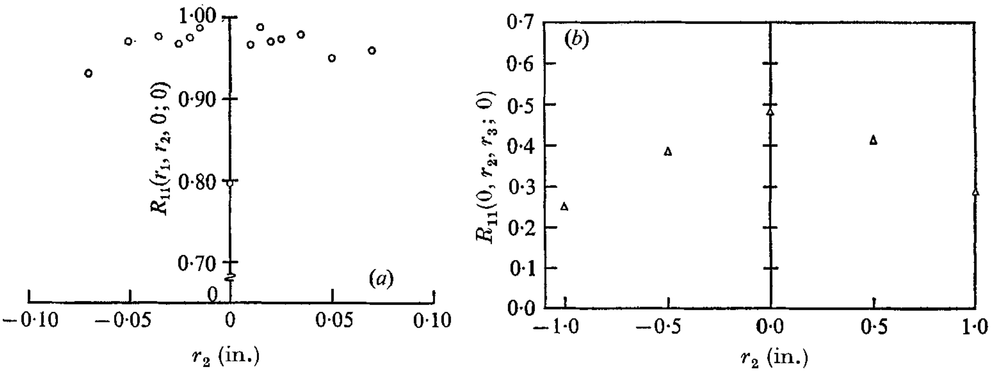

FIGURE 24(*a*)

FIGURE 24(*b*)

FIGURE 24(*a*). Gradient direction ($\pm r_2$) spatial correlation function for a single (small) streamwise (r_1) separation. This is symmetric within the accuracy of the data for these small values of r_2. $r_1 = 0{\cdot}10$ in.

FIGURE 24(*b*). Gradient direction ($\pm r_2$) spatial correlation function for a moderate separation normal to both gradient and mean flow (r_3). Unsymmetry is detectable at large r_2. $R_{11}(0, r_2, r_3; 0)$, $r_3 = 0{\cdot}5$ in.

Spatial iso-correlation contours in the (r_1, r_2) plane are shown in figures 25(*a*), (*b*), (*c*). The data points for $r_2 = 0$ were found by extrapolation of data over a range of r_2 outside the wake (appendix). The curves were faired with the results of the symmetry tests in mind. For example, they were drawn to intersect the r_1 axis orthogonally because of the symmetry of $R_{11}(r_1, r_2, 0; 0)$ in r_2 at small r_2. The fairing here, as elsewhere in this paper, was also influenced by the requirement that the collection of curves be a 'family'.

Figures 26(*a*), (*b*) show the spatial iso-correlation curves in the (r_2, r_3) plane at $x_1/h = 8{\cdot}5$. Evidently the small r_2 symmetry (up and down the $\overline{U}$ gradient) is lost at larger r_2. The unsymmetry for $R_{11} = 0{\cdot}3$, for example, seems greater than might be due to the (inevitable) small departures from homogeneity in the field.

4.7. *Space-time correlations*

Since turbulent velocity fields depend strongly on time as well as position, general double correlations are functions of both time and space separations.

These functions include the particularly important data corresponding to correlation functions *in an Eulerian frame translating with the mean flow*. Statistical properties showing temporal dependence in such a frame are generally interesting. But they are of especially simple importance in a steady, rectilinear mean flow,

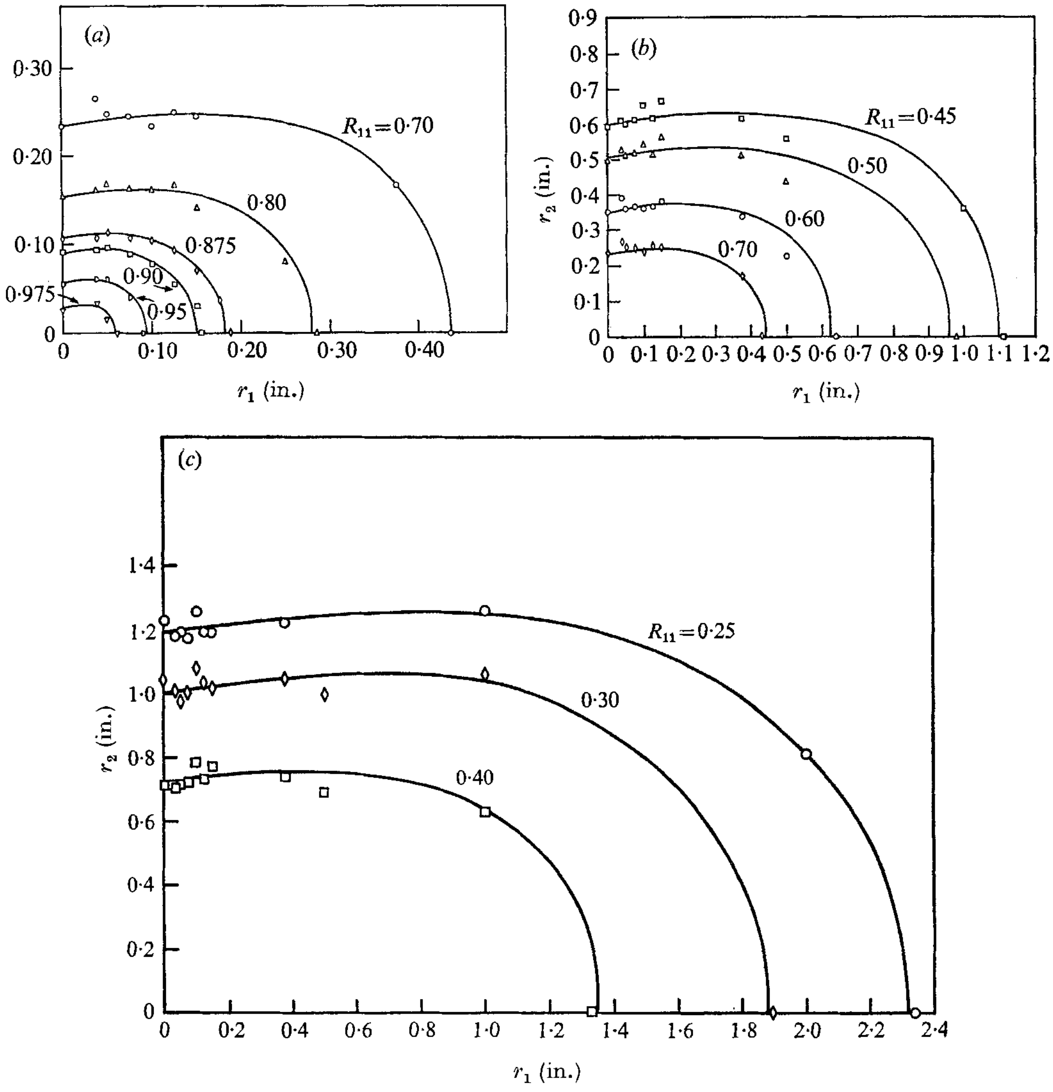

FIGURE 25. Spatial iso-correlation contours $[R_{11}(r_1, r_2, 0; 0)]$ in the (r_1, r_2) plane. The non-zero slopes at $r_1 = 0$ indicate unsymmetry in r_1.

which has constant mean speed along a mean streamline;† in this class of flows the co-ordinate transformation is Galilean, so the frame moving with the mean speed is inertial over a finite (i.e. non-zero) time interval.

---

† At these low turbulence levels it is not important to distinguish between the direction of the mean flow [i.e. $\tan^{-1}(\overline{U}_2/\overline{U}_1)$] and the mean of the flow direction $[\overline{\tan^{-1}(U_2/U_1)}]$.

Another interesting function contained in the complete space-time correlation is, for each space separation, *the time difference corresponding to maximum correlation*. This will be referred to as the '*optimum time delay*'. A complementary function is, for each time difference, *the spatial separation corresponding to maximum correlation*. With the equipment available to us, the former was simpler to measure, and is presented below. The Sangamo tape recorder (with G.P.S. multipler) was used to obtain much of the data, and a P.A.R. correlator became available near the end of this study. Tested with the same signals, the two systems gave nearly identical results.

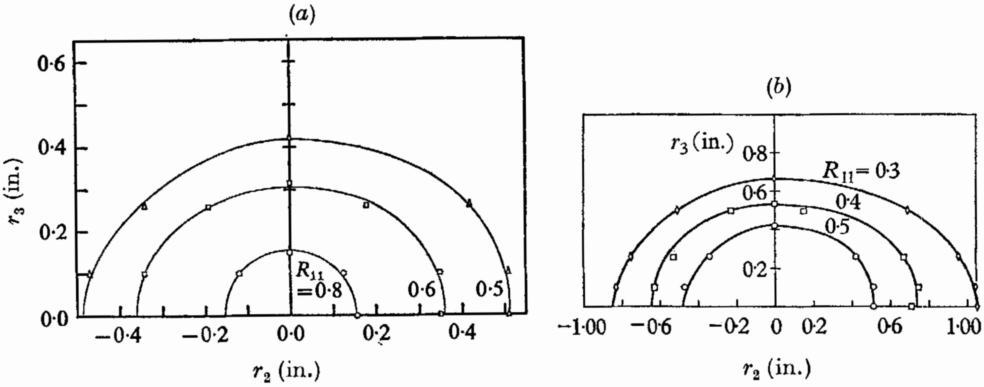

FIGURE 26. Spatial iso-correlation contours $[R_{11}(0, r_2, r_3; 0)]$ in the (r_2, r_3) plane. They appear symmetric in r_2 for small r_2, unsymmetric for large r_2.

All of the space-time correlations measured were for the u_1 field. Measurements with lateral separation along the velocity gradient, $R_{11}(0, r_2, 0; \tau)$, are shown in figure 27. The spatial location nominally assigned to a space-time correlation function is the location of the *fixed* probe, located on the test section centreline. Unless identified otherwise, all data were taken with the fixed probe at $x_1/h = 8 \cdot 50$.

Figure 27 shows distinct unsymmetry in τ, increasing with increasing r_2. The sign convention on τ is given by its definition,

$$\tau \equiv t_{\text{movable probe signal}} - t_{\text{fixed probe signal}}.$$

With the two probe signals recorded simultaneously, τ is the *delay* applied to the fixed probe signal during the tape 'playback' for correlation measurement.

We use τ_M to designate the 'optimum time delay', the value of τ corresponding to a peak in $|R_{11}|$. In figure 27, with the movable probe in the higher-velocity stratum ($r_2 > 0$), $\tau_M < 0$. This means that the maximum correlation occurs when the signal from the fixed probe (at the lower velocity position) is played back at a larger value of time. This seems plausible because this late-arriving fluid convected at lower speed was actually closer to the faster-moving fluid when both were a bit upstream, and the turbulence structure certainly has a 'memory'.

We note also that $|\tau_M|$ increases with increasing r_2. For $r_2 = 1 \cdot 00$ in., $\tau_M \approx -0 \cdot 8$ msec, so the fluid particles having maximum correlation were about 0·4 in. apart in x_1. With a mean speed difference of 0·8 ft./sec, they were at roughly equal values of x_1 about 0·04 sec 'earlier' (i.e. about 1·6 ft. upstream of the observation plane). For comparison we note that the inverse of the mean strain rate is

$$(\partial \overline{U}/\partial x_2)^{-1} = 0{\cdot}08\,\text{sec}.$$

Measurements of $R_{11}(0, r_2, 0; \tau)$ made at $x_1/h = 10{\cdot}4$ (data not shown) yielded $\tau_M(r_2)$ equal to the values at 8·5. The values of $R_{11}(0, r_2, 0; \tau_M)$ were slightly larger, consistent with the general scale growth downstream.

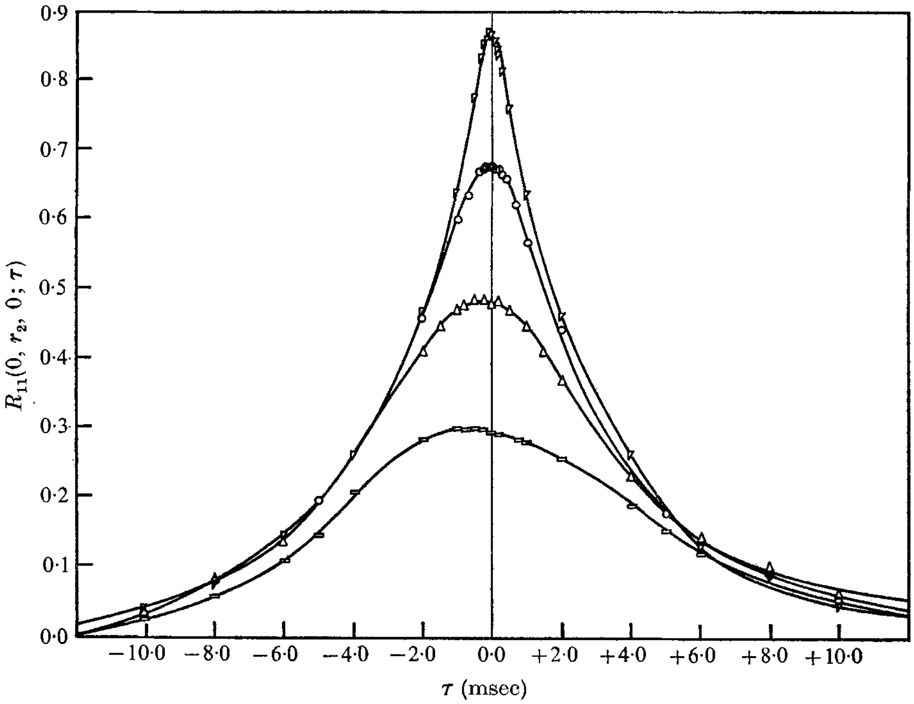

FIGURE 27. Space-time correlation functions $[R_{11}(0, r_2, 0; \tau)]$ *vs.* time difference τ for a series of gradient direction separations (r_2) and zero streamwise separation (r_1) and zero r_3. ▽, $r_2 = 0{\cdot}10$ in.; ○, $r_2 = 0{\cdot}25$ in.; △, $r_2 = 0{\cdot}50$ in.; ▭, $r_2 = 1{\cdot}00$ in.

Space-time correlations with probe separation normal to both mean flow and mean velocity gradient, $R_{11}(0, 0, r_3; \tau)$, figure 28, are symmetric in τ. The fully negative cases, $r_3 = 1{\cdot}5$, 2·0 and 3·0 in., are in a range of r_3 in which $R_{11}(0, 0, r_3; 0)$ has a rather large negative value (figure 15). We note that $R_{11}(0, 0, r_3; \tau)$ *vs.* τ changes shape as r_3 is increased. In fact, a local minimum develops at $\tau = 0$. A similar minimum was observed in turbulent pipe flow by Bakewell (1966).

Figure 29 shows space-time correlations with longitudinal probe separation only, $R_{11}(r_1, 0, 0; \tau)$. The shifted peak in this now familiar kind of data (pioneered by Favre, Gaviglio & Dumas 1953) is due to the convecting action of the mean flow. We can define a 'correlation convection speed' $V_R \equiv r_1/\tau_M(r_1, 0, 0)$. For this simple flow $V_R = U_c$, but the effect is more complex in flows with curved velocity profiles. Of course, for $r_2 \neq 0$, $V_R \neq U_c$ even in the present flow.

The dashed curve is the auto-correlation curve of the fixed (upstream) probe signal. The envelope of the curves represents the (time) auto-correlation in a

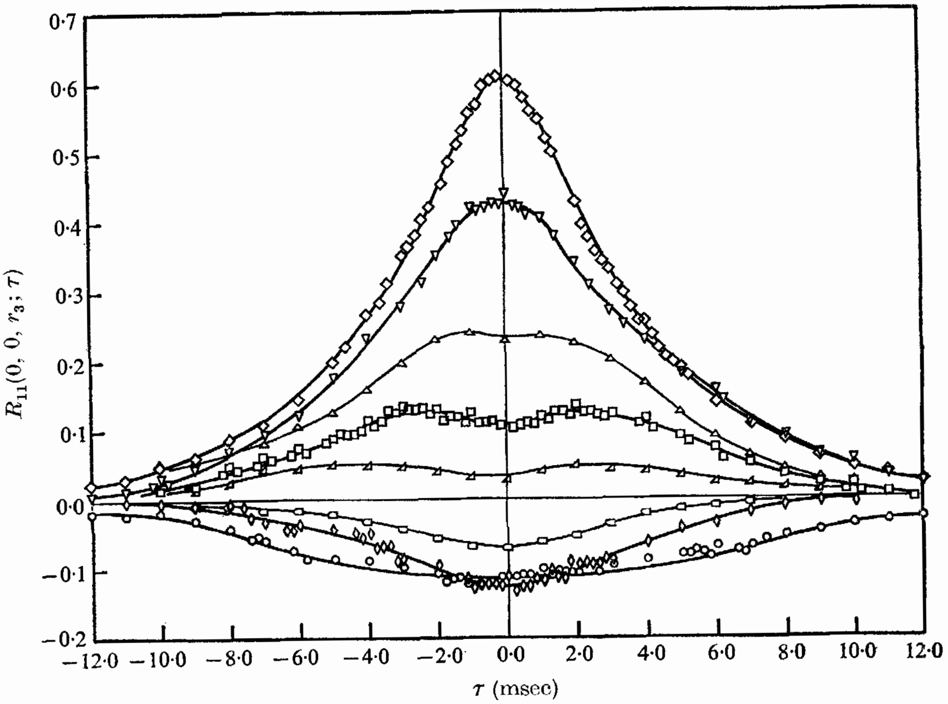

FIGURE 28. Space-time correlation functions [$R_{11}(0, 0, r_3; \tau)$] *vs.* τ for a series of r_3 separations, and $r_1 = r_2 = 0$. ◇, $r_3 = 0{\cdot}295$ in.; ▽, $r_3 = 0{\cdot}50$ in.; △, $r_3 = 0{\cdot}75$ in.; □, $r_3 = 1{\cdot}00$ in.; ◿, $r_3 = 1{\cdot}25$ in.; ▭, $r_3 = 1{\cdot}50$ in.; ◊, $r_3 = 2{\cdot}00$ in.; ○, $r_3 = 3{\cdot}00$ in.

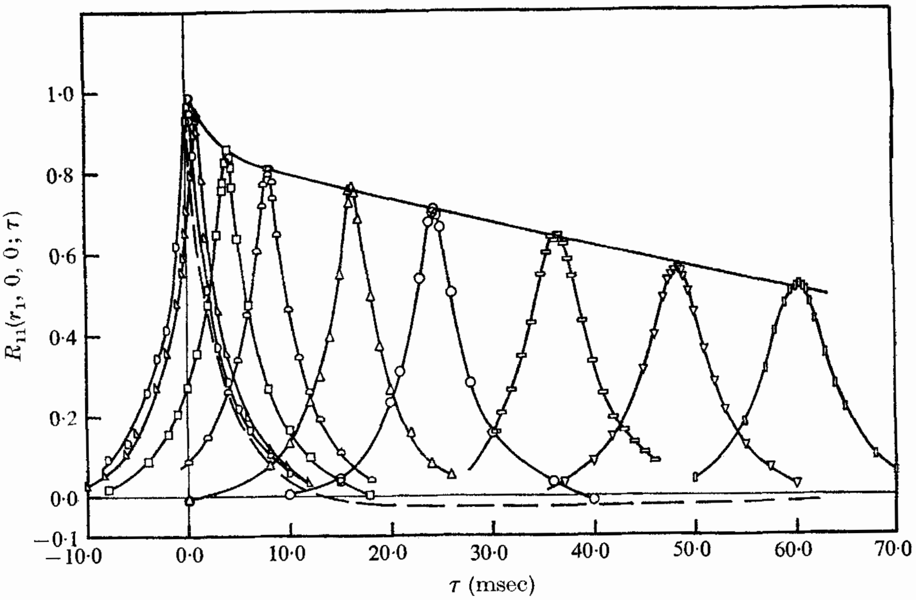

FIGURE 29. Space-time correlation functions [$R_{11}(r_1, 0, 0; \tau)$] *vs.* τ for a series of r_1 separations, and $r_2 = r_3 = 0$. The envelope is auto-correlation function in a convected frame travelling with the mean speed in this x_2 layer. D, $r_1 = 0{\cdot}10$ in.; ◺, $r_1 = 0{\cdot}50$ in.; □, $r_1 = 2{\cdot}00$ in.; ⌓, $r_1 = 4{\cdot}00$ in.; △, $r_1 = 8{\cdot}00$ in.; ○, $r_1 = 12{\cdot}00$ in.; ▭, $r_1 = 18{\cdot}00$ in.; ▽, $r_1 = 24{\cdot}00$ in.; ▯, $r_1 = 30{\cdot}00$ in.; — — —, auto-correlation.

frame moving with the convection velocity. This is the simplest sort of time correlation in the turbulence, but it could not be pursued all the way to the time at which $|R_{11}| \ll 1$ because the wind tunnel exit was reached at $r_1 = 30$ in.

Space-time correlations with r_1 and $r_2 \geqslant 0$ are shown in figures 30–34. r_1 is fixed for each figure and each set of points was measured at fixed r_2. The short vertical line drawn under each set of points, in most cases a bit to the right of the peak, is the τ value equal to the average convection time for the slab of fluid bounded by $x_2 = 0{\cdot}5h$ and $x_2 = 0{\cdot}5h + r_2$:

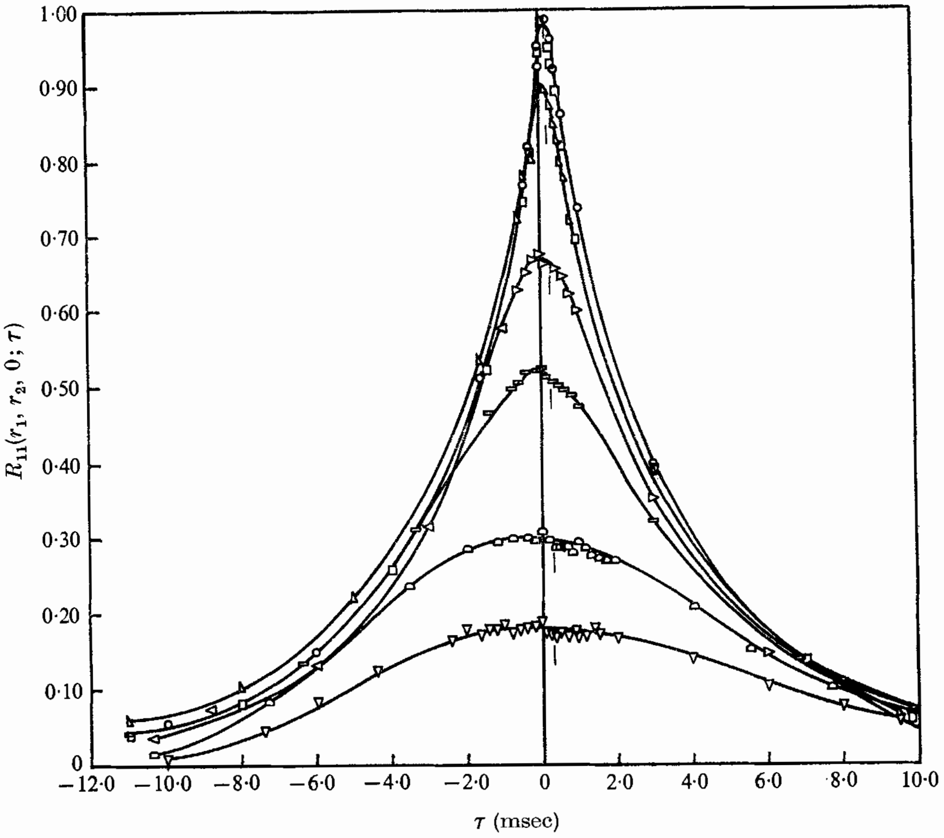

FIGURE 30. Space-time correlation functions $[R_{11}(r_1, r_2, 0; \tau)]$ *vs.* τ for a series of r_2 separations and $r_1 = 0{\cdot}10$ in. Short vertical lines are at $\tilde{\tau}$. ○, $r_2 = 0{\cdot}02$ in.; □, $r_2 = 0{\cdot}05$ in.; ◺, $r_2 = 0{\cdot}10$ in.; ▷, $r_2 = 0{\cdot}25$ in.; ▭, $r_2 = 0{\cdot}50$ in.; ⌓, $r_2 = 1{\cdot}00$ in.; ▽, $r_2 = 1{\cdot}50$ in.

$$\tilde{\tau} \equiv r_1/\tilde{U}(r_2), \quad \text{where} \quad \tilde{U} \equiv U_c + \frac{d\bar{U}_1}{dx_2}\frac{r_2}{2}. \tag{4.11}$$

The difference between $\tilde{\tau}$ and τ_M is essentially independent of r_1. Comparing these figures with figure 27, the $r_1 = 0$ case, we find that

$$\tau_M(r_1, r_2, 0) = \tau_M(0, r_2, 0) + r_1/\tilde{U}, \tag{4.12}$$

which is similar to boundary-layer results of Favre *et al.* (1955).

A typical case with appreciable wake interference effect is shown in the appendix, for $r_1 = 0\cdot5$ in. For $r_1 \geqslant 4\cdot0$ in., the upstream probe wake could no longer be detected. Without wake effect the maximum correlations with optimum delay occurred at $r_2 = 0$.

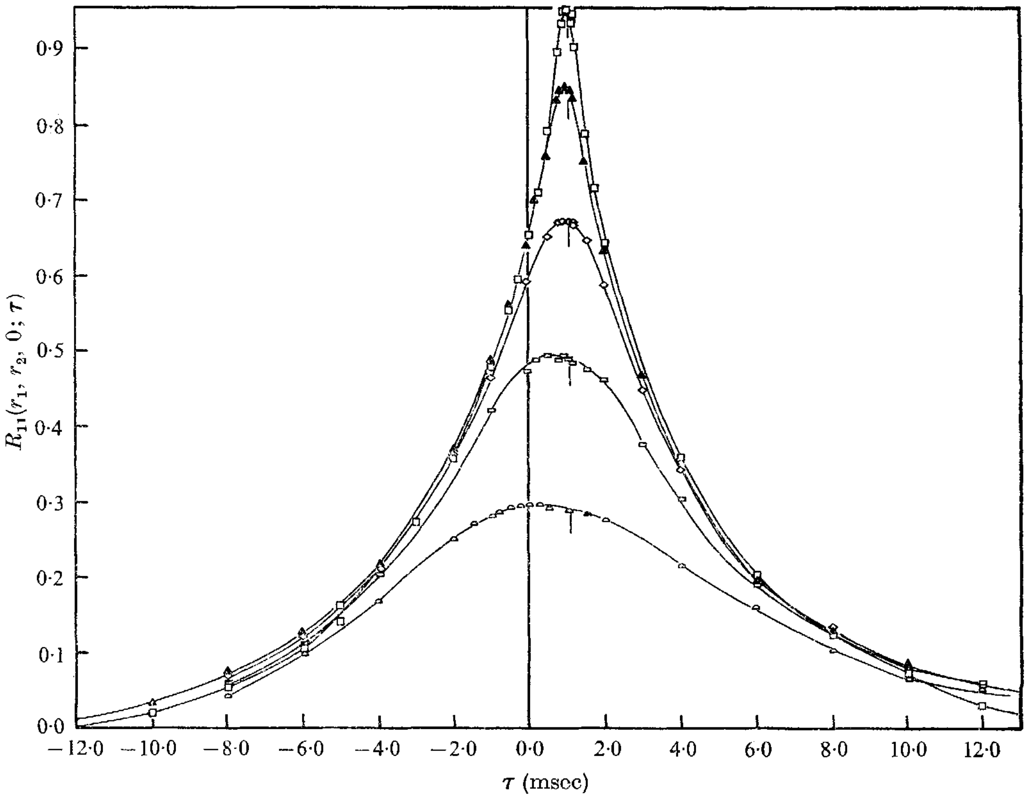

FIGURE 31. Space-time correlation functions $[R_{11}(r_1, r_2, 0; \tau)]$ *vs.* τ for a series of r_2 separations and $r_1 = 0\cdot50$ in. Short vertical lines are at $\tilde{\tau}$. □, $r_2 = 0\cdot035$ in.; ▲, $r_2 = 0\cdot10$ in.; ◇, $r_2 = 0\cdot25$ in.; ▭, $r_2 = 0\cdot50$ in.; △, $r_2 = 1\cdot00$ in.

We conclude that, at any r_1, $[R_{11}(\tau_M)]_{\max}$ occurs at $r_2 = 0$ and that the corresponding $\tau_M(r_1, 0, 0)$ is equal to $r_1/\overline{U}$ in that stratum. For these particular experiments the fixed probe was always at $x_2 = 0\cdot5h$, where $\overline{U} \equiv U_c$, so, for $r_2 = 0$, $\tau_M = r_1/U_c$. We observe furthermore that this 'convection speed' of the R_{11} peak for $r_2 = 0$ is independent of r_1.

A 'correlation convection speed' alternative to V_R can be defined by

$$V'_R \equiv (r_1)_M/\tau,$$

where $(r_1)_M$ is the r_1 corresponding to maximum $|R_{11}(r_1, 0, 0; \tau)|$ at any τ. A few tests in the present flow showed V'_R consistently 2 % smaller than V_R, independent of r_1 or τ. In more general shear flows V_R and V'_R differ more, and are not independent of r_1 and τ respectively. Therefore other concepts of 'correlation convection speed' have been suggested by Wills (1964) and Favre *et al.* (1967). The fact that V_R and V'_R are nearly equal and that V_R is independent of r_1 in this 'homogeneous' case is consistent with the observation that the Taylor approximation is well satisfied.

Space-time correlations with separation in both r_1 and r_3 (normal to mean flow and velocity gradient) are shown in figures 35 and 36. The optimum time delays are virtually identical with those for $r_3 = 0$, and hence are equal to r_1/U_c. Compare, for example, $\tau_M(24, 0, 0{\cdot}5)$ in figure 36 with $\tau_M(24, 0, 0)$ in figure 34. The slight dependence of τ_M on r_3 is apparently due to the slight variation in $\overline{U}$ with x_3 (figure 12).

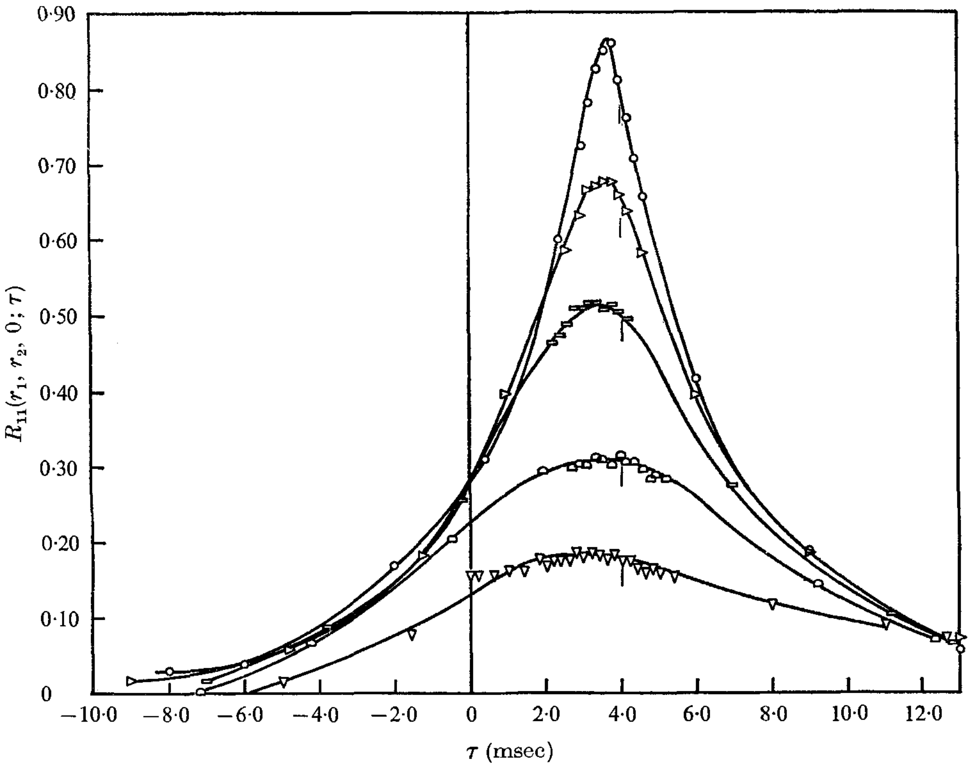

FIGURE 32. Space-time correlation functions $[R_{11}(r_1, r_2, 0; \tau)]$ *vs.* τ for a series of r_2 separations and $r_1 = 2{\cdot}00$ in. Short vertical lines are at $\bar{\tau}$. ○, $r_2 = 0{\cdot}10$ in.; ▷, $r_2 = 0{\cdot}25$ in.; ▭, $r_2 = 0{\cdot}50$ in.; ⌓, $r_2 = 1{\cdot}00$ in.; ▽, $r_2 = 1{\cdot}50$ in.

A generous region with $R_{11} < 0$ occurs for $r_3 = 2{\cdot}00$ in. just as it does in the corresponding spatial correlation $R_{11}(0, 0, r_3; 0)$.

Space-time correlations of the type $R_{11}(0, r_2, r_3; \tau)$ are shown in figure 37. Here we might expect to find $\tau_M(0, r_2, r_3) \doteq \tau_M(0, r_2, 0)$. However, the scatter here precludes a meaningful comparison of peak locations with the $r_2 = 0{\cdot}5$ in. curve of figure 27.

With the movable probe at $r_3 > 0$ it was possible to reach negative values of r_2, which could not be reached when $r_3 = 0$ because of probe support structures. Figure 37 shows that $R_{11}(0, -r_2, r_3; \tau) \neq R_{11}(0, r_2, r_3; \tau)$. This slight unsymmetry is qualitatively consistent with that indicated along the $r_3 = 0$ axis in figure 26 (*b*).

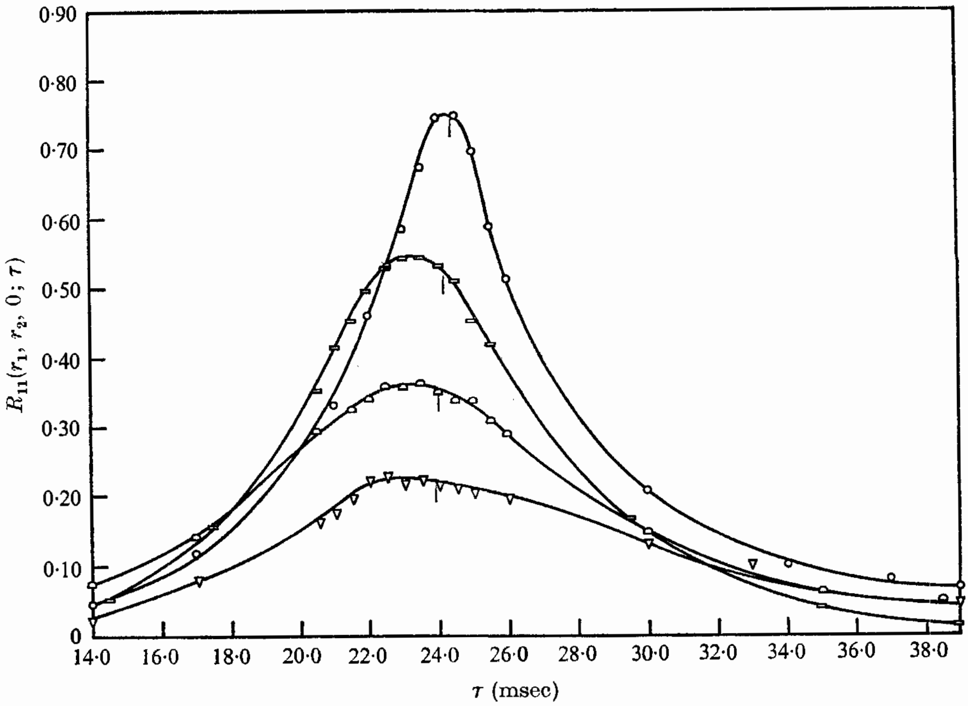

FIGURE 33. Space-time correlation functions $[R_{11}(r_1, r_2, 0; \tau)]$ *vs.* τ for a series of r_2 separations and $r_1 = 12{\cdot}0$ in. Short vertical lines are at $\tilde{\tau}$. ○, $r_2 = 0{\cdot}0$ in.; ▭, $r_2 = 0{\cdot}50$ in.; ⌓, $r_2 = 1{\cdot}00$ in.; ▽, $r_2 = 1{\cdot}50$ in.

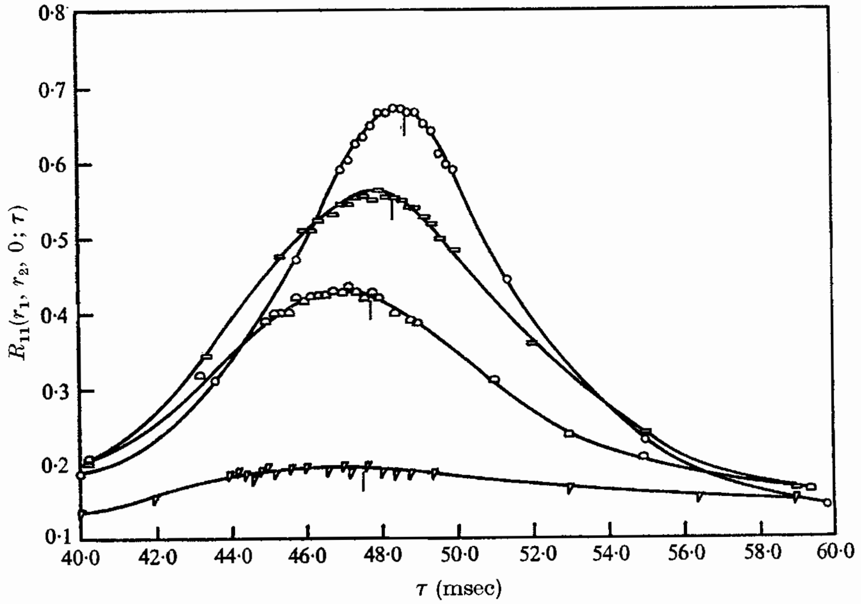

FIGURE 34. Space-time correlation functions $[R_{11}(r_1, r_2, 0;\tau)]$ *vs.* τ for a series of r_2 separations and $r_1 = 24{\cdot}0$ in. Short vertical lines are at $\tilde{\tau}$. ○, $r_2 = 0{\cdot}0$ in.; ▭, $r_2 = 0{\cdot}50$ in.; ⌓, $r_2 = 1{\cdot}00$ in.; ▽, $r_2 = 2{\cdot}00$ in.

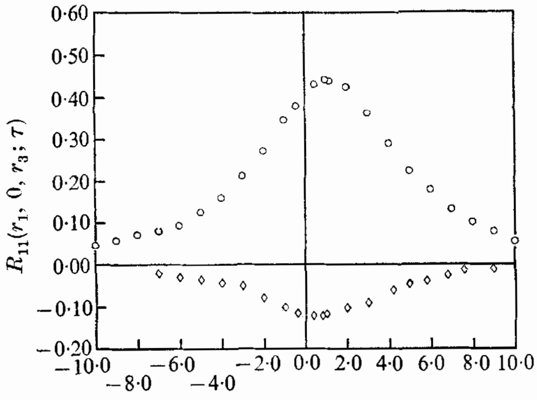

FIGURE 35

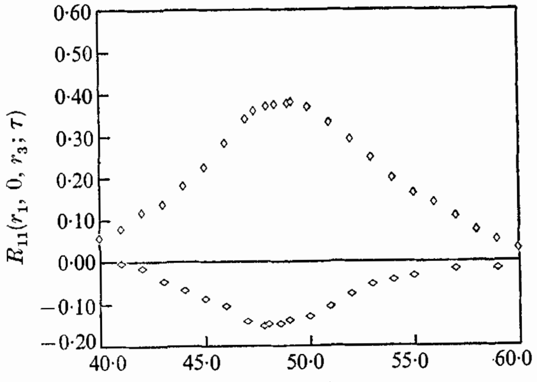

FIGURE 36

FIGURE 35. Space-time correlation functions $[R_{11}(r_1, 0, r_3; \tau)]$ *vs.* τ for two different r_3 values, $r_2 = 0$ and small r_1 ($= 0{\cdot}50$ in.). ○, $r_3 = 0{\cdot}50$ in.; ◇, $r_3 = 2{\cdot}00$ in.

FIGURE 36. Space-time correlation functions $[R_{11}(r_1, 0, r_3; \tau)]$ *vs.* τ for two different r_3 values, $r_2 = 0$ and large r_1 ($= 24{\cdot}0$ in.). ◇, $r_3 = 0{\cdot}50$ in.; ◊, $r_3 = 2{\cdot}00$ in.

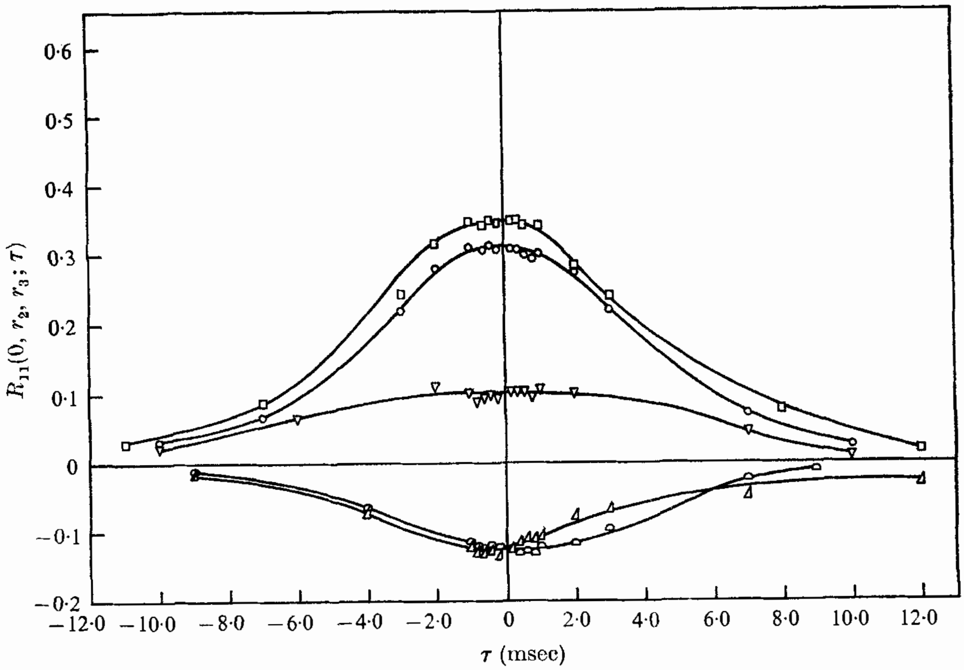

FIGURE 37. Space-time correlation functions $[R_{11}(0, r_2, r_3; \tau)]$ *vs.* τ for a series of r_3 values, with some opposite r_2 values and $r_1 = 0$. The slight unsymmetry in r_2 for $r_3 = 0{\cdot}5$ is consistent at $\tau = 0$ with figure 26(*b*). □, $r_2 = 0{\cdot}5$ in.; $r_3 = 0{\cdot}5$ in.; ○, $r_2 = -0{\cdot}5$ in., $r_3 = 0{\cdot}5$ in.; ▽, $r_2 = 0{\cdot}5$ in., $r_3 = 1{\cdot}0$ in.; △, $r_2 = 0{\cdot}5$ in., $r_3 = 2{\cdot}0$ in.; ⌓, $r_2 = -0{\cdot}5$ in., $r_3 = 2{\cdot}0$ in.

4.8. *Space-time correlation in a convected frame*

The basic Eulerian frame in which to examine the turbulence field evolution is one travelling with the fluid in the mean. Such a concept is simple only for homogeneous fields. In more general turbulent shear flows the curvature of the mean velocity profile destroys the resulting simple antisymmetry of mean convection and distortion effects in layers equidistant 'above' and 'below' any reference lamina.

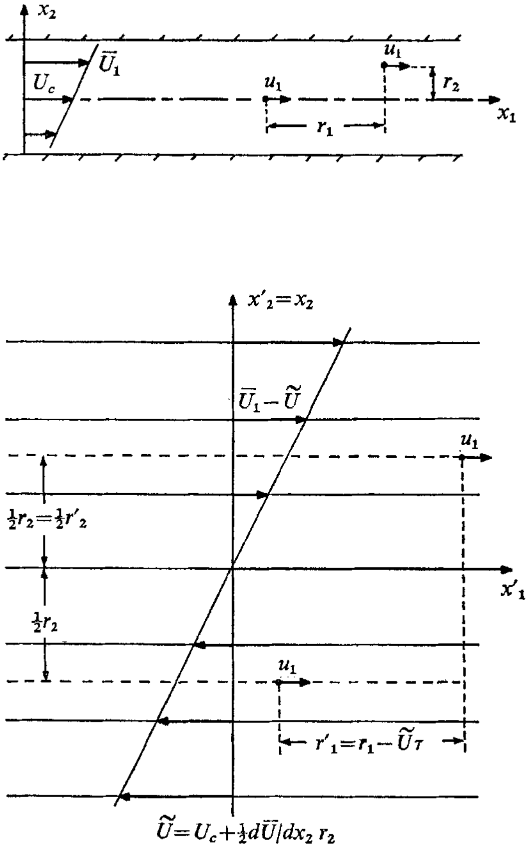

FIGURE 38. The transformation from laboratory co-ordinates (top) to convected co-ordinates travelling with the mean speed of the fluid layer bounded by the x_2 positions of the probes.

In the homogeneous case, for example, the space-time correlation peak with $r_2 = r_3 = 0$ travels simply with the local mean flow, so it is fixed at the origin of a correspondingly convected frame. This is not true in a (necessarily inhomogeneous) case with curved velocity profile (e.g. Favre *et al.* 1955; Baldwin & Mickelsen 1962; Fisher & Davies 1964), so these flows may be more fruitfully studied in frames translating with the space-time correlation maxima, i.e. for optimum delay τ_M (Favre *et al.* 1967).

In flows with strong downstream inhomogeneity, such as a jet entering fluid at rest, both kinds of (accelerating) convected frames may be appreciably non-inertial.

Although our data lend themselves more easily to presentation in terms of τ_M (next sections), we have extracted from the data of the previous section some typical space-time correlations evaluated in a frame travelling at a speed equal to $\tilde{U}$, the average of the speeds in the two laminae of the hot-wire probes (figure 38). Figure 39 shows that these results resemble figure 41, as we expect in view of equation (4.12).

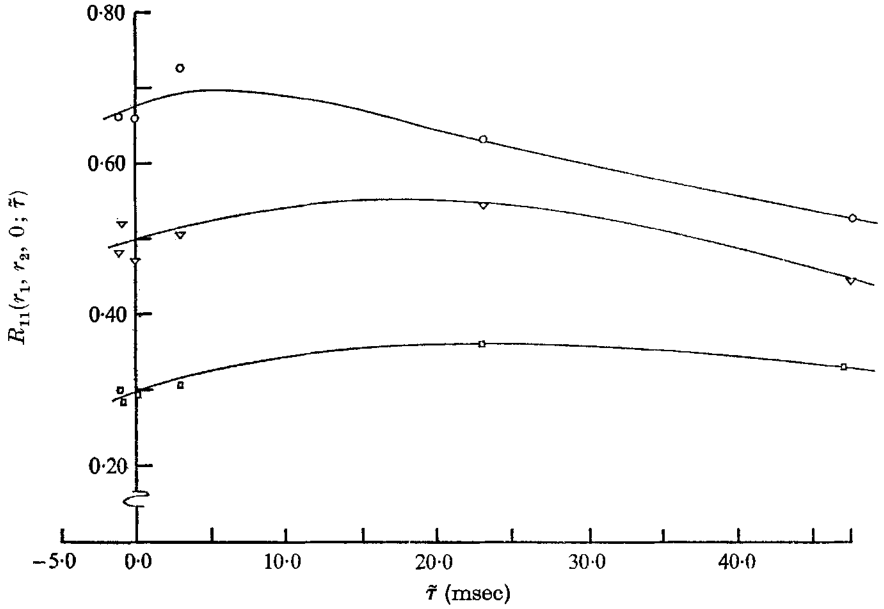

FIGURE 39. Typical space-time correlation functions $[R'_{11}(r'_1, r'_2, 0; \tilde{\tau})]$ in the frame travelling with the 'local' mean speed of the flow (figure 38). $r'_2 = r_2$, $\tilde{\tau}$ is defined in equation (4.11). $r'_1 = 0{\cdot}50$ in. ○, $r'_2 = 0{\cdot}0$ in.; ▽, $r'_2 = 0{\cdot}5$ in.; □, $r'_2 = 1{\cdot}0$ in.

4.9. *Space-time iso-correlation curves with optimum delay*

For each pair of hot-wire probe positions, there is a particular 'optimum time delay' τ_M which gives an extreme value (usually a maximum) of the two-point Eulerian velocity correlation coefficient function. Favre *et al.* (1955) have measured for a boundary layer the shape of the spatial correlation function defined by selecting $\tau = \tau_M$ for each spatial separation, e.g.

$$R_{11}^{(M)}(r_1, r_2, r_3) \equiv R_{11}(r_1, r_2, r_3; \tau_M). \tag{4.13}$$

Figure 40 shows the dependence of $R_{11}^{(M)}(r_1, r_2, 0)$ on r_2 for a small fixed value of r_1 in the present flow. For small r_2 at least, these functions were found to be even in r_2.

Figure 41 gives some of the data measured on $\mathrm{R}_{11}^{(M)}(r_1, r_2, 0)$ to look for possible symmetry in r_1 for fixed r_2. These functions are not even in r_1. It is especially notable that, except for $r_2 = 0$ (the envelope of figure 29), $R_{11}^{(M)}$ has its maximum at $r_1 > 0$. This is qualitatively like the $\tau = 0$ case, figure 23. This behaviour is reflected in the shapes of the iso-correlation contours, $R_{11}^{(M)}$ = constant. In isotropic turbulence the maxima all occur at $r_1 = 0$.

Typical iso-correlation contours in the (r_1, r_2) plane are sketched in figure 42.

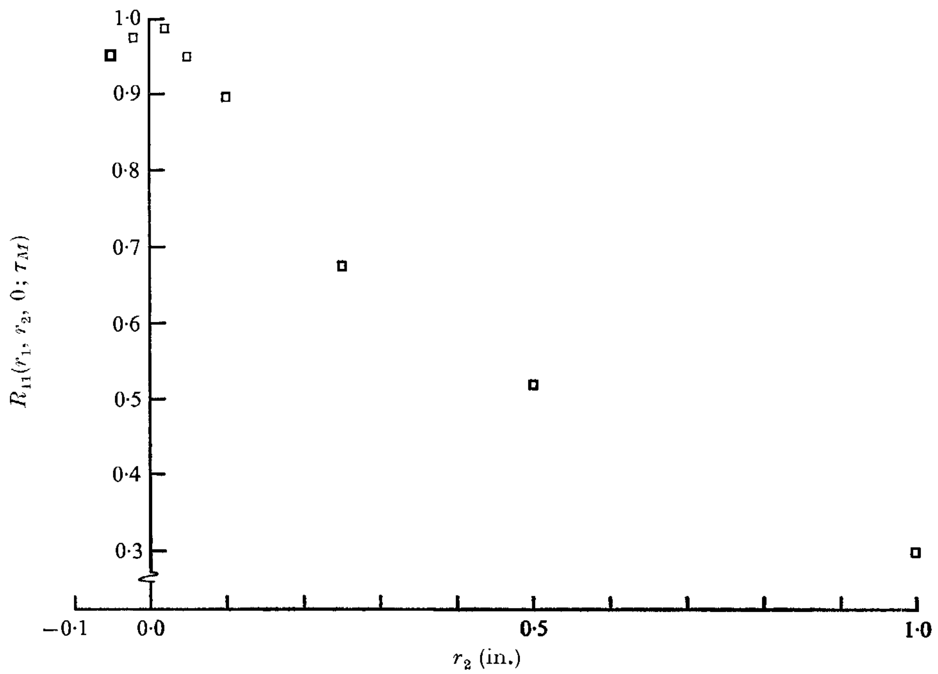

FIGURE 40. Space-time correlation with 'optimum' time delay $\tau_M(r_1, r_2)$, as a function of r_2 at a fixed r_1 = 0·10 in.

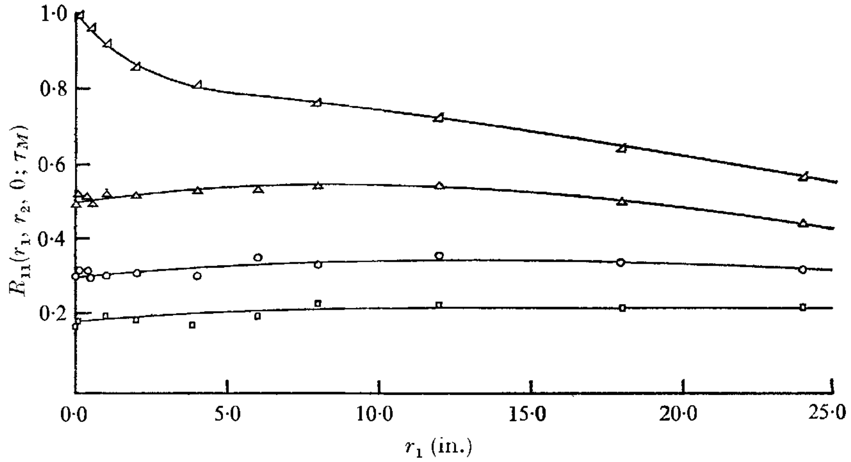

FIGURE 41. Space-time correlation with 'optimum' time delay $\tau_M(r_1, r_2)$ as a function of r_1, at several fixed values of r_2. The top curve is the envelope of figure 29. In this $r_2 = r_3 = 0$ case, τ_M equals the travel time for the convected frame of §4.8. ⊿, r_2 = 0·0 in.; △, r_2 = 0·5 in.; ○, r_2 = 1·0 in.; □, r_2 = 1·5 in.

These resemble their $\tau = 0$ counterparts, figures 25(*a*), (*b*), (*c*), although the r_1 extension is greater here.

Figure 43 shows that $R_{11}^{(M)}(0, r_2, r_3)$ is roughly an even function of r_2. We have insufficient data to permit sketching space-time iso-correlation curves in this case.

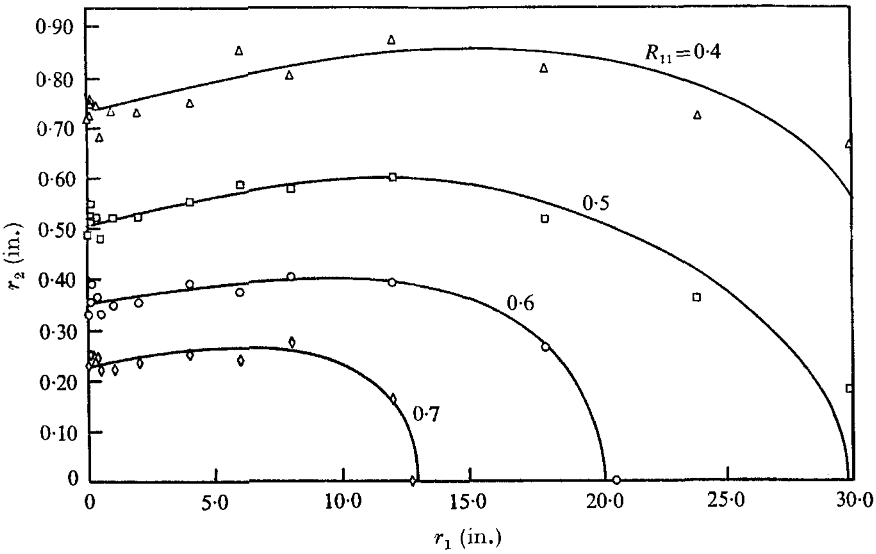

FIGURE 42. Typical space-time iso-correlation contours $[R_{11}(r_1, r_2, 0; \tau_M)]$ for optimum time delay. The non-zero slopes at $r_1 = 0$ indicate unsymmetry in r_1.

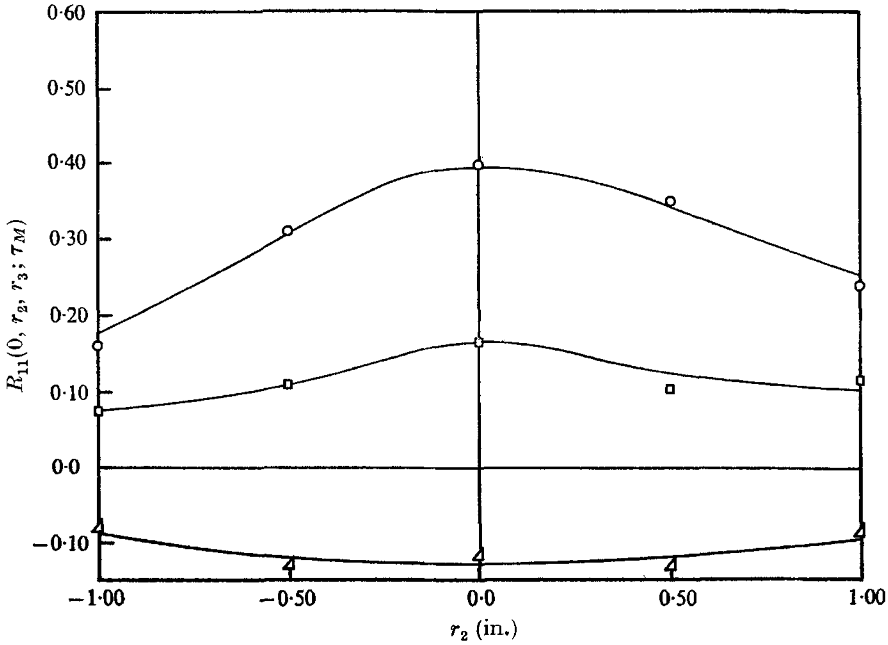

FIGURE 43. Space-time correlation $[R_{11}(0, r_2, r_3; \tau_M)]$ with optimum time delay as a function of r_2 for a set of r_3 values. They are symmetric in r_2 within the accuracy of the data. ○, $r_3 = 0{\cdot}50$ in.; □, $r_3 = 1{\cdot}00$ in.; △, $r_3 = 2{\cdot}00$ in.

5. Analysis of experimental results

5.1. *Homogeneity; stationarity in a moving frame*

In §2.2 we reached a tentative conclusion that (spatially) homogeneous turbulent shear flow at very large Reynolds number may not be stationary (in time). We hope that the downstream part ($8{\cdot}5 \leqslant x_1/h \leqslant 10{\cdot}5$) of our wind tunnel is a viable approximation to homogeneous shear flow. It is of course stationary in the laboratory frame simply because the fan runs steadily, but the time evolution of the turbulence structure is best examined in a frame convected uniformly at a speed equal to the average speed in the fluid slab under study. The spatial inhomogeneity necessarily leads to non-stationarity in any uniformly convected frame, and we shall estimate the departure from stationarity in, say, a frame convected at U_c, the mean centreline speed.

We begin by computing the departures from homogeneity. At the end we shall ask whether the field has reached an asymptotic state—albeit a non-uniform one. Necessary criteria for homogeneity are that the mean flow and turbulence statistical properties vary by only relative small amounts over distances as large as the largest characteristic lengths in the turbulence:

$$(\Lambda/N)|\nabla N| \ll 1, \tag{5.1}$$

where N is a mean property, ∇ is the gradient operator and Λ is ideally the greatest distance over which correlations are measurable. In place of Λ we use integral scales of the velocity field.

The data in figures 7 and 10 and the computations in §4.1 indicate that the mean strain rate $d\bar{U}_1/dx_2$ and the second moments of the turbulent velocity components are relatively free of large-scale trend inhomogeneities, so we focus our attention on the scales λ and L, figures 17, 18 and 20. The following are average trend departures from homogeneity in the working volume, $8{\cdot}5 \leqslant x_1/h \leqslant 10{\cdot}5$:

$$\left.\begin{aligned} \frac{L_1}{\lambda_1}\frac{\partial\lambda_1}{\partial x_1} &= 0{\cdot}015; \quad \frac{\partial L_1}{\partial x_1} = 0{\cdot}010;\\ \frac{L_2}{\lambda_2}\frac{\partial\lambda_2}{\partial x_2} &= -0{\cdot}017; \quad \frac{\partial L_2}{\partial x_2} = -0{\cdot}005. \end{aligned}\right\} \tag{5.2}$$

These magnitudes seem to indicate a good approximation to homogeneity.

A different length characterizing the large structure in a shear flow is a measure of the shear stress eddy size, such as the inverse of the first moment of the shear spectrum (Corrsin 1957),

$$(k_1)_{12}^{-1} \equiv \int_0^\infty F_{12}\,dk_1 \bigg/ \int_0^\infty k_1 F_{12}\,dk_1. \tag{5.3}$$

In the boundary layer this is equal to about half the width of the fully turbulent zone, which is itself quite inhomogeneous by other criteria. In contrast, $(k_1)_{12}^{-1}$ in the present flow is only one-fifth the width of the homogeneous region. This shows that we have succeeded in generating a flow in which the momentum transfer eddy structure is not only appreciably smaller than the width of the fully turbulent region but is also appreciably smaller than the laterally homogeneous region.

Next we examine the departure from stationarity in a frame convected with the centreline speed, U_c. Again the worst offenders seem to be the scales. For a quasi-stationary state, they would have to change by only small fractions during an integral time scale T in the convected frame:

$$\frac{TU_c}{\lambda_1}\frac{\partial\lambda_1}{\partial x_1} \ll 1; \quad \frac{TU_c}{L_1}\frac{\partial L_1}{\partial x_1} \ll 1. \tag{5.4}$$

Since the two-time velocity correlation coefficient in the convected frame (the envelope in figure 29) has not dropped near zero by the end of our test section, we cannot calculate its integral, T. We can, however, make a very crude estimate. Measurements in grid-generated isotropic turbulence (Comte-Bellot & Corrsin, manuscript submitted) have found $T \approx L_1/u_1'$. In a sense this T reflects the persistence of the turbulent structure when it is destroyed only by self-scrambling. The shear flow has an additional mechanism destroying its structure, viz. the mean straining, whose characteristic time is the inverse of the strain rate $d\overline{U}_1/dx_2$. Assuming that these mechanisms act more or less independently in reducing correlation, we estimate T by

$$\frac{1}{T} \approx \frac{u_1'}{L_1}+\frac{d\overline{U}_1}{dx_2}. \tag{5.5}$$

We then find that

$$\frac{TU_c}{\lambda_1}\frac{\partial\lambda_1}{\partial x_1} \approx 0{\cdot}15; \quad \frac{TU_c}{L_1}\frac{\partial L_1}{\partial x_1} \approx 0{\cdot}10; \tag{5.6}$$

so stationarity in the convected frame is only fair. It would be useful to measure the triple correlation of velocity, to see how well the first of these numbers checks with the value of $d\lambda/dt$ estimated by equation (2.13).

The levelling off of the velocity moments (figure 7) is the strongest indication that the field has reached an asymptotic state, even though this state is not stationary in the U_c-convected frame. The monotonic growth of scales (figure 17) gives the clearest measure of continuing evolution. In the presence of a constant mean velocity gradient, the growing integral scales might be expected to lead to growth in the turbulent energy production rate, thus to a growth in turbulent energy. These events are not indicated in figure 7, but should be sought in future experiments at larger dimensionless times.

It is interesting to tabulate some of the characteristic times in this experiment. Unless otherwise identified, the turbulence times in the following list are averages for the working volume, $8{\cdot}5 \leqslant x_1/h \leqslant 10{\cdot}5$.

Transit time for generator (test-section residence time):

$$T_T = \frac{\text{test-section length}}{\text{mean speed}} = \frac{9{\cdot}5\,\text{ft.}}{40{\cdot}7\,\text{ft./sec}} = 0{\cdot}23\,\text{sec.}$$

Mean straining time:

$$T_S = \left(\frac{d\overline{U}_1}{dx_2}\right)^{-1} = 0{\cdot}077\,\text{sec.}$$

Eulerian time scale in convected co-ordinates:

$$T \approx \left(\frac{u_1'}{L_1}+\frac{d\overline{U}_1}{dx_2}\right)^{-1} = 0{\cdot}056\,\text{sec.}$$

Energy spectral residence time:

$$T_E = \frac{\frac{1}{2}\overline{u_k u_k}}{-\overline{u_1 u_2}(d\overline{U}_1/dx_2)} = \frac{\bar{e}}{\epsilon} = 0{\cdot}22\,\text{sec.}$$

Root-mean-square turbulent straining time:

$$T_\sigma = \left(\frac{\nu}{\epsilon}\right)^{\frac{1}{2}} = 0{\cdot}008\,\text{sec.}$$

In order to have an asymptotic state in the wind tunnel we presumably need T_T appreciably larger than the other characteristic times listed. This condition is not met for T_E but, as remarked earlier, the levelling off of velocity moments suggests that an asymptotic state has just about been reached. Perhaps $T_T \geqslant T_E$ suffices.

Unfortunately the test section was not long enough to attain

$$R_{11}(U_c\tau, 0, 0; \tau) \leqslant 1.$$

In future work we hope to reach this region by means of larger velocity gradient and/or longer wind tunnel.

5.2. *Local isotropy*

As mentioned earlier, the relative values of the Taylor 'microscales' are consistent with local isotropy. The turbulence Reynolds number at $x_1/h = 10{\cdot}0$ is

$$R_\lambda \equiv \frac{\lambda_2}{\nu}\left(\frac{\overline{u_i u_i}}{3}\right)^{\frac{1}{2}} = 130. \tag{5.7}$$

This is probably not large enough to permit local isotropy in the inertial range of the spectrum; the dissipative region may not be remote enough from the production region (e.g. Corrsin 1957, 1958).

The expectation of local isotropy is based on the idea that the non-linear spectral energy cascade is an orientation-losing process, primarily through the cross-spectrum of pressure-velocity covariance. If an inertial subrange does exist, a necessary condition for local isotropy in the inertial region is that the Onsager spectral transfer time,

$$\tau_0(k) \equiv [k^3\mathscr{E}(k)]^{-\frac{1}{2}} \ll \left|\frac{1}{2}\frac{d\overline{U}_1}{dx_2}\right|^{-1}, \tag{5.8}$$

a measure of gross straining time. The $\frac{1}{2}$ factor is a matter of taste. k is wavenumber magnitude, $\mathscr{E}$ is three-dimensional spectrum, a concept useful primarily in isotropic turbulence. The gross strain presumably tends to cause anisotropy in all sizes of eddies. If we approximate $\mathscr{E}(k)$ by the Kolmogorov isotropic form (5.8) becomes

$$k^{\frac{2}{3}} \gg \epsilon^{-\frac{1}{3}}\left|\frac{d\overline{U}_1}{dx_2}\right|, \tag{5.9}$$

with e the viscous dissipation rate.

At $x_1/h = 10$, $\epsilon \approx 2\times 10^3\,\mathrm{cm}^2/\mathrm{sec}^3$ (see below), so (5.9) gives $k^{\frac{2}{3}} \gg 0{\cdot}5\,\mathrm{cm}^{-\frac{2}{3}}$, which might be written as $k \gg 0{\cdot}4\,\mathrm{cm}^{-1}$. At this location the Kolmogorov wave-number $k_K \equiv (\epsilon/\nu^3)^{\frac{1}{4}} \approx 28\,\mathrm{cm}^{-1}$. We infer that local isotropy is not likely to be attained at a wave-number much smaller than k_K in this flow. If local isotropy is attained, it is likely to be in the viscous (large wave-number) range. Viscous dissipation becomes important for wave-numbers greater than $0{\cdot}2\,k_K$. There exists a mixed spectral region, roughly $0{\cdot}2\,k_K \leqslant k \leqslant k_K$, where both inertial transfer and viscous dissipation are important. It is in this range that most of the dissipation occurs.

In this mixed range the characteristic spectral times (such as τ_0) are mostly the same order as the inverse r.m.s. strain rate or vorticity, $(\nu/\epsilon)^{\frac{1}{2}}$, so (5.8) is equivalent to

$$\left(\frac{\epsilon}{\nu}\right)^{\frac{1}{2}} \gg \left|\frac{d\overline{U}_1}{dx_2}\right|. \tag{5.10}$$

At $x_1/h = 10{\cdot}0$, $(\epsilon/\nu)^{\frac{1}{2}}/(d\overline{U}_1/dx_2)$ is approximately 10, which at best satisfies (5.10) marginally.

Another requirement for local isotropy is that the spectral region be at wave-numbers much larger than those at which turbulent energy production occurs. The latter was conjectured by Corrsin (1958) to be

$$k_p \approx \frac{1}{u_2'}\frac{d\overline{U}_1}{dx_2}. \tag{5.11}$$

Then we should not expect local isotropy at wave-numbers which do not satisfy

$$k \gg \frac{1}{u_2'}\frac{d\overline{U}_1}{dx_2}. \tag{5.12}$$

For dissipation local isotropy this requires at least that $k_K \gg k_p$.

At $x_1/h = 10{\cdot}0$, $k_K/k_p \approx 35$, which seems sufficient.

A more rational measure of the wave-number region for turbulent energy production is simply $(k_1)_{12}$, the first moment of the production spectrum—which is just the shear spectrum [equation (5.3)]. At $x_1/h = 10{\cdot}5$, $(k_1)_{12} = 0{\cdot}4\,\mathrm{cm}^{-1}$, the same order as k_p.

It should be remarked that this discussion and computation in terms of $F_{12}(k_1)$, the one-dimensional spectrum of $-\overline{u_1u_2}$, is less appropriate than work based on the full three-dimensional spectral density field. The more complete function will presumably be measured in turbulent shear flows when time permits it.

The turbulent energy dissipation rate is most accurately determined in this experiment by measuring the production rate and remembering that, since the energy in the convected frame is essentially constant and since spatial transfer of energy is negligible, therefore dissipation equals production:

$$\epsilon \doteqdot -\overline{u_1u_2}\,d\overline{U}_1/dx_2 = 2{\cdot}35\times 10^3\,\mathrm{cm}^2/\mathrm{sec}^3. \tag{5.13}$$

To the extent that the dissipation occurs primarily in a locally isotropic part of the spectrum, we can also determine ϵ from any one of the mean square velocity derivatives. The values of λ_1 (§4.3) were mostly measured by time differentiation and invocation of the Taylor approximation in the form $\partial/\partial t \doteq -\overline{U}_1 \partial/\partial x_1$ to get $\overline{(\partial u_1/\partial x_1)^2}$. In these terms the dissipation is

$$\epsilon \doteq 15\nu\overline{(\partial u_1/\partial x_1)^2} = 1{\cdot}93 \times 10^3\,\mathrm{cm}^2/\mathrm{sec}^2, \tag{5.14}$$

presumably a less reliable value than (5.13).

The fully isotropic formulas for ϵ, involving mean square velocity components, are likely to be even less accurate, because $\overline{u_1^2}$, $\overline{u_2^2}$ and $\overline{u_3^2}$ are set primarily outside of the locally isotropic part of the spectrum.

A direct measure of departure from local isotropy in the spectral range which determines the first derivatives (hence the dissipation) is the estimated correlation between $\partial u_1/\partial x_1$ and $\partial u_1/\partial x_2$ (§5.5):

$$\overline{\frac{\partial u_1}{\partial x_1}\frac{\partial u_1}{\partial x_2}} \Big/ \left[\overline{\left(\frac{\partial u_1}{\partial x_1}\right)^2}\,\overline{\left(\frac{\partial u_1}{\partial x_2}\right)^2}\right]^{\frac{1}{2}} \approx -0{\cdot}21. \tag{5.15}$$

For isotropy this is zero.

Although the three one-dimensional spectra have relative forms nearly consistent with an inertial, locally isotropic subrange $0{\cdot}03 \leqslant \eta k_1 \leqslant 0{\cdot}15$, the shear correlation coefficient spectrum (figure 22) indicates that this region is significantly non-isotropic: ${}_{k_1}R_{12}$ varies between 0·4 and 0·05. ${}_{k_1}R_{12}$ is, however, very small in the viscous region.

Bradshaw (1967) has noted for other flows the presence of spectral forms consistent with local isotropy in a wave-number range where ${}_{k_1}R_{12}$ is appreciable. He suggested that $|{}_{k_1}R_{12}| \ll 1$ is too strong a condition (perhaps sufficient, but not necessary), and he proposed the weaker one,

$$\left|\int_{k_1}^{\infty} F_{12}\,dk_1\right| \ll \left|\int_0^{\infty} F_{12}\,dk_1\right|. \tag{5.16}$$

In the present flow Bradshaw's relation is satisfied for $\eta k_1 > 0{\cdot}03$. On the other hand, we believe the spectrum to be appreciably non-isotropic at larger k_1 [particularly in view of (5.15)]. Furthermore, there is no reason to believe that turbulence which is isotropic around wave-number k_1^* would be non-isotropic at $k_1 > k_1^*$. Therefore we conclude that the Kolmogorov '$-\frac{5}{3}$ law', even with proper component spectral magnitudes, is a relatively insensitive indicator of local isotropy.

5.3. *The Reynolds stress tensor*

One of the main reasons that the stress/strain-rate relation for turbulent shear flows cannot be Newtonian is that the stress tensor $\sigma_{ik} \equiv -\overline{u_i u_k}$ and the strain-rate tensor $E_{lm} \equiv \partial \overline{U}_l/\partial x_m + \partial \overline{U}_m/\partial x_l$ are not generally aligned (Corrsin 1957).

In this rectilinear flow the strain-rate principal axes are at angles $\alpha_E = \pm 45°$, while the σ_{ik} principal axes are at

$$\alpha_\sigma = \tfrac{1}{2}\tan^{-1}\left\{\frac{2\overline{u_1 u_2}}{\overline{u_1^2} - \overline{u_2^2}}\right\} = -28°, 62°. \tag{5.17}$$

This relative orientation is much like that found in boundary-layer and channel flows (away from the symmetry axis), where

$$\left.\begin{aligned} \alpha_E &\doteq \pm 45°, \\ \alpha_\sigma &\approx -20° \text{ to } -25°,\ 70° \text{ to } 65°, \end{aligned}\right\} \tag{5.18}$$

and is quite different from that in the plane wake (away from the symmetry axis), where

$$\left.\begin{aligned} &\alpha_E \doteq \pm 45^\circ, \\ &\alpha_\sigma \approx 40^\circ \text{ to } 50^\circ,\ -50^\circ \text{ to } -40^\circ. \end{aligned}\right\} \tag{5.19}$$

As remarked earlier (Corrsin 1957), the rough equality in the wake may be related to the empirical fact that such 'free' shear flows can be approximated with gradient transport (quasi-Newtonian) models, even though such models are wrong in principle.

The two principal stressses in the (x_1, x_2) plane are

$$-\sigma_{a,b} = \frac{\overline{u_1^2}+\overline{u_2^2}}{2} \pm \left[\left(\frac{\overline{u_1^2}-\overline{u_2^2}}{2}\right)^2 + (\overline{u_1u_2})^2\right]^{\frac{1}{2}}, \tag{5.20}$$

and the ratio in the present flow is

$$\sigma_a/\sigma_b = 2{\cdot}3. \tag{5.21}$$

For comparison, the ranges of values in three traditional flows are

$$\left.\begin{aligned} &\text{boundary layer: } && \sigma_a/\sigma_b = 3 \text{ to } 4, \\ &\text{channel: } && \sigma_a/\sigma_b = 3 \text{ to } 5, \\ &\text{plane wake: } && \sigma_a/\sigma_b = 2 \text{ to } 6. \end{aligned}\right\} \tag{5.22}$$

If we insist on computing an 'eddy viscosity', $\nu_T \equiv -\overline{u_1u_2}/(d\overline{U}_1/dx_2)$, we find $\nu_T = 13{\cdot}2\,\text{cm}^2/\text{sec}$, so $\nu_T/\nu = 91$. For comparison, $\nu_T/\nu = 200$ in the boundary layer at $x_2/\delta = 0{\cdot}5$ (Klebanoff 1955).

A further comparison between the present flow and traditional ones is given by the ratios of turbulent to mean flow strain rates:

Flow	Position, x_2/δ	$\left(\frac{\epsilon}{\nu}\right)^{\frac{1}{2}} \bigg/ \frac{d\overline{U}_1}{dx_2}$
Boundary layer (Klebanoff 1955)	0·1	2·5
	0·5	9·3
	0·9	5·5
Channel (Laufer 1951)	0·1	5·3
	0·5	7·6
	0·9	16
'Homogeneous' shear	$(x_1/h = 10)$, any x_2	9·8

In this table, δ is boundary-layer thickness and half-width of the channel. The value of $(\epsilon/\nu)^{\frac{1}{2}}/(d\overline{U}_1/dx_2)$ in the boundary layer at $x_2/\delta = 0{\cdot}9$ becomes 27 if we divide by the local 'intermittency factor', the fraction of time that the hot-wire probe was in turbulent fluid.

5.4. *A pressure-velocity covariance tensor*

In §2 we are reminded that the one-point covariances $\overline{p\,\partial u_1/\partial x_1}$, $\overline{p\,\partial u_2/\partial x_2}$ and $\overline{p\,\partial u_3/\partial x_3}$ are intercomponent transfer rates of turbulent kinetic energy. A related term, $\overline{p(\partial u_1/\partial x_2 + \partial u_2/\partial x_1)}$, acts on the turbulent shear stress. Turbulent shear flows with nearly parallel mean streamlines (boundary layers, channels, wakes, jet cores, etc.) receive their turbulent energies almost entirely in the streamwise velocity component, yet the three component energies are observed to be the same order. It follows that the intercomponent transfer is a key phenomenon. Since the turbulent shear governs the mean momentum distribution, the pressure-velocity covariance which helps to set the shear stress level by balancing against the shear production rate must also be central to turbulent flow dynamics.

The difficulties of making reliable measurements of static pressure fluctuations (except on smooth walls) have caused the gathering of such data to lag far behind the measurement of velocity moments by hot-wire anemometer. This nearly homogeneous shear flow opens a side door to pressure-velocity covariance determination by simplifying the moment equations. Rotta (1962) first suggested this approach in connexion with traditional shear flows. In the present flow the component energy and shear stress equations (2.6) and (2.7) reduce roughly to

$$0 \approx -\overline{u_1u_2}\frac{d\overline{U}_1}{dx_2} + \frac{1}{\rho}\overline{p\frac{\partial u_1}{\partial x_1}} - \frac{\epsilon}{3}, \tag{5.23}$$

$$0 \approx +\frac{1}{\rho}\overline{p\frac{\partial u_2}{\partial x_2}} - \frac{\epsilon}{3}, \tag{5.24}$$

$$0 \approx +\frac{1}{\rho}\overline{p\frac{\partial u_3}{\partial x_3}} - \frac{\epsilon}{3}, \tag{5.25}$$

$$0 \approx -\overline{u_2^2}\frac{d\overline{U}_1}{dx_2} + \frac{1}{\rho}\overline{p\left(\frac{\partial u_1}{\partial x_2} + \frac{\partial u_2}{\partial x_1}\right)}. \tag{5.26}$$

These equations also assume local isotropy in the dissipative spectral range, a condition only roughly met in this experiment, but one which could be improved by increasing R_λ.

We see that all terms but the pressure-velocity covariances have been directly measured by hot-wire anemometer. The equations then give us the required covariances. The only other flows in which these terms have been determined are unsheared, nearly homogeneous, non-isotropic turbulence generated by a uniform grid followed by gross strain (e.g. Uberoi 1957).

Expressed compactly in terms of ϵ, equations (5.23, 24, 25) give energy loss rate from $\overline{u_1^2}$ shared equally by $\overline{u_2^2}$ and $\overline{u_3^2}$:

$$\frac{1}{\rho}\overline{p\frac{\partial u_1}{\partial x_1}} = -\tfrac{2}{3}\epsilon, \quad \frac{1}{\rho}\overline{p\frac{\partial u_2}{\partial x_2}} = \frac{1}{\rho}\overline{p\frac{\partial u_3}{\partial x_3}} = \tfrac{1}{3}\epsilon. \tag{5.27}$$

This equality of transfer rates into $\overline{u_2^2}$ and $\overline{u_3^2}$ is due merely to the assumption of local isotropy. We do not expect exact equality because u_2 is directed along the only important mean gradient in the field, $d\overline{U}_1/dx_2$, while u_3 is normal to it. Furthermore, we note from figure 10 that $\overline{u_2^2} \neq \overline{u_3^2}$. As in boundary layers and channels, $\overline{u_3^2} > \overline{u_2^2}$ in this 'homogeneous' case.

A dramatic difference between $\overline{p\,\partial u_2/\partial x_2}$ and $\overline{p\,\partial u_3/\partial x_3}$ turns up in the correlation-discard calculations by Deissler (1961) and Fox (1964). They have computed some of the properties of a suddenly sheared isotropic turbulence, discarding triple velocity covariances but keeping pressure-velocity covariances. Their calculations give a healthy transfer from $\overline{u_1^2}$ to $\overline{u_3^2}$, but lack adequate transfer to $\overline{u_2^2}$, so that component dies out an order of magnitude more rapidly than the others. Their computations are interesting because they reveal (presumably over-emphasize) possible differences between $\overline{p\,\partial u_2/\partial x_2}$ and $\overline{p\,\partial u_3/\partial x_3}$ at small Reynolds numbers. Alternatively, it is possible that their truncation is not self-consistent.

As hypothesis for the intercomponent transfer rates Rotta (1951, 1962) proposed a linear dependence on component energy deficiency (relative to the average), in effect

$$\left.\begin{aligned}\frac{1}{\rho\epsilon}\overline{p\frac{\partial u_1}{\partial x_1}} &= -C\frac{(\overline{u_1^2}-\frac{1}{3}\overline{u_ku_k})}{\frac{1}{3}\overline{u_ku_k}},\\ \frac{1}{\rho\epsilon}\overline{p\frac{\partial u_2}{\partial x_2}} &= -C\frac{(\overline{u_2^2}-\frac{1}{3}\overline{u_ku_k})}{\frac{1}{3}\overline{u_ku_k}},\\ \frac{1}{\rho\epsilon}\overline{p\frac{\partial u_3}{\partial x_3}} &= -C\frac{(\overline{u_3^2}-\frac{1}{3}\overline{u_ku_k})}{\frac{1}{3}\overline{u_ku_k}}.\end{aligned}\right\} \tag{5.28}$$

From the data of figure 10, the three Rotta relations give $C = 1{\cdot}5,\ 1{\cdot}2,\ 2{\cdot}0$. If Rotta's conjecture were exact, these would be equal. We conclude that it is a plausible first step for shear flow. He concluded from calculations on the data of Uberoi (1957) that it works within a factor of 2 for irrotationally strained isotropic turbulence.

The analysis of the pressure-velocity covariance terms can be taken further if we note that they are components of a second-rank symmetric tensor,

$$P_{ik} \equiv \frac{1}{\rho}\overline{p\left(\frac{\partial u_i}{\partial x_k}+\frac{\partial u_k}{\partial x_i}\right)}, \tag{5.29}$$

the pressure/strain-rate covariance, which actually appears in the balance equation for $\overline{u_iu_k}$ (Chou 1945). For the present flow, the above equations plus the replacement of dissipation by production permit the approximation

$$P_{ik} \approx \frac{d\overline{U}_1}{dx_2}\begin{Bmatrix}\frac{4}{3}\overline{u_1u_2} & \overline{u_2^2} & 0\\ \overline{u_2^2} & -\frac{2}{3}\overline{u_1u_2} & 0\\ 0 & 0 & -\frac{2}{3}\overline{u_1u_2}\end{Bmatrix}. \tag{5.30}$$

The principal-axis directions in the (x_1, x_2) plane are given by

$$\alpha_P \approx -\tan^{-1}\left(\frac{\overline{u_1u_2}}{\overline{u_2^2}}-\left[1+\left(\frac{\overline{u_1u_2}}{\overline{u_2^2}}\right)^2\right]^{\frac{1}{2}}\right). \tag{5.31}$$

With the measured moments, these are

$$\alpha_P \approx -28^\circ,\ 62^\circ, \tag{5.32}$$

which is *equal to the orientation of the Reynolds stress tensor*, within the accuracy of the measurements. The corresponding principal values are

$$P_{a,b} \approx \frac{d\overline{U}_1}{dx_2}\left(\tfrac{1}{3}\overline{u_1u_2} \mp [(\overline{u_1u_2})^2+(\overline{u_2^2})^2]^{\frac{1}{2}}\right). \tag{5.33}$$

Like the stress tensor, P_{ik} has its third principal axis along x_3, and the corresponding value is

$$P_c = P_{33} = -\frac{2}{3}\frac{d\overline{U}_1}{dx_2}\overline{u_1u_2}. \tag{5.34}$$

The corresponding principal value of σ_{ik} is $\sigma_c = -\overline{u_3^2}$.

An important consequence of the alignment of σ_{ik} and P_{lm} is that inspection of the shear flow in the common principal-axis co-ordinates presents a view very much like the irrotational homogeneous strain problem, in which both σ_{ik} and P_{lm} are diagonalized. Townsend (1956) proposed the first theory for inferring shear stress in a shear flow from the level of anisotropy in unsheared turbulence subjected to homogeneous irrotational strain.

We can now test Rotta's linear intercomponent energy transfer, equation (5.28), for the present flow in principal-axis co-ordinates. In cm^2/sec^2 units the principal values of the Reynolds stress tensor (now only kinetic energies) are $\overline{u_a^2} = 600$, $\overline{u_b^2} = 155$, $\overline{u_c^2} = 292$. The corresponding values of intercomponent energy transfer rate are

$$\frac{1}{\rho\epsilon}P_a = -1{\cdot}02, \quad \frac{1}{\rho\epsilon}P_b = 0{\cdot}68, \quad \frac{1}{\rho\epsilon}P_c = 0{\cdot}33.$$

The (hopefully) common proportionality factor of the equation analogous to (5.28) has the three values $C' = 1{\cdot}4$, $1{\cdot}3$, $2{\cdot}0$. The third number is of course the same in both co-ordinate systems.

Rotta proposed an equation like (5.28), and using the same empirical constant, for estimating the pressure-velocity covariance term in the shear stress equation (5.26). Evidently he visualized rotating the principal-axis energy estimates back into 'laboratory co-ordinates'. His P_{12} suggestion can be combined with (5.28), by writing

$$\frac{1}{2\rho\epsilon}P_{ik} = \frac{C}{\frac{2}{3}\overline{e}}[\sigma_{ik} - {}_I\sigma_{ik}], \tag{5.35}$$

where ${}_I\sigma_{ik} \equiv \frac{2}{3}\overline{e}\,\delta_{ik}$, the form of σ_{ik} in isotropic turbulence with the same energy. δ_{ik} is the Kronecker delta, equal to 1 for $i = k$, 0 for $i \neq k$.

This form emphasizes Rotta's implicit assumption of the coincidence of the principal axes of P_{ik} and σ_{jl}, a condition which does not follow in general from the second moment equations—and which may not be true for all flows. We have found experimentally that it holds in our nearly homogeneous shear flow, so in this flow Rotta's proportionality hypothesis is not ruled out *a priori*. It seems plausible that the principal axes of P_{ik} and σ_{jl} be approximately the same in boundary layers and channels which have no major downstream evolution due to mean pressure gradients.

5.5. *Spatial iso-correlation curves*

In isotropic turbulence spatial iso-correlation curves $R_{11}(r_1, r_2, 0; 0) = \text{const.}$ are ovals, symmetric about r_1 and r_2 axes. Figure 25 shows that turbulence undergoing nearly homogeneous shear straining departs systematically from symmetry, at least in the r_1 direction. Unfortunately our data are confined to one quadrant, but a comparison with isotropic turbulence data [figure 44, data adapted from Comte-Bellot & Corrsin (manuscript submitted)] emphasizes a characteristic difference especially near the r_2 axis, where the shear case does not intersect normally. The principal axis of the mean strain-rate tensor in this quadrant is at 45° to the r_1 axis; that of the Reynolds stress tensor is 62°. It may be significant that forms of the shear case iso-correlation curves cannot be simulated by simply tilting the isotropic ones.

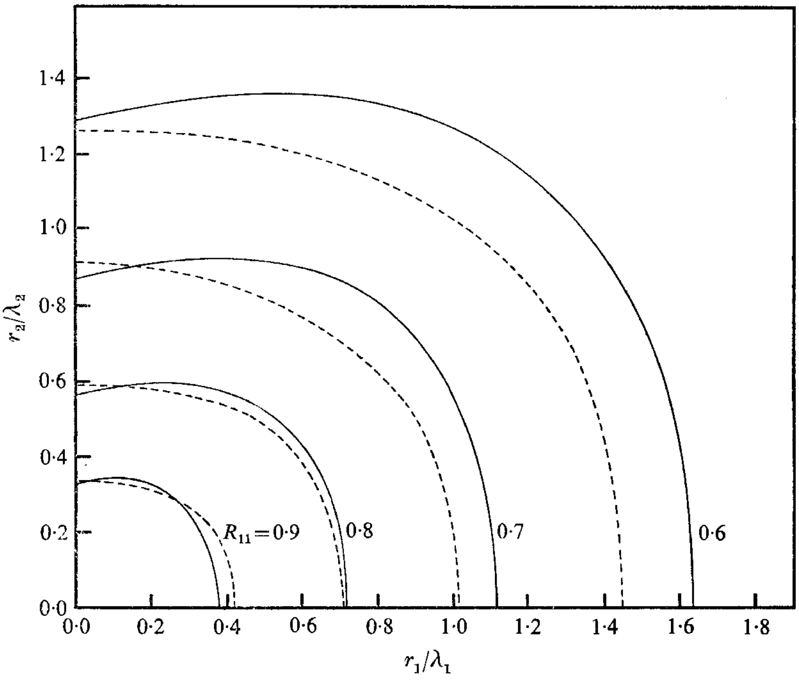

FIGURE 44. Contrast between typical spatial iso-correlation contours $[R_{11}(r_1, r_2, 0; 0)]$ in the shear flow and in nearly isotropic turbulence generated by a grid. The shapes (rather than the average radii) are the relevant information. ——, nearly homogeneous shear turbulence; – – –, nearly isotropic grid turbulence.

A truncated power series approximation to R_{11} helps to extract additional quantitative information. If $u_1(\mathbf{x}+\mathbf{r}, t)$ is expressed as a power series in r_1 and r_2, with $r_3 = 0$, the series for R_{11} to fifth order in r, assuming homogeneity, is

$$\begin{aligned} R_{11}(r_1, r_2, 0; 0) = 1 &- \frac{1}{2\overline{u_1^2}}\left[\overline{\left(\frac{\partial u_1}{\partial x_1}\right)^2} r_1^2 + 2\overline{\left(\frac{\partial u_1}{\partial x_1}\right)\left(\frac{\partial u_1}{\partial x_2}\right)} r_1 r_2 + \overline{\left(\frac{\partial u_1}{\partial x_2}\right)^2} r_2^2\right] \\ &+ \frac{1}{24\overline{u_1^2}}\left[\overline{\left(\frac{\partial^2 u_1}{\partial x_1^2}\right)^2} r_1^4 + 4\overline{\left(\frac{\partial^2 u_1}{\partial x_1^2}\right)\left(\frac{\partial^2 u_1}{\partial x_1 \partial x_2}\right)} r_1^3 r_2 + 6\overline{\left(\frac{\partial^2 u_1}{\partial x_1^2}\right)\left(\frac{\partial^2 u_1}{\partial x_2^2}\right)} r_1^2 r_2^2\right. \\ &\left. + 4\overline{\left(\frac{\partial^2 u_1}{\partial x_1 \partial x_2}\right)\left(\frac{\partial^2 u_1}{\partial x_2^2}\right)} r_1 r_2^3 + \overline{\left(\frac{\partial^2 u_1}{\partial x_2^2}\right)^2} r_2^4\right] + O(r^6). \end{aligned} \tag{5.36}$$

The slopes at $r_1 = 0$ and $r_2 = 0$ are

$$\left.\frac{\partial R_{11}}{\partial r_1}\right|_{r_1=0} = -\frac{1}{\overline{u_1^2}}\overline{\left(\frac{\partial u_1}{\partial x_1}\right)\left(\frac{\partial u_1}{\partial x_2}\right)}\, r_2 + \frac{1}{6\overline{u_1^2}}\overline{\left(\frac{\partial^2 u_1}{\partial x_1 \partial x_2}\right)\left(\frac{\partial^2 u_1}{\partial x_2^2}\right)}\, r_2^3 + \ldots \tag{5.37}$$

and
$$\left.\frac{\partial R_{11}}{\partial r_2}\right|_{r_2=0} = -\frac{1}{\overline{u_1^2}}\overline{\left(\frac{\partial u_1}{\partial x_1}\right)\left(\frac{\partial u_1}{\partial x_2}\right)}\, r_1 + \frac{1}{6\overline{u_1^2}}\overline{\left(\frac{\partial^2 u_1}{\partial x_1^2}\right)\left(\frac{\partial^2 u_1}{\partial x_1 \partial x_2}\right)}\, r_1^3 + \ldots. \tag{5.38}$$

The eight derivative moments in (5.36) were determined from the correlation data. The values, in the order in which they occur in (5.36), are $1{\cdot}0\times 10^3$, $-2{\cdot}9\times 10^2$, $1{\cdot}9\times 10^3$, $1{\cdot}9\times 10^5$, $-1{\cdot}7\times 10^5$, $1{\cdot}1\times 10^5$, $-5{\cdot}3\times 10^3$, $2{\cdot}5\times 10^5$. The units are inches and seconds.

Putting R_{11} = constant in (5.36), we get equations for the iso-correlation contours at small r. These can be used to infer particular properties, such as the slopes at the axis intersections:

$$\left.\frac{dr_2}{dr_1}\right|_{r_1=0} = \frac{-\overline{\left(\frac{\partial u_1}{\partial x_1}\right)\left(\frac{\partial u_1}{\partial x_2}\right)} + \frac{1}{6}\overline{\left(\frac{\partial^2 u_1}{\partial x_1 \partial x_2}\right)\left(\frac{\partial^2 u_1}{\partial x_2^2}\right)}\, r_2^2}{\overline{\left(\frac{\partial u_1}{\partial x_2}\right)^2} - \frac{1}{6}\overline{\left(\frac{\partial^2 u_1}{\partial x_2^2}\right)^2}\, r_2^2}, \tag{5.39}$$

$$\left.\frac{dr_2}{dr_1}\right|_{r_2=0} = \frac{-\overline{\left(\frac{\partial u_1}{\partial x_1}\right)^2} + \frac{1}{6}\overline{\left(\frac{\partial^2 u_1}{\partial x_1^2}\right)^2}\, r_1^2}{\overline{\left(\frac{\partial u_1}{\partial x_1}\right)\left(\frac{\partial u_1}{\partial x_2}\right)} - \frac{1}{6}\overline{\left(\frac{\partial^2 u_1}{\partial x_1^2}\right)\left(\frac{\partial^2 u_1}{\partial x_1 \partial x_2}\right)}\, r_1^2}. \tag{5.40}$$

With the moments estimated from the measured correlation functions, these two expressions were used as aids in fairing curves through the scattered data of figure 25. In the case of (5.40), we don't even need the numerical values listed above: the denominator of (5.40) is proportional to the first two terms in (5.38), and figure 24 suggests that $(\partial R_{11}/\partial r_2)|_{r_2=0} = 0$, so we conclude that the iso-correlation contours at small r intersect the r_1 axis normally. This is consistent with the tabulated moment values for $r_1 \leqslant 0{\cdot}18$ in.

The numerator of (5.39) is proportional to the first two terms in (5.37). Figure 23 shows that $(\partial R_{11}/\partial r_1)|_{r_1=0} > 0$, so $(dr_2/dr_1)|_{r_1=0} > 0$ if the denominator $\geqslant 0$, a condition which is met for $r_1 \leqslant 0{\cdot}21$ in., at least.

For both sets of axis intersections, the small r behaviour seemed consistent with the large r data as well.

5.6. *Space-time iso-correlation curves with optimum delay*

As discussed in §4.2, space-time correlation in a frame convected with $\tilde{U}$, the average speed of the r_2 slab of fluid bounded by the probes, would be desirable. Since we have insufficient data to extract iso-correlation contours in that frame, we have inferred results which are easier to get and nearly the same in this flow, viz. the iso-correlation contours with $\tau = \tau_M$, figure 42.

Another reason for inspecting these functions is that Favre, Gaviglio & Dumas have studied them extensively in the boundary layer. They have established a characteristic 'kidney shape' (figure 40 of Favre, Gaviglio & Dumas 1955;

figures 7, 8 of Favre, Gaviglio & Dumas 1958), and we can ask if this is due simply to the shear or if it is due to the transverse inhomogeneity.

Although our data are restricted to one quadrant, this is sufficient to show that the homogeneous shear flow does not have its *maximum maximorum* in the (r_1, r_2) plane on a line which is concave toward the high-velocity side. It appears to be on the r_1 axis instead. A second difference is that the present flow shows distinct upstream–downstream unsymmetry (e.g. by $(dr_2/dr_1)|_{r_1=0} \neq 0$ for the $R_{11}^{(M)}$ = constant contours), while the boundary-layer contours are virtually symmetric about the r_2 axis.

As in the pure spatial case, some symmetry properties for small r and τ can be inferred by Taylor series expansion of $u_1(\mathbf{x}+\mathbf{r}, t+\tau)$ about $(\mathbf{x}, t)$. If we assume both stationarity and homogeneity, and truncate the expansions at the quadratic terms ($\sim r_1^2, r_2^2, r_1 r_2, r_1 \tau, r_2 \tau, \tau^2$), hence $[1-R_{11}^{(M)}] \ll 1$, the iso-correlation ellipses, $r_2(r_1; \tau)$, are tilted. This is consistent with the contours drawn in figure 42 except near the r_1 axis. Our decision to sketch the contours normal to the r_1 axis was governed partly by the trends in data for additional $R_{11}^{(M)}$ values (omitted here for brevity) and by the good approximation to r_2 symmetry displayed in $R_{11}^{(M)}(0, r_2, r_3)$ (figure 43). Of course none of these data corresponds to signal separations small enough for the Taylor series analysis to be surely applicable. There is a clear need for more extensive data, including all four quadrants in the (r_1, r_2) plane.

This research was begun and continued from 1966 to 1968 with the support of the U.S. Air Force Office of Scientific Research, with help from the Boeing Scientific Research Laboratories. During the past year it has been supported by the U.S. Atomic Energy Commission. We should like to thank Hervé Buthaud for his help in recording and processing data, and a referee for his critical reading of the manuscript.

Appendix. Probe interference study

A hot-wire probe inevitably changes the flow field around it, especially on the downwind side. This probe wake consists of extraneous alterations not only in mean and turbulent velocity fields, but in temperatures as well. When we seek correlation data at two space points such that the downstream probe may be in the wake of the upstream one, we must either make suitable corrections to the measurements or avoid the wake and infer the corresponding data by interpolation/extrapolation. We chose the latter course. Favre, Gaviglio & Dumas (1955) indicate a wake effect on correlation for their 'old probe', remarking that improved streamlining reduced this effect.

Figure 45 shows the two-probe configuration. For small r_1 it is the wake of the upstream wire itself which must be avoided; at larger r_1 the needle and full probe wakes were involved. For $r_1 \geqslant 4{\cdot}0$ in., no wake effect could be detected when the downstream probe was at $r_2 \geqslant 0$, so no extrapolation was necessary.

It should be mentioned parenthetically that figure 45 does not apply to the measurements of $R_{11}(0, 0, r_3; \tau)$, for which the wires were set parallel to x_2.

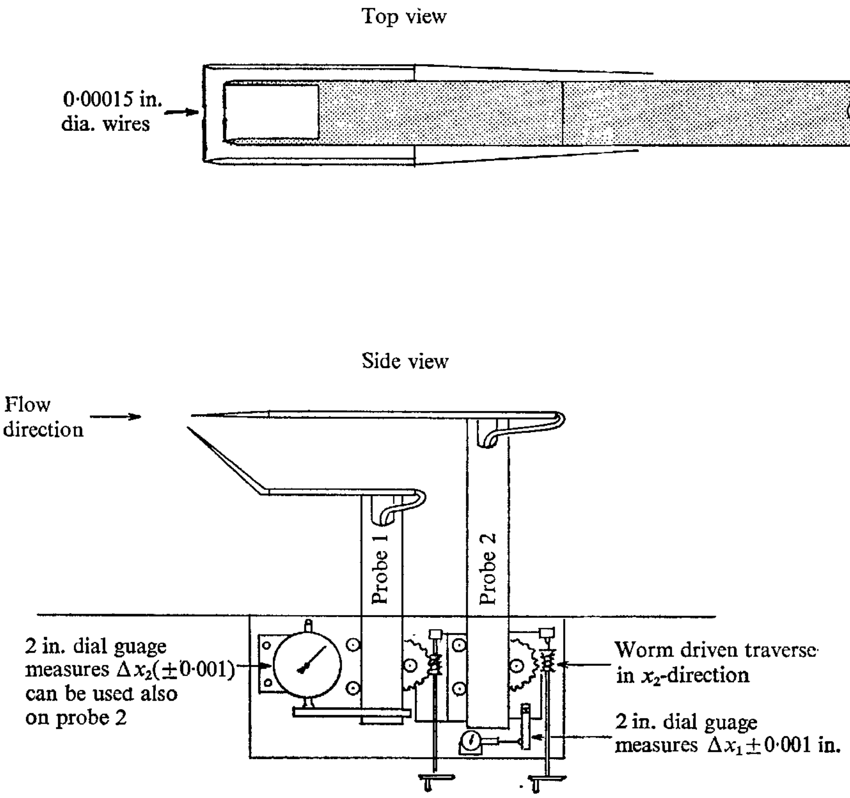
Top view

Side view

FIGURE 45. Sketch of hot-wire probe configuration.

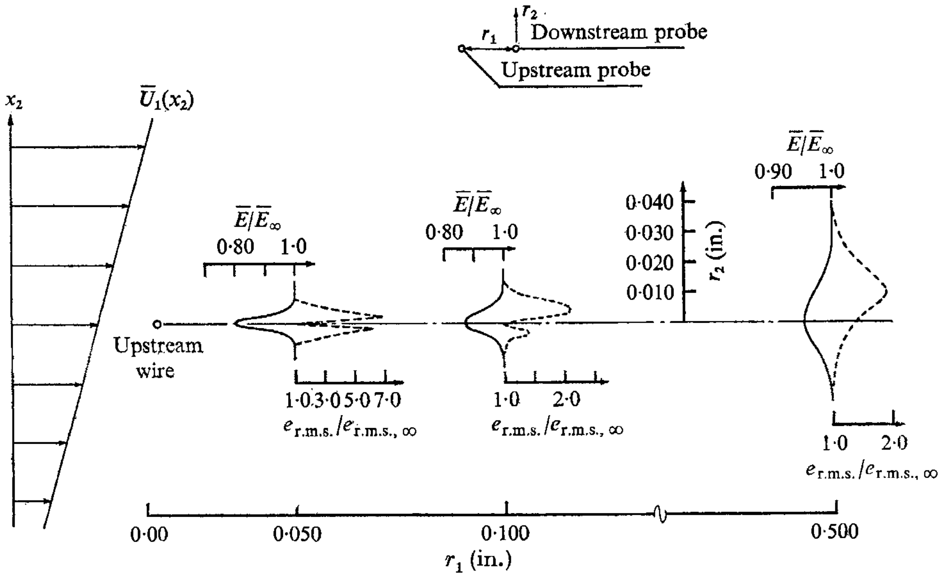

FIGURE 46. Mean velocity and fluctuation profiles close behind upstream hot-wire.

The influence of the upstream probe on the reading of the downstream probe is shown qualitatively in figure 46. The small inserted plots show values of mean and fluctuating linearizer output voltages, $\bar{E}$ and $e_{\mathrm{r.m.s.}}$ respectively, at various r_1 stations, functions of r_2. The subscript ∞ denotes conditions outside the wake.

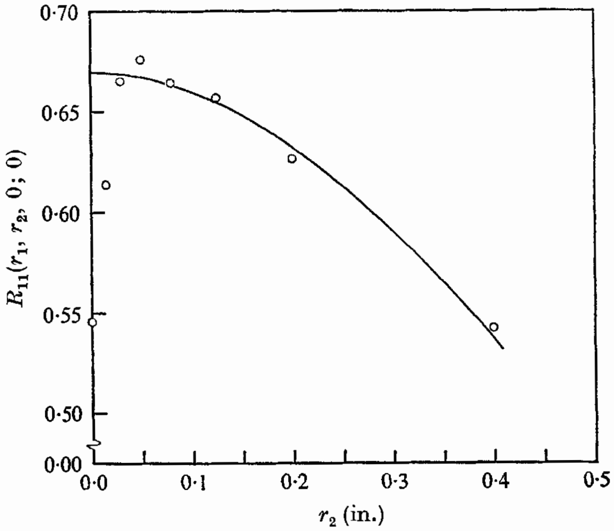

FIGURE 47. Example of least-squares extrapolation technique to avoid wake interference error. $r_1 = 0{\cdot}5$ in. ○, measured; ——, estimated.

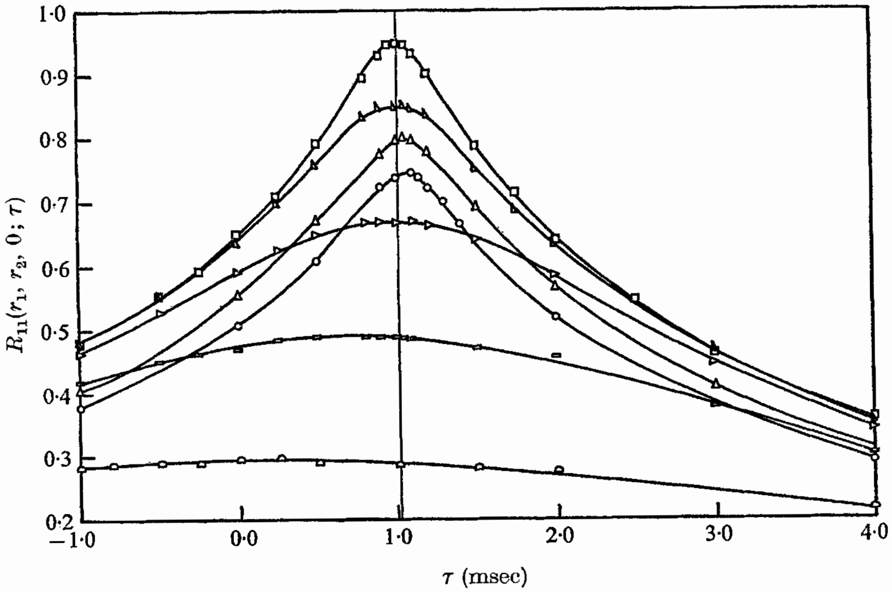

FIGURE 48. Illustration of error in space-time correlation function $[R_{11}(r_1, r_2, 0; \tau)]$ when downstream wire is in wake of upstream wire ($r_2 < 0{\cdot}035$ in.). The peaks should increase monotonically with decreasing r_2. $r_1 = 0{\cdot}50$ in. ○, $r_2 = 0{\cdot}0$ in.; △, $r_2 = 0{\cdot}010$ in.; □, $r_2 = 0{\cdot}035$ in.; ◺, $r_2 = 0{\cdot}10$ in.; ▷, $r_2 = 0{\cdot}25$ in.; ▭, $r_2 = 0{\cdot}50$ in.; ⏢, $r_2 = 1{\cdot}000$ in.

No attempt has been made to differentiate between velocity and temperature responses. The r.m.s. fluctuating voltage exhibits a double-lobed character for small r_1. At larger r_1 the double lobes blend into a single, off-axis curve.

Figure 47 (circle data points) shows the behaviour of the recorded correlation coefficient $R_{11}(r_1, r_2, 0; 0)$ as one traverses in the r_2 direction at $r_1 = 0{\cdot}5$ in. At the point $r_2 = 0$ the apparent correlation coefficient is 20 % below the value obtained at $r_2 = 0{\cdot}05$ in. Presumably it should have a maximum at $r_2 = 0$.

To estimate $R_{11}(r_1, 0, 0; 0)$ we extrapolate the correlation data in the small r_2 region using only data judged to have been taken outside the wake. Furthermore, we use the earlier inference that $R_{11}(r_1, r_2, 0; 0)$ is symmetric in r_2, therefore we extrapolate with a least squares parabola with vertex at $r_2 = 0$. The diamond points identify the parabola in figure 47. For very small r_1, extrapolation was done simply by inspection.

The correlation in the wake drops off with increasing r_1 more rapidly than that in the basic flow because the narrowness of the mean shear zone around the wire and in its near wake reduces the scale of the turbulence produced. This also causes important errors in the space-time correlation, as illustrated in figure 48. Not only does the correlation level drop off more rapidly in time (smaller scale with increased r.m.s. velocity implies smaller characteristic times), but also the peak arrival time is shifted. Although the 6 % error in τ_M may seem fairly small, it is conceptually very serious because it actually reverses the sign of $\tau_M - r_1/\bar{U}$.

REFERENCES

Bakewell, H. P. 1966 An experimental investigation of the viscous sublayer in turbulent pipe flow. Thesis for Ph.D. degree, Penn State University.

Baldwin, L. V. & Mickelsen, W. R. 1962 *J. Engng Mech. Div., Am. Soc. C.E.* **88**, 37 (Discussion, 151).

Batchelor, G. K. 1950 *J. Aero. Sci.* **17**, 441.

Batchelor, G. K. 1953 *The Theory of Homogeneous Turbulence*. Cambridge University Press.

Boussinesq, J. 1877 *Essai sur la Théorie des Eaux Courantes*. Mém. présentés par div. sav. à l'Acad. des Sci.

Bradshaw, P. 1967 *Nat. Phys. Lab. Aero Rep.* no. 1220.

Burgers, J. M. & Mitchner, M. 1953 *Konink. Ned. Akad. v. Wet.* B **15**, 228 (part II, 383).

Chou, P. Y. 1945 *Quart. J. Appl. Math.* **3**, 38.

Comte-Bellot, G. & Corrsin, S. 1970 Manuscript submitted to *J. Fluid Mech.*

Corrsin, S. 1949 *J. Aero. Sci.* **16**, 757.

Corrsin, S. 1957 *Proc. 1st Naval Hydro-Symp.*, Pub. 515. *Natn. Acad. Sci./Natn. Res. Counc.*, 373.

Corrsin, S. 1958 *N.A.C.A. Res. Memo* RM 58B11.

Corrsin, S. 1963 *Encyclopedia of Physics*, vol. VIII/2. (Ed. S. Flügge and C. Truesdell.) Berlin: Springer-Verlag.

Craya, A. 1958 *Publ. Sci. et Tech. du Min. de l'Air*, no. 345.

Deissler, R. G. 1961 *Phys. Fluids*, **4**, 1187.

Favre, A., Gaviglio, J. & Dumas, R. 1953 *La Rech. Aéro.* (32), 21.

Favre, A., Gaviglio, J. & Dumas, R. 1955 *La Rech. Aéro.* (48), 3 (see also *J. Fluid Mech.* **2**, 313).

Favre, A., Gaviglio, J. & Dumas, R. 1958 *J. Fluid Mech.* **3**, 344.

FAVRE, A., GAVIGLIO, J. & DUMAS, R. 1967 *Phys. Fluids Suppl.* **10**, II, S138.

FISHER, M. J. & DAVIES, P. O. A. L. 1964 *J. Fluid Mech.* **18**, 97.

FOX, J. 1964 *Phys. Fluids*, **7**, 562.

HASEN, E. M. 1967 *J. Fluid Mech.* **29**, 721.

HINZE, J. O. 1959 *Turbulence.* New York: McGraw-Hill.

VON KÁRMÁN, TH. 1930 *Nachr. Ges. Wiss., Göttingen, Math. Phys. Kl.*, 58 (see also *N.A.C.A.* TM 611).

KELLOGG, R. M. 1965 Ph.D. dissertation, Johns Hopkins University.

KLEBANOFF, P. S. 1955 *N.A.C.A. Rep.* 1247.

KOLMOGOROV, 1941 *C.R. Akad. Sci. U.R.S.S.* **30**, 301.

LANDAHL, M. 1967 *J. Fluid Mech.* **29**, 441.

LAUFER, J. 1951 *N.A.C.A. Rep.* 1053.

LIN, C. C. 1953 *Quart. J. Appl. Math.* **10**, 295.

LUMLEY, J. L. 1965 *Phys. Fluids*, **8**, 1056.

LUMLEY, J. L. 1967 *Phys. Fluids*, **10**, 1405.

MOFFATT, H. K. 1967 *Atmospheric Turbulence and Radio Wave Propagation.* Moscow: Publ. House 'Nauka'.

NEE, V. W. & KOVASZNAY, L. S. G. 1969 *Phys. Fluids*, **12**, 473.

NEVZGLJADOV, V. 1945 *J. Phys.* (*USSR*), **9**, 235.

PEARSON, J. R. A. 1959 *J. Fluid Mech.* **5**, 274.

PHILLIPS, O. M. 1967 *J. Fluid Mech.* **27**, 131.

PRANDTL, L. 1925 *Z. angew. Math. Mech.* **5**, 136.

PRANDTL, L. 1942 *Z. angew. Math. Mech.* **22**, 241.

REIS, F. B. 1952 Ph.D. dissertation, Mass. Inst. of Tech.

REYNOLDS, O. 1895 *Phil. Trans. Roy Soc. Lond.* A **186**, 123.

ROSE, W. G. 1966 *J. Fluid Mech.* **25**, 97.

ROTTA, J. C. 1951 *Z. Phys.* **129**, 547 (I) and **131**, 51 (II).

ROTTA, J. C. 1962 *Progress in Aeronautical Sciences*, vol. 2. (Ed. by A. Ferri, D. Küchemann and L. H. G. Sterne.) Oxford: Pergamon.

DE SAINT-VENANT, B. 1843 *C. r. Séanc. Acad. Sci.* **17**, 1270.

TAYLOR, G. I. 1915 *Phil. Trans. Roy. Soc. Lond.* A **215**, 1.

TAYLOR, G. I. 1932 *Proc. Roy. Soc.* A **135**, 685.

TAYLOR, G. I. 1936 *Proc. Roy. Soc.* A **157**, 537.

TAYLOR, G. I. 1938 *Proc. Roy. Soc.* A **164**, 15.

TOWNSEND, A. A. 1956 *The Structure of Turbulent Shear Flow.* Cambridge University Press.

TRITTON, D. J. 1967 *J. Fluid Mech.* **28**, 433.

UBEROI, M. S. 1957 *J. Appl. Phys.* **28**, 1165.

UBEROI, M. S. & CORRSIN, S. 1953 *N.A.C.A. Rep.* 1142.

WILLS, J. A. B. 1964 *J. Fluid Mech.* **20**, 417.

WYNGAARD, J. C. 1968 *J. scient. Instrum.* (*J. Phys.* E) ser. 2, **1**, 1105.